Università degli Studi di Padova

Department of Industrial Engineering

Master Thesis in Electrical Energy Engineering

Design and genetic algorithm optimization of a PM motor for the Formula SAE race car

Supervisor
Nicola Bianchi
Università degli Studi di Padova

Master Candidate
Giacomo Girelli

Academic year:
2020-2021

Contents

Abstract

The electric single-seat race car of the University of Padua, which participates in engineering competitions for students, is propelled by four electric motors mounted directly on the wheel.

This thesis deal with the design and the optimization of a new permanent magnet motor, maintaining the maximum compatibility with the old design. The torque objectives are defined by analysing the drive cycle of another similar car and a lap time simulation. The genetic algorithm optimization is performed using the analytical model of the internal permanent magnet motor. This model uses the lumped parameter magnetic circuit and the slot-opening concentrated conductors solving methods, with the additional correction of a fictitious saturation coefficient. These techniques are necessary to find a reasonable solution of fractional-slot motors with high flux densities. Moreover for comparison, a partial analytical model of the slotless motor is formulated.

Finally, the optimization is computed to find the optimal geometry with the best values of nominal torque, maximum torque, weight and losses. The obtained motor, which has 12 slots and 10 poles, is adjusted to reduce the torque ripple. Lastly, the finite element analysis is performed to verify the reliability of the analytical model results, the performance and the motor feasibility.

Riassunto esteso

Formula SAE, o Formula Student, è una competizione internazionale ingegneristica tra squadre di studenti universitari. L'obbiettivo è quello di concepire, progettare, realizzare e testare una monoposto in stile formula, che andrà a misurarsi in una serie di prove, valutate da una giuria di esperti del settore. Le prove si dividono in due tipologie: gli eventi statici ed gli eventi dinamici. I primi servono a giudicare il progetto della vettura da un punto di vista di *concept*, di gestione dei componenti e di *business plan*. Gli eventi dinamici invece mettono alla prova la vettura in pista per valutare l'accelerazione laterale, l'accelerazione longitudinale, l'efficienza e le prestazioni globali.

La squadra "Race UP" dell'Università degli Studi di Padova ha più di 60 studenti che, senza l'aiuto di professionisti, si occupano della progettazione di due vetture di Formula SAE: "MG" dotata di un motore a combustione interna, e "SG-e" elettrica. Quest'ultima, oggetto di studio della tesi, è dotata di quattro motori elettrici montati a ruota, controllati da inverter individuali e alimentati da una batteria a celle di litio. Questa configurazione a trazione integrale consente l'utilizzo della tecnica "torque vectoring", che, sfruttando una diversa distribuzione di coppia sulle ruote, permette di ottenere prestazioni migliori.

Questa tesi si occupa della progettazione e ottimizzazione di un nuovo motore a magneti permanenti. Infatti, attualmente la vettura elettrica utilizza quattro motori comprati, le cui caratteristiche di coppia, efficienza e peso possono essere migliorate. Oltre a ottenere delle prestazioni migliori in pista, una progettazione del motore potrebbe fornire un punteggio maggiore durante gli eventi statici. Inoltre, l'esperienza guadagnata dagli studenti durante la realizzazione, porterebbe a un progressivo miglioramento di anno per anno del progetto del motore elettrico. Per questo motivo, la transizione dal motore comprato a quello sviluppato in casa viene facilitata mantenendo la massima compatibilità con il vecchio sistema.

Gli obbiettivi di coppia e velocità del motore sono stati estrapolati dal ciclo di guida della vettura durante un evento dinamico. Siccome dei dati affidabili della vettura elettrica non sono disponibili, i cicli di guida della vettura a combustione "MG 13-18" durante l'evento "endurance" sono stati utilizzanti. In aggiunta, è stato fatto un confronto anche con i dati prodotti dalle simulazioni della vettura elettrica. Tramite queste analisi sono stati ottenuti gli obbiettivi di coppia nominale, coppia massima, velocità base e velocità massima del motore.

Nel quarto e quinto capitolo vengono formulati i modelli analitici del motore *slotless* e motore *slotted*. Entrambe le tipologie di motore rappresentano delle soluzioni interessanti per l'applicazione automotive. Il primo, infatti, permette di ottenere delle basse oscillazioni di coppia e un rendimento elevato per applicazioni

ad alta velocità. Il secondo invece è più comunemente utilizzato per la sua alta densità di coppia. Si è scelto di utilizzare dei modelli analitici per poter effettuare un'ottimizzazione multi-obbiettivo con molti parametri in ingresso mantenendo i tempi ridotti. Effettuare la stessa ottimizzazione utilizzando l'analisi agli elementi finiti richiederebbe tempi computazionali venti volte maggiori.

Il modello del motore *slotless* è stato costruito sulla base delle equazioni di coppia di A. Tessarolo. Il motore *slotless* presenta una geometria semplice, che permette di ricavare in modo analitico la soluzione dei campi magneti al suo interno. Il modello non è stato ulteriormente sviluppato poiché la geometria, per poter ottenere le necessarie prestazioni, presenta un momento d'inerzia troppo elevato per questa applicazione.

Il modello analitico del motore *slotted* è stato sviluppato a partire dal metodo di risoluzione a parametri concentrati del rotore. Siccome gli avvolgimenti considerati hanno un numero di cave basso, l'ordinaria ipotesi di conduttori distribuiti sinusoidalmente porterebbe a un sovrastima del risultato. Perciò, la tecnica dei conduttori concentrati nell'apertura di cava è stata utilizzata. La densità di flusso al traferro viene corretta con un coefficiente di saturazione fittizio, calcolato dai valori d'induzione dei denti e delle sezioni di corona. Infine, la coppia viene calcolata dai valori di densità di flusso e di carico elettrico. Inoltre, tre verifiche vengono effettuate: sostenibilità del regime termico, raggiungimento della velocità base e momento d'inerzia contenuto.

L'ottimizzazione multi-obbietivo viene effettuata tramite un algoritmo genetico per trovare i valori ideali di: diametro di statore, diametro esterno, lunghezza del pacco di lamiere, angolo di copertura dei magneti, spessore dei magneti, inclinazione dei magneti, larghezza dei denti, altezza della corona, densità di corrente nominale e corrente nominale. L'algoritmo viene utilizzato in prima battuta per fare un confronto tra le combinazioni di numeri di cave e poli, poi per valutare le prestazioni del motore *slotless* e infine per ottenere la geometria ottimale che soddisfa gli obbiettivi di coppia.

Nell'ultimo capitolo, vengono confrontati i risultati così ottenuti con un'analisi agli elementi finiti, per saggiare l'affidabilità del modello analitico del motore *slotted*. Successivamente, si controlla che le fluttuazioni di coppia siano minori dello standard di *FreedomCAR*, e si effettua una sagomatura dei poli per ridurle. La resistenza alla smagnetizzazione dei magneti viene verificata imponendo corrente massima sull'asse diretto. Vengono costruite la mappe di coppia, induttanze e velocità del motore. Infine, le prestazioni ottenute vengono confrontate con quelle del precedente motore, evidenziando i miglioramenti ottenuti.

Introduction

Established in 1981, the Formula SAE competition involves the conception, design and production of a single-seat car in formula style by university engineering students [3]. The project foresees the contribution of various engineering disciplines but also of other departments, in particular the economics one. As a matter of fact, the race car is not only evaluated for performance on track, but the overall design, the cost management and the business plan are further judged by a team of motorsport experts. Nowadays the competition, also called Formula Student, is widespread on every continents and sees the participation of the best universities.

The University of Padua participates annually to the competitions with its team "Race UP", which is simultaneously involved in the design of a car with an internal combustion engine and an electric car [5]. The latter uses an all-wheel drivetrain configuration, built with a bought package of four motors and four inverters.

The team trend over the years is to try to design and build every component without buying. In addition to earning more points in the design event, the ad hoc design allows to obtain better performance and more suitable for this application. This is the motivation that prompts to design a new electric motor. Moreover, the knowledge acquired by the team with the building of an electric motor, allows to adopt better and better solutions for each passing year. For this reason, the project of the new motor is performed maintaining the maximum compatibility with the old design, to facilitate the transition from bought to in-home built motor.

First, the torque and speed objectives are defined analysing the drive cycle of the car during a race. Since reliable telemetry data of the electric car are not available, the analysis is performed with the telemetry data of the Paduan combustion car and the results of a lap time simulation. The two drive cycle distributions are compared to define the torque and speed objectives.

The optimization of the motor geometry is performed with a genetic algorithm and an analytical model of the motor. In particular, two analytical models are considered: the slotless motor and the slotted motor. Both are an interesting solution for the automotive application. Indeed, the slotless motor presents low level of torque ripple and great efficiency in high speed conditions [9]. On the other hand, the slotted motor is commonly used for its high torque density.

The slotless model is formulated with the Tessarolo torque equations found thanks to the simple geometry [10][11]. The slotted model is developed by the solution of the lumped magnetic circuit of [12], improved extending the magnetic

circuit to the whole rotor. The hypothesis of slot-opening concentrated conductors is used to allow solving motors with low slots number and fractional-slots. The air gap flux density is then corrected by a fictitious saturation coefficient [14]. To verify the motor feasibility, three verifications are performed: thermal steady state, reaching base speed and moment of inertia lower than an established limit.

The analytical models are then used with the genetic algorithm to optimize the nominal torque, the maximum torque, the weight and the losses. The optimization is used to compare the different slots and poles combinations, to compare the slotless motor to the slotted one, and finally, to find the optimal geometry that satisfies the torque objectives.

In the last chapter, a comparison between the analytical model and the finite element analysis solutions is performed. The round shaping of the pole island is performed to reduce the torque ripple. Finally, the motor characteristics are compared to the bought motor.

Chapter 1

Formula SAE

Formula SAE (or Formula Student) is an international competition between teams of university students that design and build a single-seat formula race car [1][2][3]. Everything is left to the students, no professional is directly involved in the conception and designing of the car. The competition is an engineering project challenge: the winner is not necessarily the fastest car, but the one with an overall package of construction, performance, financial and sales planning. Indeed, the events in which a team must excel are not only aimed to evaluate the performance of the car, but also the knowledge, the planning, the creativity and the competence of the team. The aforementioned events are divided into two categories:

- **Statics Events**: No physical car is needed, just its design and the economic aspects.
  - Design Event: presentation of the complete project of the car.
  - Business Event: simulation of the presentation of the prototype in front of potential investors.
  - Cost Event: analysis of the costs in which are included quantities of materials and components used.
- **Dynamic Events**: The car performance is evaluated on the track.
  - Acceleration: The car accelerates from a standstill on a straight $75\,m$ track. So the longitudinal acceleration is evaluated.
  - Skid pad: The car runs on an eight pattern track and so the lateral acceleration is evaluated.
  - Autocross: The car runs in a $500\,m$ track with straights, curves, and chicanes to evaluate the overall race performance.
  - Endurance: The car runs for a total distance of $22\,km$. Race performance and fuel management are evaluated.

The judges are experts from the motorsport, automotive and supplier industries, and the official language of the competitions is English. The competitions are organized every year, but the important rule is that a team can not use the

Figure 1.1: Panoramic view of the teams at the ZF Race Camp 2019

same car as the previous year. This imposes that to participate every year in the same competition a new car must be designed, built and tested in one year span. This requires the teams to have good planning and a safety margin in case of design and production mistakes. The new single-seat car is classified as new if the chassis structure has undergone significant changes. The racecars are divided into three classes:

- Internal Combustion Engine Vehicle (CV): The cars are powered by an internal combustion engine (ICE) (no hybrid powertrains are allowed).
- Electric Vehicle (EV): The cars are powered by electric motors.
- Driverless Vehicle (DV): The drivetrain can be of either type, but the car presents a full autonomous driving (dynamic events are slightly different).

The race cars must be open-wheeled, single seat and open cockpit, like formula, but they present an overall smaller dimension due to many competition rules and for the need to race on tight and curvy tracks.

Figure 1.2: University of Padova CV "MG 13-18" during the FSG (Formula Student Germany) 2019 Autocross.

1.1 Race UP

In 2006 the team of the University of Padua "Race UP" participates in its first competition with a CV [4]. In 2010 the EV class is added in Formula SAE. In 2014 the Paduan team starts to design, in parallel with the CV, an EV that finally participates in its first competition in 2016 [4].

Nowadays the team is composed of more than 60 students, half of them work on the CV and the other half on the EV. Each team member is required to stay in the team for two years, allowing to have a training period in the first year and a generational change of half students in the second year. Thus, every 12 months the recruitment is held to replace the students who have completed their two years of participation. The students, besides being in the combustion or electric division, are further divided into departments. Every department takes care of a particular car aspect: Chassis, Mechanical Structures, Powertrain, Electronics, Vehicle Dynamics, Aerodynamics, Software, Business & Marketing. A manager is at the head of each department and refers to the Technical Director and the Team Leader of the division.

Figure 1.3: Race UP electric division and their car "SG-e 03" at FSG (Formula Student Germany) 2019

Chapter 2

SG-e 03

The last electric car designed and built by the Paduan team is called SG-e 03, while at today's date the SG-e 04 is still under construction. The car chassis is a monocoque made by sandwich panels of carbon fiber and aluminium honeycomb. This structure allows the chassis to have a great torsional stiffness of $2200\,Nm/deg$ with a very low weight of $9\,kg$. In addition to the monocoque, two bent steel tubes ensure the safety of the pilot in case of a rollover. The double wishbone suspensions have the push-rod configuration, that allows making better use of the available space. As a matter of fact, each wheel group must fit its dedicated drivetrain system, composed of one electric motor and one gearbox directly mounted on the wheel group. The electric motors are controlled by the inverters that are supplied by a lithium cells accumulator. The whole electronic system of the car is designed and built by the students, starting from the boards and the wiring, up to the software. Lastly, the aerodynamic package allows to generate $275\,N$ down force at $15\,m/s$, with low weight thanks to the carbon fiber based composite materials.
The overall weight of the car is $201\,kg$, with a wheelbase of $1.535\,m$ and a track of $1.23\,m$ [5].

Figure 2.1: The unveiling of SG-e 03 at the presentation of the Race UP single-seaters in 2019

2.1 Powertrain system

An all-wheel drive (AWD) is a powertrain configuration that provides power to all the wheels. Each SG-e 03 wheel is directly connected to an Internal Permanent Magnet (IPM) motor through an epicycloidal gearbox, and each electric motor is controlled by its inverter. All four inverters are connected to a single bus bar that is supplied by an accumulator of lithium cells. A simple electric schematic of the powertrain system is presented in figure 2.2.

This AWD configuration allows to have different speeds and torques for each motor, increasing the manoeuvrability of the car and permitting the possibility to use torque vectoring. Torque vectoring is a technique of variation of torque for each wheel to increase the performance of the car. For example, during a left turn, an increase of torque on the right wheels could increase the turning speed. Another simple example could be that during a straight acceleration the rear wheels have more load and so more torque can be applied to the rear wheels than the fronts.
The inverters and the motors are water cooled, while the accumulator is air cooled with fans. The inverters are cooled with a cold plate, the motors are cooled with an external cooling jacket.

Currently, the powertrain propulsion system is made using a bought package of four motors and four inverters by AMK Group. It's a package built by the company especially for the Formula Student. The main motor characteristics are reported in table 2.1.

The new design must improve the motor performances just presented, but it should also maintain the compatibility with the AMK inverters. But not only with

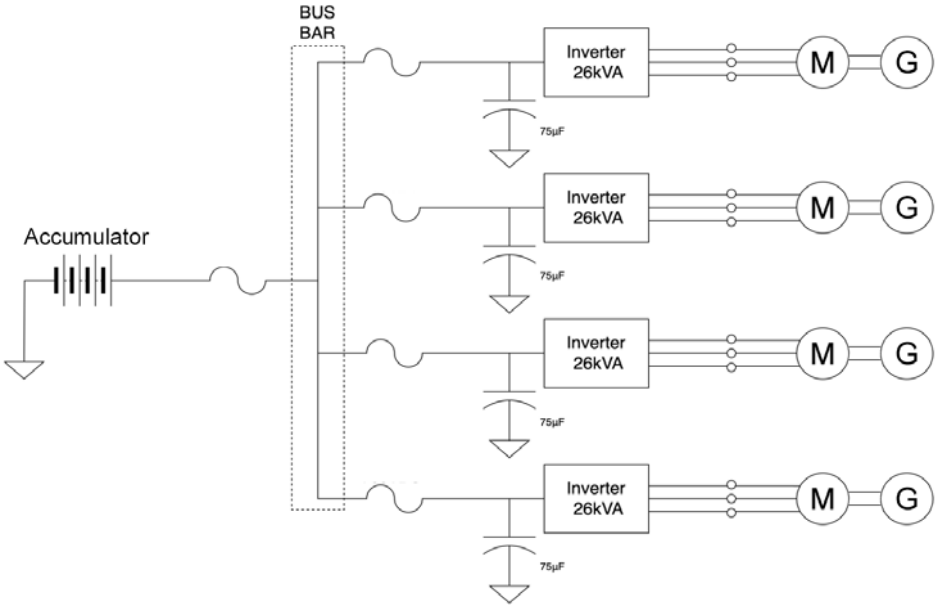

Figure 2.2: Powertrain electric system schematic

AMK motor characteristics	
Nominal torque	$9.8\,Nm$
Nominal speed	$12000\,rpm$
Nominal power	$12.3\,kW$
Nominal efficiency	$87.34\,\%$
Maximum torque	$21\,Nm$
Maximum speed	$20000\,rpm$
Poles number "$2p$"	10
Insulation class	F
Weight	$3.55\,kg$

Table 2.1: AMK motor main characteristics

the inverters: the maximum compatibility with the whole car must be maintained. The reason is that every year a new car must be designed and built, and the failure of the design or the manufacturing of one component requires to find a fast solution in a limited span of time before competitions. The best way is to maintain the compatibility between new and old systems, so in case of failure of a new component, it can be used the old one to replace it. Another reason is that the transition from a bought motor to an in-home-built motor is smoother if the rest of the components, which have been tested and are reliable, remain the same.

The main parts, that give us compatibility constraints, are the transmission system, the supply system and the cooling system. These systems impose numerous constraints that could reduce the possibilities of improvement of the new motor design, but it's preferable to start with a safe solution to increase the team knowledge of building an electric motor. Once the knowledge is solid, the team can attempt to use more bold solutions, reducing the system compatibility.

2.1.1 Transmission

The transmission system is mainly composed by an epicycloidal gearbox directly mounted in the upright. The motor is attached with an adapter to the upright (figure 2.3).

The gearbox transmission ratio is $\tau = 14.4$, and so it binds the range speed of the motor to the range speed of the car. For example, considering the maximum speed that the car could reach during a race, the corresponding maximum motor speed is expressed as

$$n_{max}\,[rpm] = \frac{60 \cdot \tau \cdot v_{max}\,[km/h]}{3.6 \cdot 2\pi R_{wheel}\,[m]} \tag{2.1}$$

where R_{wheel} is the radius of the tire, v_{max} is the maximum car speed in km/h. Considering the SG-e 03 case study, the Hoosier tires have a radius of $R_{wheel} = 0.228\,m$ and the maximum speed reached by the car is $v_{max} \simeq 120\,km/h$, then the maximum motor speed to be achieved is $n_{max} \simeq 20000\,rpm$.

Another constraint given by the transmission system is the coupling of the new motor design with the gearbox. While the coupling of shafts is purely a mechanical constraint and does not limit the electromagnetic design, the maximum encumbrance of the motor is restricted by the mounting points (figure 2.4). It's impossible or very complicated to mount a motor with a larger diameter than the mounting points. The space of the mounting points is further decreased by the cooling jacket around the motor. This leads to the diameter of the current mounted motors that is $96\,mm$.

Another encumbrance constraint is the axial length. There is not a precise maximum axial length, but a decrease in axial length would improve the outboard cable and cooling tube management of the steering front wheels. Indeed, reducing

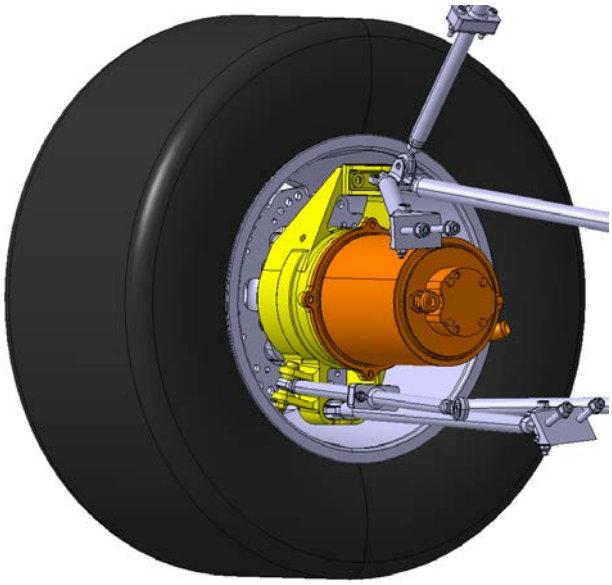

Figure 2.3: SG-e 03 wheel group: gearbox integrated in the upright (yellow) and motor (orange)

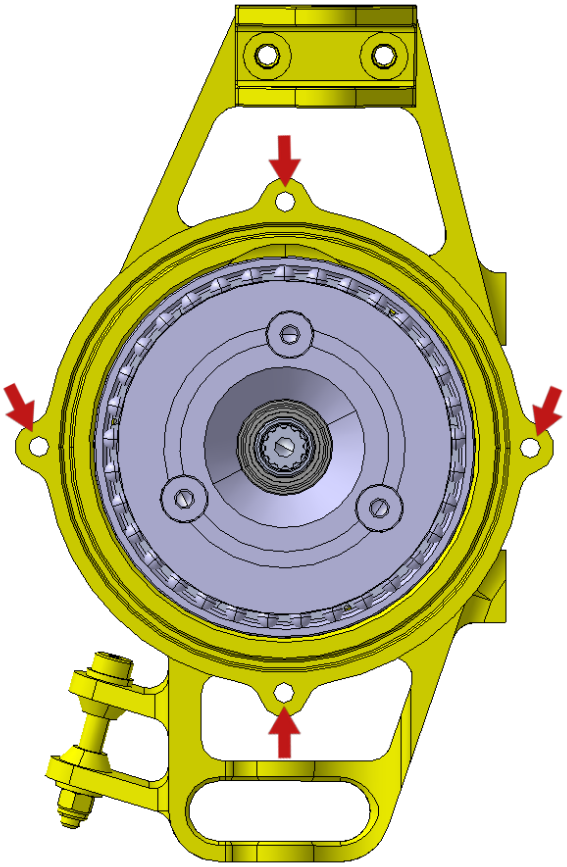

Figure 2.4: Upright mounting points (red arrows)

the radius of rotation with respect to the center of rotation of the steering wheel would decrease the maximum excursion of cables and tubes.

2.1.2 Supply

The supply system is mainly composed of the two other electric components in series with the motor: the inverter and the accumulator. The constraints given by these components are the voltage and the current available for the motor. The maximum supply voltage depends on the DC bus voltage, that is directly connected to the accumulator. The maximum continuous current and the peak current depend instead on the lowest limit between battery or inverter.

The accumulator has a 142s2p configuration using the $LiCoO_2$ pouch cell by Melasta (cell specifications reported in table 2.2). The accumulator voltage depends on the DOD (Depth of Discharge) of the $LiCoO_2$ cells, which is presented in figure 2.5. A constant discharge of 15C is never reached because the battery current would be $190.5\,A$ that exceeds the maximum usable power imposed by the rule book, that is $80\,kW$. Considering the mean power of the motors during a race $21\,kW$ (see calculation in section 3.2.1), the mean current is equal to $\frac{21\,kW}{530\,V} = 40\,A$ that is equal to $3.1C$. With this rate of discharge the voltage/DOD curve can be considered close to the one measured with low C (figure 2.5). Thus, it can be

Cell specifications	
Cell model	Melasta SLPBA843126 pouch cell
Cell nominal capacity	$6.35\,Ah$
Maximum voltage	$4.2\,V$
Nominal voltage	$3.7\,V$
Minimum voltage	$3\,V$
Maximum continuous output current	$95.25\,A$

Table 2.2: Melasta SLPBA843126 pouch cell specification

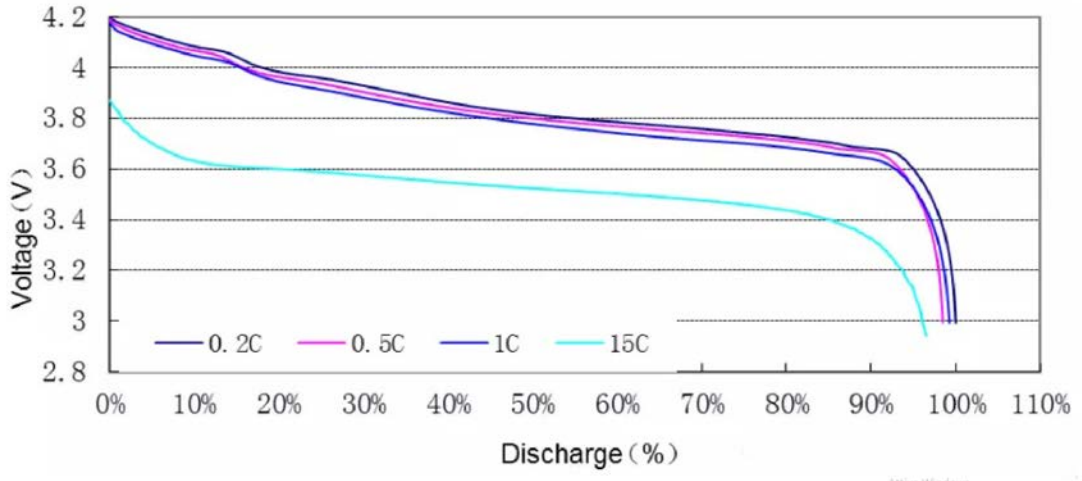

Figure 2.5: Discharge curve of a $LiCoO_2$ cell (Melasta SLPBB042126)

used the nominal voltage reported on the cell data sheet to calculate the nominal voltage of the battery:

$$E_{DC} = 142 \cdot 3.7\,V = 525.4\,V \tag{2.2}$$

The nominal DC bus voltage used to dimension is further reduced by $30V$ to account the reserve used for the inverter control and any possible voltage drop. The peak nominal voltage delivered by the inverter is then calculated as

$$\hat{E} = \frac{E_{DC} - 30\,V}{\sqrt{3}} \simeq 286\,V \tag{2.3}$$

The continuous and peak currents are not constrained by the accumulator, that has a current rating much higher than the inverter. The maximum continuous current of the inverter is $I_n = 43\,A$, and the peak current is $I_{peak} = 105\,A$, which can be maintained for $10\,s$. The peak current will be used to calculate the the maximum torque. There is no reason to size the motor with a lower current because it would mean dimensioning with a lower power, so limiting either the torque or the speed. On the other hand, the nominal current must be chosen on the basis of the ratio between the maximum torque and the nominal torque. For example, if the nominal torque is 25% of the maximum torque, the nominal

current should be 25% or lower than the peak current, otherwise it is impossible to achieve these performances.

2.1.3 Cooling

The cooling system is used to maintain the motors and the inverters within the temperature range specified by the data sheet. It uses plain water to cool the motors with a water jacket, and the inverters with a cold plate in contact with the IGBTs. The two radiators positioned in the side pods exchange heat with the flowing air.

To maintain the same components of the cooling system, the cooling fluid must be plain water. Thus, to ensure a safety condition and an easier manufacturing, the motor cooling is maintained external. In fact, internal cooling with plain water would require special precautions.

For the motor sizing, it's considered the steady water temperature of the actual operating condition of the cooling system, that in the worst case scenario is $80°C$. This high temperature is caused by the air conditions during the race: the air in August over a concrete track can reach temperatures up to $40°C$. Furthermore, the air flow in the radiators is limited by the low average speed ($50\,km/h$) of the race car. This cooling temperature highlights also the problem with the previous class F motors ($155°C$), of which the data sheet required a water temperature lower than $40°C$. Thus, the insulation rating is increased to the most suitable Class H ($180°C$) . Dimensioning with a higher insulation class yields a good safety factor on thermal management, and it could lead to a reduction of the cooling capabilities, which results finally in a lower weight of the cooling system.

Chapter 3

Operating conditions

To size properly the motor, the objectives of speed and torque must be defined accurately. But the electric motors for automotive applications do not work at a constant speed and torque. They have to propel the car from standstill to maximum speed with different accelerations, so a wide region of performance is required. However, it is possible to visualize in a chart the points of speed and torque to identify the region where the motor is required to work most often. This speed and torque distribution can be acquired by telemetry data or with a lap time simulation of the race car on the track. In this chapter, both distributions are presented, to highlight the difference between real and ideal data. Then the objective of speed and torque are defined.

Precise telemetry data of the electric division car are not available, thus the telemetry data of the combustion division car are used. The distribution of speed and torque of a CV is expected to be similar to the one of an EV. As a matter of fact, the scoring results at competitions are similar for both classes but slightly better for the electric one. Thus, the results obtained with the CV telemetry should be increased.

3.1 Data elaboration

The initial data available are the velocity u of the car in km/h sampled with a frequency of $f = 20\,Hz$. So, the time interval between each sampling is

$$\Delta t = \frac{1}{f} = 50\,ms \tag{3.1}$$

Then, the acceleration in m/s^2 in every time interval can be calculated as

$$a(k) = \frac{u(k+1) - u(k)}{3.6 \cdot \Delta t} \tag{3.2}$$

This is the resulting acceleration of the car, but the force that acts on the vehicle is not only the motors one. Also the aerodynamic resistance $F_{aero}\,[N]$ and the

tires rolling resistance $F_{roll}\,[N]$ are applied to the car. So, the balance of forces is

$$\frac{\tau C}{R} = aM + F_{aero} + F_{roll} \tag{3.3}$$

where C is the sum of the motors torques, $\tau = 14.4$ is the gearbox ratio, $R = 0.228\,m$ is the wheel radius and $M \simeq 270\,kg$ is the car weight including the pilot. In the equation it does not appear the contribution of brakes for negative accelerations. Indeed, it is assumed that all the kinetic energy is recovered with regenerative braking of the motors. This increases the efficiency of the car and allows to evaluate if the total braking can be performed by the motors.

The aerodynamic resistance is calculated using the drag equation:

$$F_{aero} = 0.5 \cdot c_{xA} \cdot \rho \left(\frac{u}{3.6}\right)^2 \tag{3.4}$$

where $c_{xA} = 1.2\,m^2$ is the car coefficient of drag multiplied by the area and $\rho = 1.225\,kg/m^3$ is the air density.

The tire rolling resistance is calculated as

$$F_{roll} = M \cdot g \left[f_0 + f_2 \left(\frac{u}{3.6}\right)^2\right] \tag{3.5}$$

where $g = 9.81\,m/s^2$ is the gravitational acceleration, $f_0 = 0.02$ is the tire rolling resistance coefficient from standstill ($u = 0$) and $f_2 = 6.48 \cdot 10^{-6}$ is the tire rolling resistance coefficient that depends on the square of the velocity.

Once the total torque C is calculated with (3.3), the torque must be divided between motors. The torque distribution is a complex task because depends on many variables, and it is the result of the torque vectoring. So in every time instant, the torque is not uniformly distributed between motors. But because the nominal torque is required, the average value of torque distribution can be considered. As a matter of fact, the nominal torque will be approximately in the center of the region where the motor is required to work most often. The average torque on the whole run of left and right motors can be considered equal. The average torque distribution between front and rear motors is considered with a ratio 45%/55%, which is the result of in-depth studies by the department of vehicle performance. For manufacturing simplicity, the same motors are used for front and rear wheels, thus the sizing must be performed with the most demanding load that, according to the distribution ratio, is the rear motor. Finally, the torque of a single rear motor is calculated as

$$c = C \cdot \frac{0.55}{2} \tag{3.6}$$

The motors instantaneous speeds are not the same for left and right motors because of the curves. Thanks to the same consideration made before, the average

value can be considered and it can be calculated as

$$n = \frac{u \cdot \tau 30}{3.6\pi R} \tag{3.7}$$

3.2 Speed and torque distribution

It is important to select the right data to evaluate the heavier operating conditions of the motor. Of the four types of dynamic events presented in chapter 1, the most meaningful are the endurance and the acceleration. The endurance is the event that requires the motor to work for a long time, thus the thermal steady state is reached. So, the nominal torque of the motor must be capable to satisfy the endurance required torque. Moreover, the range speed of the endurance must be satisfied to obtain the best time results. The acceleration is the event that requires the maximum torque and the car can reach its maximum speed. So while the maximum speed has been already considered in section 2.1.1, the maximum torque of the motor must be maximized. Thus, even if not necessary, the acceleration event speed/torque distribution is presented just for comparison with the endurance one.

3.2.1 Telemetry data

The telemetry data used are those of the Paduan CV "MG 13-18" during the FSG (Formula Student Germany) competition in 2019. FSG competition has been selected because it's the most important and sees the best European teams participate every year. Furthermore, the track of FSG autocross and endurance is the same every year.

In figure 3.1 the speed and the acceleration of a single lap of the endurance event are presented. In the acceleration chart is also reported the maximum value ($13.5\,m/s^2$) found in the lap time simulation of the electric car during the acceleration event. The limit is always respected except for a peak at $\sim 124\,s$ that is almost certainly an error due to a previous important braking. As a matter of fact, also the braking at $\sim 102\,s$ and $\sim 108\,s$ are followed by sudden acceleration. This disturbance occurs at the same moment on the other laps. During this endurance the mean power of the 4 motors is $21\,kW$.

The torque distribution presents large variations but in very short times, thus the motor temperature does not vary too much from the steady state. Neglecting the saturation, the torque depends linearly on the current. The thermal limits, that are reached during the endurance, depend mainly on the joule losses, which are therefore $\propto c^2$. Thus, to evaluate the thermal limits of the endurance the RMS torque is considered [6]:

$$c_{RMS} = \sqrt{\sum c^2} \tag{3.8}$$

The iron losses instead depend also proportionally to the frequency: for $\sim 70\%$ linearly (hysteresis losses), for $\sim 30\%$ to the square of the frequency (eddy cur-

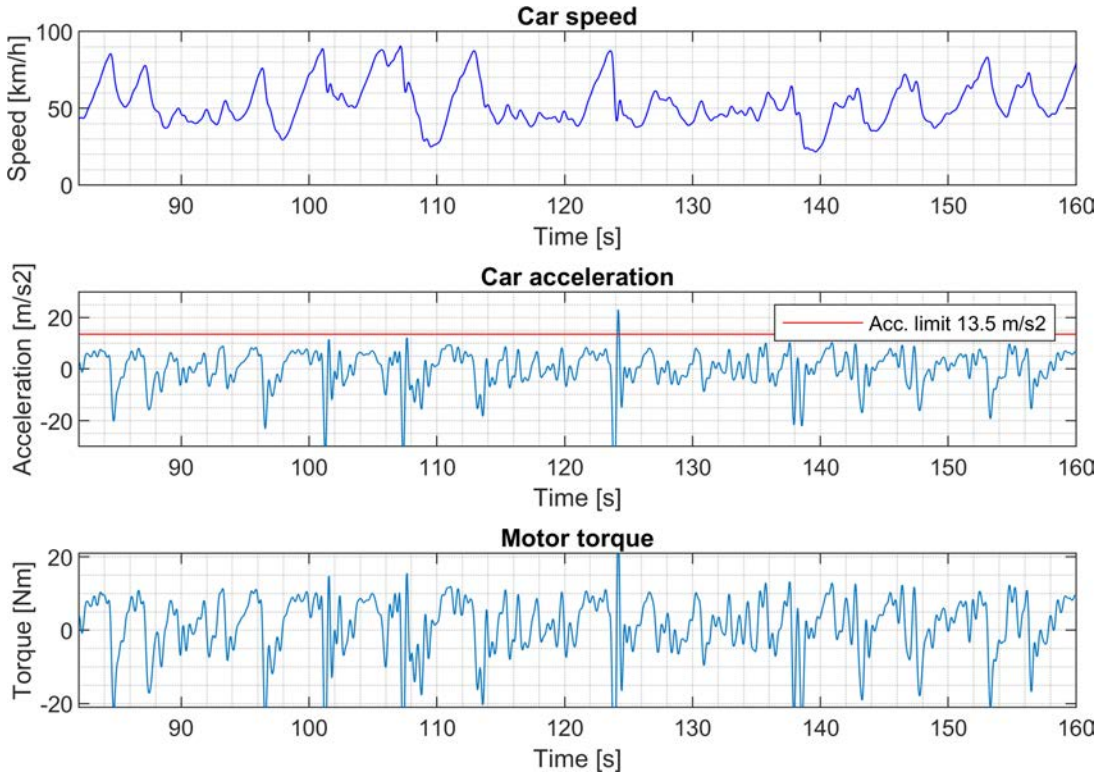

Figure 3.1: Car speed, car acceleration and torque of a single motor in one lap of 2019 FSG endurance of MG 13-18

rents). For simplicity the nominal speed has been calculated as an average of all speeds, thus considering the proportionality of the hysteresis losses.

The endurance data can be reported on a speed/torque chart (figure 3.2). The negative torque (braking) has been separated from the positive torque (accelerations) to highlight the different regions of work. The negative torque has been limited to $-21Nm$, with the hypothesis that the remaining torque needed is provided by the brakes.
The RMS torque of the acceleration phase is $6.8\,Nm$ and occurs at $9\,krpm$ nominal speed (red star in figure 3.2).
The RMS torque of the braking phase is $7.6\,Nm$ and occurs at $8.25\,krpm$ nominal speed (red star in figure 3.2).

3.2.2 Lap time simulation

The data of the lap time simulation has been produced with the script "Optimum Lap Race UP", coded by the vehicle dynamics department, using the model of [7]. The track used is the FSG autocross, which is the same endurance track of section 3.2.1. In the speed/torque distribution chart (figure 3.3) is also presented the results of the lap time simulation of the acceleration event to highlight the operating limit of the motor. It is necessary to remember, however, that the distribution has been generated with the ratio 45%/55%. Thus, the instantaneous torque overcomes this limit, especially on the acceleration event in which the

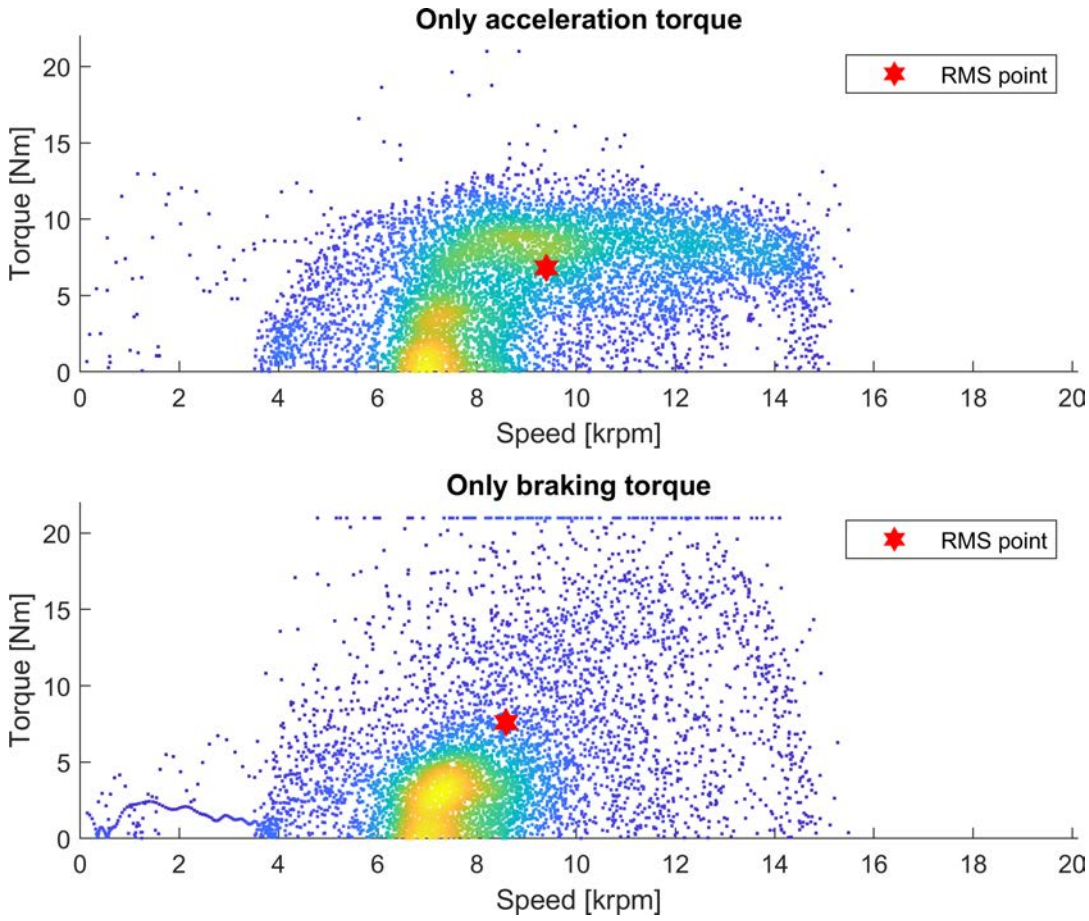

Figure 3.2: Speed and torque distribution of a single motor using the telemetry data of the 2019 FSG endurance of MG 13-18

distribution of torque is more shifted towards the rear motors.

It is evident that the ideality of the simulation gives a higher torque range of performance compared to the data telemetry one. As a matter of fact, the mean power of the 4 motors is $40\,kW$, that is nearly double that of the telemetry data. While the braking torques are completely out of range and can be obtained only using the brakes, the acceleration torques can be considered as an objective to approach. The RMS torque of the acceleration phase is $9.8\,Nm$ at $10\,krpm$ (red star in figure 3.3).

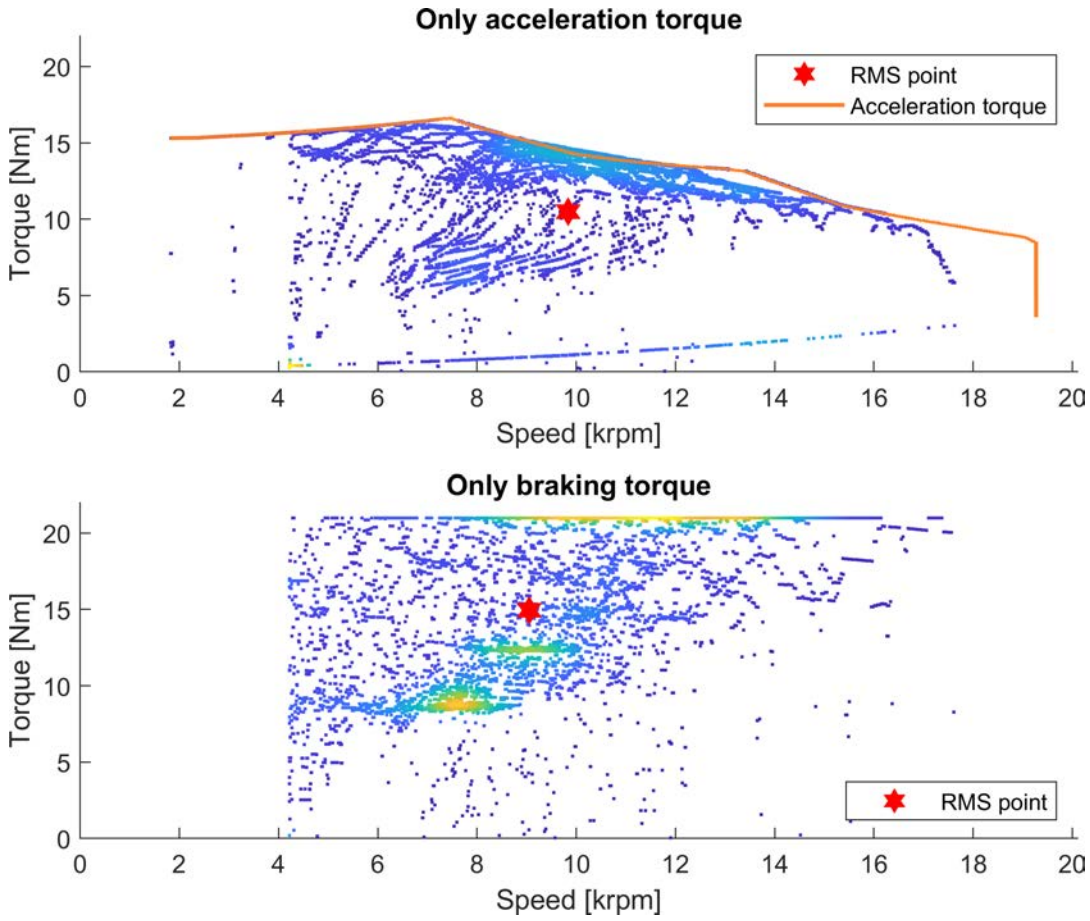

Figure 3.3: Speed and torque distribution of a single motor in the lap time simulation of SGe-03 in the FSG autocross event and in the acceleration event.

3.3 Moment of inertia

Further lap time simulations have been performed to evaluate the impact of the motor inertia on the acceleration event. The results in figure 3.4 highlight that only moment of inertia greater than $7 \cdot 10^{-4}\, kgm^2$ worsen the time result. Inertias lower than this value are irrelevant to the car performance.

The total moment of inertia of the wheel group is given by

$$M_{J,tot} = M_{J,w} + M_{J,g} + M_{J,m} \cdot \tau^2 \tag{3.9}$$

where $M_{J,w} = 0.28\, kgm^2$ is the inertia of the assembly of the tire and the wheel rim, $M_{J,g} = 0.000427\, kgm^2$ is the gearbox inertia, $M_{J,m}$ is the motor inertia and $\tau = 14.4$ is the gearbox ratio. The limit found with the lap time simulation is $\sim 50\%$ of the inertia of the rest of the wheel group.

The moment of inertia of the motor, approximating the rotor to a full cylinder, can be calculated as

$$M_{J,m} = \frac{1}{8} m_r D_r^2 \tag{3.10}$$

where m_r is the rotor mass and D_r is the rotor diameter. The rotor mass can be

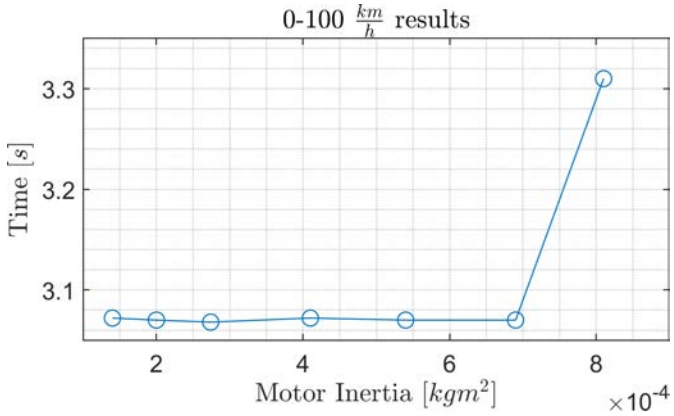

Figure 3.4: Lap time simulation of acceleration event in function of the motor moment of inertia.

approximately calculated as the moment of inertia of a full iron cylinder:

$$m_r = \gamma_{fe} \frac{\pi}{4} D_r^2 L_{stk} \tag{3.11}$$

where γ_{fe} is the iron density and L_{stk} is the rotor length. Then, substituting the (3.11) in the (3.10), the rotor diameter can be obtained as a function of the other parameters. Using the moment of inertia limit found with the lap time simulation and a rotor length of $L_{stk} = 60\,mm$, it results

$$D_r = \sqrt[4]{\frac{32 M_{J,m}}{\pi \gamma_{fe} L_{stk}}} = 62.5\,mm \tag{3.12}$$

Since the expected rotor diameter of the new design is close to $60\,mm$, the motor moment of inertia must be checked to make sure that does not overcome this limit.

3.4 Objectives

The objectives that must be reached by the motor have been chosen by both the results of telemetry data and lap time simulation. The telemetry data, although they represent a real Formula SAE car on the track, they are the result of a different drivetrain. On the other hand, the lap time simulation, although uses the SG-e 03 characteristics, has the operating conditions that are an ideal limit of the race car. Thus, neither of the two can be considered as the real and correct operating conditions.

The competition results testify that the EVs are faster than CVs in every dynamic event. Thus, a real higher RMS endurance torque value is expected for SG-e 03 compared to that of the MG 13-18. To evaluate how much the torque could increase for SG-e 03, the performance comparison between the best EV in FSG and the MG 13-18 is considered. The time results of 2019 FSG endurance of the best EV (München TU) and MG 13-18 are: $t_{EV} = 1321.15\,s$

and $t_{CV} = 1402.98\,s$ [8]. The faster time result is assumed to be obtained only with a greater acceleration by the EV. A constant acceleration a is considered. The uniform acceleration equation is

$$x = \frac{1}{2}at^2 \tag{3.13}$$

where x is the hypothetical length of the track. Equaling the equation for the EV and the CV, the ratio of acceleration is

$$\frac{a_{CV}}{a_{EV}} = \left(\frac{t_{EV}}{t_{CV}}\right)^2 = 0.887 \tag{3.14}$$

Because the motor torque is almost proportional to the acceleration, this ratio represents the increase of torques during the acceleration phase. So the RMS torque found in the CV telemetry data becomes $\frac{6.8\,Nm}{0.887} = 7.7\,Nm$. This is the minimum nominal torque to be achieved by the motor. The objectives of nominal torque and nominal speed are chosen by the lap time simulation results because they represent the operating ideal limit, that guarantees that the real car will operate within these ranges even with the best conditions. The base speed instead is chosen considering the telemetry data distributions in figure 3.2, that clearly does not exceed $15\,krpm$.

Instead, the maximum torque is found with a different calculation performed by the vehicle dynamics department, considering the torque needed to generate the maximum yaw moment with the torque vectoring. The result found is $29\,Nm$, but a more reasonable value is $21.9\,Nm$.

Finally, the objectives are summarized in table 3.1.

Objectives	
Nominal torque T_n	$7.7 \div 9.8\,Nm$
Nominal speed n_n	$10\,krpm$
Base speed n_B	$15\,krpm$
Maximum torque T_{max}	$21.9 \div 29\,Nm$
Maximum speed n_{max}	$20\,krpm$
Moment of inertia $M_{J,m}$	$< 7 \cdot 10^{-4}\,kgm^2$

Table 3.1: New motor design objectives.

Chapter 4

Slotless model

A conventional electric motor is designed with a stator that has an outer iron ring and several iron teeth facing inward (figure 4.1 (a)). This structure is designed to carry the magnetic flux with the minimum magnetic voltage drop. Furthermore, the teeth separates the winding coils and provide a mechanical anchoring. Another possible structure is the slotless motor, which does not have the teeth but instead, the winding occupies all the circumference space (figure 4.1 (b)).

Slotless PM motors are gaining interest to be used for EV or HEV (Hybrid electric vehicles), thanks to their low level of torque ripple [9]. Furthermore, they can offer the benefit of reduction of losses for high speed application thanks to the low magnetic flux density [9]. Indeed, this characteristic reduces a lot the iron losses, while the joule losses are almost constant with speed. On the other hand, to achieve the same performance as laminated machines, the magnet weight tends to be $3 \sim 3.5$ times larger [9]. However, this is not a very relevant downside because the performance has priority while the manufacturing cost is less important, considering also that the motors to be built are few.

The model of the slotless motor is needed to first evaluate if it holds up the comparison with the slotted motor and then, in that case, to obtain the geometry optimization using the genetic algorithm. Thus, it must be as reliable as possible. Thanks to its simple geometry the analytical solution of the magnetic field can

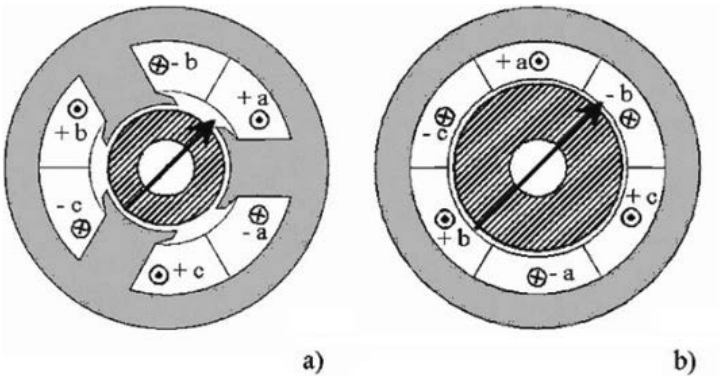

Figure 4.1: Slotted (a) and slotless (b) PM motor structure. [13]

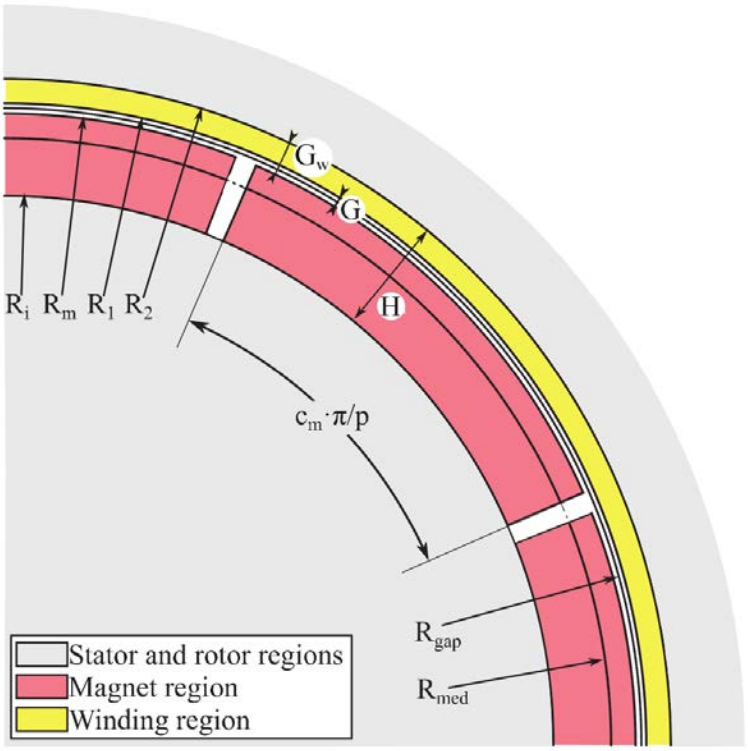

Figure 4.2: Slotless SPM motor geometry with main dimensional data. [10]

be easily found: the torque equations by A. Tessarolo [10] [11] are used. The Tessarolo model is a slotless motor with surface mounted magnets and the winding occupy the whole circumference, there is not space between slots. Although it does not represent the actual final geometry of the motor, that could have shaped magnets and space between slots. These simplifications will still guarantee the determination of the main geometric parameters and the motor performance. Then eventually, in case of choice of the slotless solution instead of the slotted one, it will require an optimization using the Finite Element Analysis (FEA) to refine the details of the magnet shaping and the winding distribution.
The motor geometry and its dimensional data are defined in the figure 4.2.
The airgap G and the magnet thickness t_m can be calculated as

$$\begin{aligned} G &= R_1 - R_m \\ t_m &= R_m - R_i \end{aligned} \tag{4.1}$$

The radial magnetization M of the magnets is defined as

$$M = \mu_r H_{cB} \frac{t_m + G}{t_m + \mu_r G} \tag{4.2}$$

where μ_r is the relative permeability of the magnet, and H_{cB} is the magnet coercitivity calculated by the remanent flux density B_{rem}:

$$H_{cB} = \frac{B_{rem}}{\mu_r \mu_0} \tag{4.3}$$

4.1 Torque equation

The average torque formula, neglecting the torque ripple, by A. Tessarollo [10] is expressed as

$$T_{mean} = 4p^2 M L_{stk} F(p, R_2, R_1, R_m, R_i, J_n) \sin\left(\frac{\pi c_m}{2}\right) \tag{4.4}$$

where p is the number of pole pairs, L_{stk} is the stack length of the machine, c_m is the magnet to pole span ratio and $F(p, R_2, R_1, R_m, R_i, J_n)$ is a function defined as

$$F(p, R_2, R_1, R_m, R_i, J_n) = \begin{cases} \frac{1}{2} A_m^+ (R_m^2 - R_i^2) + A_m^- \cdot ln(R_m/R_i) & p = 1 \\ \frac{A_m^+ (R_m^{p+1} - R_i^{p+1})}{p+1} + \frac{A_m^- (R_m^{-p+1} - R_i^{-p+1})}{-p+1} & p \neq 1 \end{cases} \tag{4.5}$$

$A_m^+(p, R_1, R_i, J_n, A_w^+, A_w^-)$ and $A_m^-(p, R_1, R_i, J_n, A_w^+, A_w^-)$ are constants of the magnetic vector potential in the permanent magnet domain, and are defined as

$$\begin{cases} A_m^+(p, R_1, R_i, J_n, A_w^+, A_w^-) = \frac{((A_w^- + A_w^+ R_1^{2p})(p^2-4) + \mu_0 J_n R_1^{p+2})}{((R_1^{2p} + R_i^{2p})(p^2-4))} \\ A_m^-(p, R_1, R_i, J_n, A_w^+, A_w^-) = \frac{((A_w^- + A_w^+ R_1^{2p})(p^2-4) + \mu_0 J_n R_1^{p+2})}{((R_1^{2p} + R_i^{2p})(p^2-4))} \cdot R_i^{2p} \end{cases} \tag{4.6}$$

$A_w^+(p, R_2, R1, R_m, R_i, J_n)$ and $A_w^-(p, R_2, R1, R_m, R_i, J_n)$ are constants of the magnetic vector potential in the winding domain, and are defined as

$$\begin{cases} A_w^+(p, R_2, R_1, R_m, R_i, J_n) = \\ \frac{\mu_0 J_n}{2p(R_2^{2p} - R_i^{2p})} \left(\frac{4R_2^{p+2} - R_i^{2p} R_1^{2-p}(2+p) + R_1^{p+2}(p-2)}{(2+p)(2-p)} \right) \\ A_w^-(p, R_2, R_1, R_m, R_i, J_n) = \\ \frac{\mu_0 J_n}{2p(R_i^{-2p} - R_2^{-2p})} \left(\frac{4R_2^{-p+2} + R_i^{-2p} R_1^{2+p}(-2+p) - R_1^{-p+2}(p+2)}{(2+p)(2-p)} \right) \end{cases} \tag{4.7}$$

where J_n is the current density fundamental amplitude and it is calculated by the current density in the slot J_{slot} as

$$J_n = \frac{3\sqrt{2}}{\pi} \cdot J_{slot} \tag{4.8}$$

The current is not uniformly distributed over the slot, but it is concentrated in the conductors. Thus, considering the filling factor k_{fill} and the conductors current density J_{Cu}, the slot current density is expressed as $J_{slot} = J_{Cu} \cdot k_{fill}$. Finally, the

current density fundamental amplitude (4.8) can be expressed as

$$J_n = \frac{3\sqrt{2}}{\pi} \cdot J_{Cu} \cdot k_{fill} \tag{4.9}$$

4.2 Weight

Using the dimensional data defined in figure 4.2, the volumes (V) and the weights (G) of the motor parts can be expressed as:

- Back iron:

$$\begin{aligned} V_{fe,s} &= \frac{\pi}{4}(D_e^2 - 4R_2^2)L_{stk}k_{stack} \\ G_{fe,s} &= V_{fe,s}\gamma_{fe} \end{aligned} \tag{4.10}$$

- Permanent magnet:

$$\begin{aligned} V_{pm} &= \pi(R_m^2 - R_i^2)L_{stk}c_m \\ G_{pm} &= V_{pm}\gamma_{pm} \end{aligned} \tag{4.11}$$

- Rotor iron:

$$\begin{aligned} V_{fe,r} &= \pi R_i^2 L_{stk}k_{stack} \\ G_{fe,r} &= V_{fe,r}\gamma_{fe} \end{aligned} \tag{4.12}$$

- Winding:

$$\begin{aligned} V_{Cu} &= \pi(R_2^2 - R_1^2)L_{cond}k_{fill} \\ G_{Cu} &= V_{Cu}\gamma_{Cu} \end{aligned} \tag{4.13}$$

- Winding resin:

$$\begin{aligned} V_{res} &= \pi(R_2^2 - R_1^2)L_{stk}(1 - k_{fill}) \\ G_{res} &= V_{res}\gamma_{res} \end{aligned} \tag{4.14}$$

where $\gamma_{fe}, \gamma_{pm}, \gamma_{Cu}, \gamma_{res}$ are respectively the densities of iron, magnets, copper and winding resin; k_{stack} is the stacking factor of the lamination. The conductors length L_{cond} has been calculated as the sum of the motor axial length and the end-winding length:

$$L_{cond} = L_{stk} + \frac{5R_1}{p} \tag{4.15}$$

Finally, the total weight of the slotless motor is the sum of the weights of the parts:

$$G_{tot} = G_{fe,s} + G_{pm} + G_{fe,r} + G_{Cu} + G_{res} \tag{4.16}$$

4.3 Losses

Concerning the motor losses only the joule losses are considered because the iron losses, thanks to the low magnetic flux density, are small compared to the winding one. The joule losses are calculated as

$$P_J = \rho_{Cu,165^\circ C} J_{Cu}^2 V_{Cu} \tag{4.17}$$

4.4 Moment of inertia

As explained in section 3.3, the moment of inertia of the motor can reduce considerably the car performance. Thus, the value must be lower than the limit found. The moment of inertia of the slotless motor, using the equation (3.10), is calculated as

$$M_J = \frac{1}{8}(G_{fe,r} + G_{pm})(2R_m)^2 \tag{4.18}$$

Chapter 5

Slotted model

In this chapter, an in-depth analytical model of the Internal Permanent Magnet (IPM) slotted motor is formulated. The purpose of the model is to obtain the torque, the weight and the losses starting from a given geometry. The model will be used to find the optimal geometry using the genetic algorithm. The same optimization performed with the Finite Element Analysis (FEA) would have brought to very long computational times. The analytical model is found using the lumped parameter magnetic circuit described by [12], improved with a more general magnetic circuit, which includes the whole rotor, and with the slot-opening concentrated conductors hypothesis [13]. Finally, the solution is further corrected using a fictitious saturation of the stator iron [14].

5.1 Slot opening concentrated winding

The usual hypothesis of sinusoidally distributed conductors is not feasible for a low number of slots, in particular with fractional slots. So, to solve the analytical computation of the magnetic field produced by the winding, the conductors are concentrated in the slots openings [13] and the electric load is computed. Then the magnetic potential is computed and finally, using the lumped parameters model, the magnetic field result is calculated.

Once the combination of slots/poles is selected, a modified square wave function $slots(\theta_m)$ is generated. It indicates the position of the slot openings and their width along the stator circumference as a function of the mechanical angle θ_m (from 0 to 2π). To assign the proper slot to the right phase, more square wave functions are used: $K_a(\theta_m)$,$K_b(\theta_m)$,$K_c(\theta_m)$ reproduce the slot matrix along θ_m for the three phases.

The distribution of the three-phases conductors (figure 5.1) can be expressed as

$$\begin{aligned} n_{da}(\theta_m) &= \hat{n}_d K_a(\theta_m) slots(\theta_m) \\ n_{db}(\theta_m) &= \hat{n}_d K_b(\theta_m) slots(\theta_m) \\ n_{dc}(\theta_m) &= \hat{n}_d K_c(\theta_m) slots(\theta_m) \end{aligned} \tag{5.1}$$

where $\hat{n}_d$ is the amplitude of the conductors function [12]. The value of $\hat{n}_d$ can

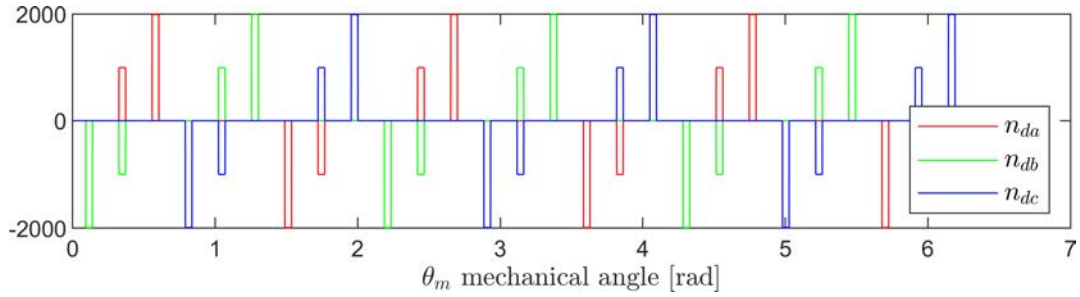

Figure 5.1: Conductors functions of a Q=27 2p=6 motor, with $N = 50$, $D_s = 120\,mm$ and $\alpha_o = 2.67°$

be expressed as a function of the phase series conductors N, the number of pole pairs p, the slots number Q, the stator diameter D_s and the slot opening angle α_o (in mechanical radians). To derive the $\hat{n}_d$ formula, first, the conductors for phase and for pole are given by

$$n_{cs} \cdot q = n_{cs} \frac{Q}{3 \cdot 2p} = \frac{3N}{Q} \frac{Q}{3 \cdot 2p} = \frac{N}{2p} \tag{5.2}$$

where n_{cs} is the number of equivalent series conductors in one slot, and q is the number of slots for phase and for pole. In a circle arc of $\frac{D_s}{2} d\theta$ there are $n_{da}(\theta) \frac{D_s}{2} d\theta$ conductors. The integral over one pole, from 0 to π electric radians, of $n_{da}(\theta) \frac{D_s}{2} d\theta$ must be equal to the conductors for phase and for pole calculated above:

$$\begin{aligned} \frac{N}{2p} &= \int_0^{\pi} n_{da}(\theta_e) \frac{D_s}{2} d\theta_e \\ &= \int_0^{\pi} \hat{n}_d K_a(\theta_m) slots(\theta_m) \frac{D_s}{2} d\theta_e \\ &= \int_0^{\alpha_o} \hat{n}_d \frac{D_s}{2} q d\theta_m \\ &= \hat{n}_d \frac{D_s}{2} q \alpha_o \end{aligned} \tag{5.3}$$

where θ_e is the electric angle. Finally, the amplitude of the conductors function can be calculated as

$$\hat{n}_d = \frac{N}{2p} \frac{2}{D_s} \frac{1}{q \alpha_o} \tag{5.4}$$

The motor is fed by a three-phase system of symmetric sinewave currents [12], that are linked to the rotor position θ_r, and can be expressed as

$$\begin{aligned} i_a(\theta_r, \alpha_{ie}) &= \hat{I} cos(p\theta_r + \alpha_{ie}) \\ i_b(\theta_r, \alpha_{ie}) &= \hat{I} cos(p\theta_r + \alpha_{ie} - \frac{2\pi}{3}) \\ i_c(\theta_r, \alpha_{ie}) &= \hat{I} cos(p\theta_r + \alpha_{ie} - \frac{4\pi}{3})) \end{aligned} \tag{5.5}$$

where $\hat{I}$ is the peak phase current, and α_{ie} is the initial current angle of the a-

phase. For simplicity the rotor will be aligned with the a-phase, thus $\theta_r = 0$. Note that with this definition the functions $slots(\theta_m)$,$K_a(\theta_m)$,$K_b(\theta_m)$,$K_c(\theta_m)$ must be properly aligned to have the a-axis on the position $\theta_m = 0$.

The phase linear current densities (electric loads) are calculated as

$$\begin{aligned} K_{sa}(\theta_m, \alpha_{ie}) &= n_{da}(\theta_m) \cdot i_a(0, \alpha_{ie}) \\ K_{sb}(\theta_m, \alpha_{ie}) &= n_{db}(\theta_m) \cdot i_b(0, \alpha_{ie}) \\ K_{sc}(\theta_m, \alpha_{ie}) &= n_{dc}(\theta_m) \cdot i_c(0, \alpha_{ie}) \\ K_s(\theta_m, \alpha_{ie}) &= K_{sa}(\theta_m, \alpha_{ie}) + K_{sb}(\theta_m, \alpha_{ie}) + K_{sc}(\theta_m, \alpha_{ie}) \end{aligned} \tag{5.6}$$

The total electric load $K_s(\theta_m, \alpha_{ie})$ can be rewritten using the Fourier series. Note that some windings can have the periodicity $t = MCD\{p, Q\} = 1$, so the Fourier series must be calculated all along θ_m, from 0 to 2π. Thanks to the alignment of the a-phase axis on $\theta_m = 0$ the sine terms correspond to the d-axis current, while the cosine terms changed in sign correspond to the q-axis current. The calculated Fourier coefficient of sines and cosines are respectively called $b_{k,Kd}$ and $a_{k,Kq}$. Finally, the electric loads (figure 5.2) can be expressed as

$$\begin{aligned} K_s(\theta_m, \alpha_{ie}) &= \sum_k^\infty \left[b_{k,Kd} \sin(k\theta_m) - a_{k,Kq} \cos(k\theta_m) \right] \\ K_{sd}(\theta_m, \alpha_{ie}) &= \sum_k^\infty b_{k,Kd} \sin(k\theta_m) \\ K_{sq}(\theta_m, \alpha_{ie}) &= -\sum_k^\infty a_{k,Kq} \cos(k\theta_m) \end{aligned} \tag{5.7}$$

The Fourier coefficients depends also on α_{ie}, but it is omitted for a reason explained in section 5.3.

Thanks to the Ampere law, the magnetic scalar potential can be calculated as [12]

$$U_s(\theta_m, \alpha_{ie}) = \int K_s(\theta_m, \alpha_{ie}) \frac{D_s}{2} d\theta_m \tag{5.8}$$

The electric load is composed by the two summations of sines and cosines, so the integral can be computed independently:

$$\begin{aligned} U_s(\theta_m, \alpha_{ie}) &= \int K_s(\theta_m, \alpha_{ie}) \frac{D_s}{2} d\theta_m \\ &= \frac{D_s}{2} \left[\int \sum_k^\infty b_{k,Kd} \sin(k\theta_m) d\theta_m + \int \sum_k^\infty -a_{k,Kq} \cos(kp\theta_m) d\theta_m \right] \\ &= \frac{D_s}{2} \left[\sum_k^\infty \int b_{k,Kd} \sin(kp\theta_m) d\theta_m + \sum_k^\infty -a_{k,Kq} \int \cos(k\theta_m) d\theta_m \right] \\ &= \frac{D_s}{2} \left[\sum_k^\infty \frac{b_{k,Kd}}{k} (-\cos(k\theta_m)) + \sum_k^\infty \frac{-a_{k,Kq}}{k} \sin(k\theta_m) \right] \\ &= \sum_k^\infty \frac{D_s}{2} \frac{-b_{k,Kd}}{k} \cos(k\theta_m) + \sum_k^\infty \frac{D_s}{2} \frac{-a_{k,Kq}}{k} \sin(k\theta_m) \end{aligned} \tag{5.9}$$

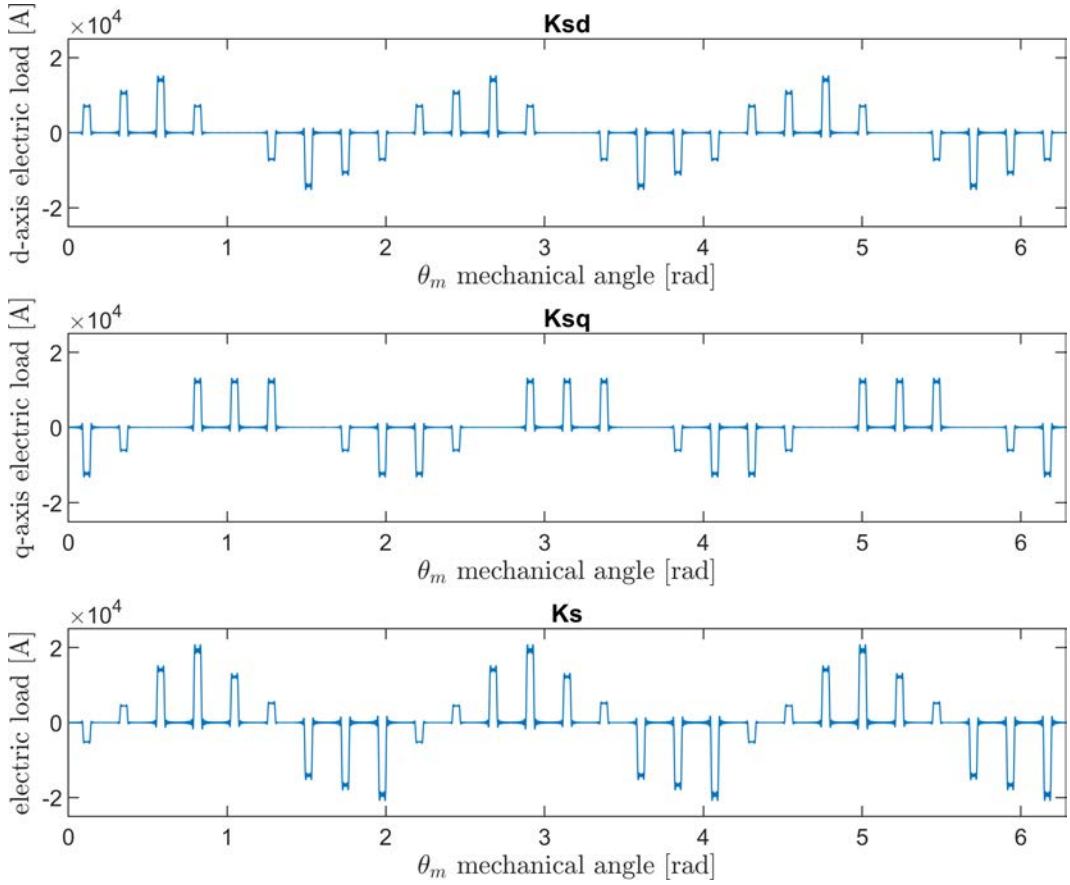

Figure 5.2: Electric loads of a Q=27 2p=6 motor, with $N = 50$, $D_s = 120\,mm$, $\alpha_o = 2.67°$, $\hat{I} = 10\,A$ and $\alpha_{ie} = 45°$

The coefficients of the magnetic potentials are

$$\begin{aligned} a_{k,Ud} &= \frac{D_s}{2}\frac{-b_{k,Kd}}{k} \\ b_{k,Uq} &= \frac{D_s}{2}\frac{-a_{k,Kq}}{k} \end{aligned} \tag{5.10}$$

Finally, the magnetic potentials produced by the d-axis and q-axis currents respectively can be expressed as

$$\begin{aligned} U_{sd}(\theta_m, \alpha_{ie}) &= \sum_k^{\infty} a_{k,Ud}\cos(k\theta_m) \\ U_{sq}(\theta_m, \alpha_{ie}) &= \sum_k^{\infty} b_{k,Uq}\sin(k\theta_m) \end{aligned} \tag{5.11}$$

5.2 Lumped parameters

Neglecting the distortion produced by the slot-openings, the magnetic flux density in the air gap is a function of the magnetic potentials difference respec-

tively of the stator U_s, calculated in (5.11), and of the rotor U_r:

$$B_s(\theta_m, \alpha_{ie}) = \frac{\mu_0}{g}(U_r - U_s(\theta_m, \alpha_{ie})) \tag{5.12}$$

where μ_0 is the magnetic permeability of free space and g is the air gap width.

The fluxes encounter the magnets in their path, so the magnetic potential U_r is not zero over the magnets islands. The calculation of this magnetic potential depends on the rotor geometry, and it is performed using the lumped-parameter magnetic circuit [12]. The rotor and stator iron is considered with infinite magnetic permeability, so the magnetic islands are at the same magnetic potential [12] and the system is linear. Since the analytical model must solve also fractional slots/poles combinations, the fluxes could not be equal in every pole pair, so the magnetic circuit must be extended to the whole rotor. The simple geometry of the radial magnetization rotor is initially considered to define the solving method.

5.2.1 Radial magnetization

In the radial magnetization geometry, there is a single magnet per pole with radial orientation, and it covers c_m portion of the pole. It results that the mechanical angle that covers the magnet is $2\alpha_m = c_m \cdot \pi/p$. The main geometrical dimensions are presented in the figure 5.3.

Starting with the dimensional data of the magnetic rib thickness t_{rib}, the stator diameter D_s, the coverage coefficient of the magnet c_{m2}, the magnet thickness t_m and the air gap width g, the other dimensional data are calculated as

$$\alpha_{m2} = \frac{\pi c_{m2}}{2p} \tag{5.13}$$

$$\begin{aligned} h_m &= 2 \cdot \frac{-b + \sqrt{b^2 - 4ac}}{2a} \qquad with \\ a &= 1 + \tan^2 \alpha_{m2} \\ b &= 2t_m \tan \alpha_{m2} \\ c &= [t_m^2 - (D_s/2 - t_{rib} - g)^2] \cdot \tan^2 \alpha_{m2} \end{aligned} \tag{5.14}$$

$$\alpha_m = \arcsin\left(\frac{2h_m}{D_s/2 - t_{rib} - g}\right) \tag{5.15}$$

$$c_m = \frac{2p\alpha_m}{\pi} \tag{5.16}$$

The rotor is divided in $4p$ slices (figure 5.4) and the rotor magnetic potential U_r is computed in each piece. Thus, the magnetic circuit is composed of $4p$ branches (figure 5.5), each of which represents one slice of the rotor. Two types of slices are identified: the one over the magnet m and the one over the iron i (figure 5.4). The fluxes of the m slices encounter both the magnet and the air gap reluctance, while the fluxes of the i slices encounter only the air gap reluctance.

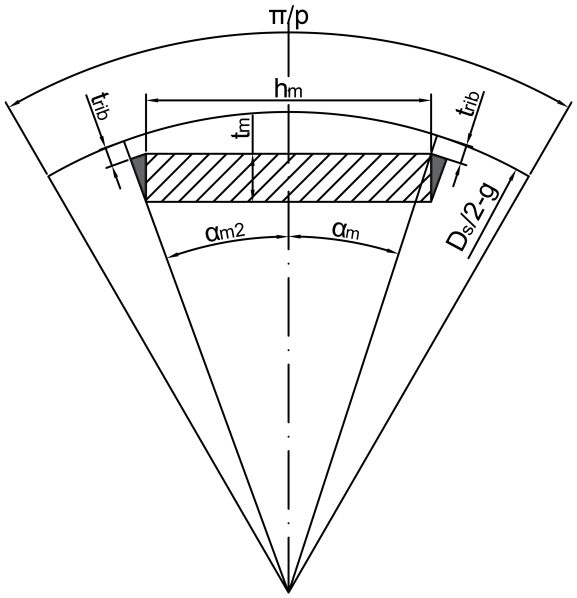

Figure 5.3: Single pole of the radial magnetization geometry with main dimensional data.

The hypothesis of constant magnetic potential, in the iron pieces, is used. Thus, the rotor magnetic potential is computed using the average value of the stator magnetic potential over these zones.

The air gap of the m slice has a width of $2\alpha_m$, while the air gap of the i slice has a width of $\pi/p - 2\alpha_m$. The respective reluctances are calculated with the average diameter of the air gap:

$$R_{gm} = \frac{g}{\mu_0 \alpha_m (D_s - g) L_{stk}} \tag{5.17}$$

$$R_{gi} = \frac{g}{\mu_0 (\frac{\pi}{2p} - \alpha_m)(D_s - g) L_{stk}} \tag{5.18}$$

The reluctance of the magnet is expressed as

$$R_m = \frac{t_m}{\mu_r \mu_0 h_m L_{stk}} \tag{5.19}$$

The reluctance of the k branch R_k is the sum of R_{gm} and R_m for m branches, and it is equal of R_{gi} for the i branches. After computing the average value of the stator magnetic potential $U_{s,AVG,k}$ in each slice, the solution of the magnetic circuit of $4p$ branches is found using the Millman theorem. The magnetic differential potential between A and B is

$$U_{AB} = \frac{\sum_{k=1}^{4p} \frac{U_{s,AVG,k}}{R_k}}{\sum_{k=1}^{4p} \frac{1}{R_k}} \tag{5.20}$$

The flux in each branch, with the direction indicated by the arrow in figure 5.5, is given by

$$\Phi_k = \frac{U_{AB} - U_{s,AVG,k}}{R_k} \tag{5.21}$$

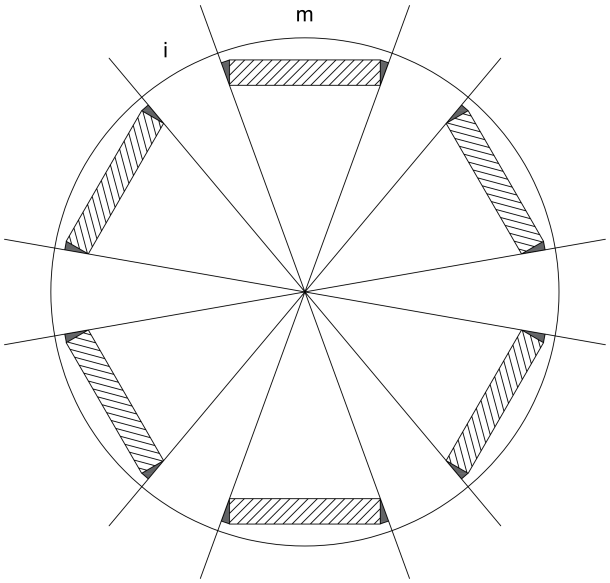

Figure 5.4: Radial magnetization 2p=6 IPM machine divided in slices.

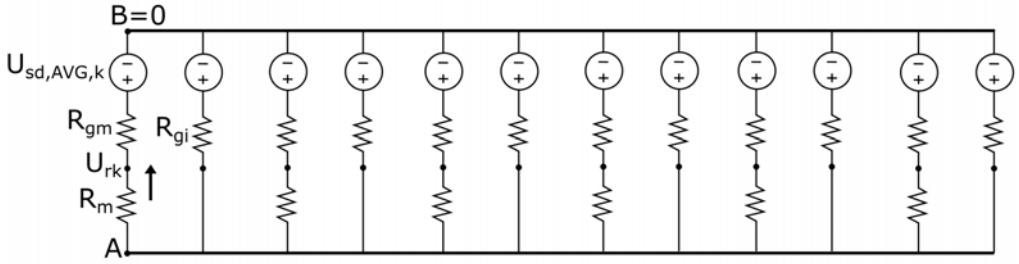

Figure 5.5: Magnetic circuit of radial magnetization 2p=6 IPM machine.

Finally, the rotor magnetic potential is computed as

$$U_{r,k} = U_{AB} - R_m \cdot \Phi_k \tag{5.22}$$

Note that R_m is equal to zero for the i branches, so it results that $U_r = U_{AB}$ for the i branches. The magnetic flux density in the air gap is computed as

$$B_s(\theta_m) = \frac{\mu_0}{g}(U_{r,k} - U_s(\theta_m)) \tag{5.23}$$

Thanks to the linearity of the system, the solving method can be applied independently to the d-axis and q-axis magnetic potential. So, the solutions are expressed as

$$\begin{aligned} B_{sd} &= \frac{\mu_0}{g}(U_{rd,k} - U_{sd}) \\ B_{sq} &= \frac{\mu_0}{g}(U_{rq,k} - U_{sq}) \end{aligned} \tag{5.24}$$

These functions can be decomposed with the Fourier series, and the property of only cosines for d-axis flux density and only sines for in q-axis flux density is maintained. The Fourier coefficients are calculated as

$$\begin{aligned} a_{k,Bsd} &= \frac{1}{\pi}\int_0^{2\pi} B_{sd}(\theta_m)\cos(k\theta_m)d\theta_m \\ b_{k,Bsq} &= \frac{1}{\pi}\int_0^{2\pi} B_{sq}(\theta_m)\sin(k\theta_m)d\theta_m \end{aligned} \tag{5.25}$$

The computation of the magnetic flux density produced by the magnet is easier because the fluxes are perfectly balanced and periodic. Thus, the magnetic circuit can be solved only for a single pole. The magnet is represented by a magnetic flux source

$$\Phi_{rem} = B_{rem} h_m L_{stk} \tag{5.26}$$

in parallel with its reluctance R_m (5.19). The iron ribs, which have a mechanical purpose, represent a leakage flux for the magnet. The leakage flux remains in the rotor so it does not change the air gap flux density. It is assumed that the ribs are saturated by the magnet at a constant magnetic flux density B_{sat}. This hypothesis allows making the problem linear, having no dependence on the B-H curve [12]. The leakage flux of a single rib can be expressed as

$$\Phi_{rib} = B_{sat} t_{rib} L_{stk} \tag{5.27}$$

where t_{rib} is the rib thickness. Finally, the magnet air gap flux is calculated as

$$\Phi_g = \frac{R_m}{R_m + R_{gm}}(\Phi_{rem} - N_{rib}\Phi_{rib}) \tag{5.28}$$

where N_{rib} is the ribs number, that in the case of radial magnetization geometry is 2. Finally, the magnet air gap flux density is given by

$$B_{gm} = \frac{\Phi_g}{\alpha_m D_s L_{stk}} \tag{5.29}$$

The shape of the distribution of the magnet flux density is a modified square wave of width $2\alpha_m$. This distribution can be expressed by only cosine harmonics because the fluxes of the magnets are only of d-axis. Of particular interest is the p harmonic because is the one used to calculate the torque. Thanks to the shape simplicity of the distribution, it can be calculated as

$$B_{gmp} = \frac{4}{\pi} B_{gm} \sin(p\alpha_m) \tag{5.30}$$

Finally, the total air gap flux density is given by

$$B_{tot} = B_{gm} + B_{sd} + B_{sq} \tag{5.31}$$

An example solution is presented in figure 5.6.

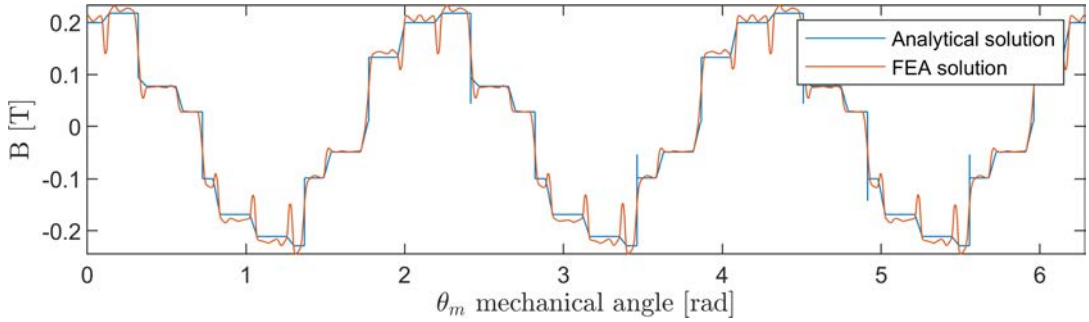

Figure 5.6: Comparison between analytical and FEA solutions of the total air gap flux density of a Q=27 2p=6 motor fed by $\alpha_{ie} = 45°$ currents.

5.2.2 V-shape

The same lumped parameters calculation can be used with a different rotor geometry: the v-shape. In this configuration, the single pole is formed by two tilted magnets like in figure 5.7. Thus, the two magnets of the v-shape configuration can be considered as a single magnet of the radial magnetization geometry split in half, with a height of $h_m/2$. The calculation of their height not only becomes more complex but also depends on the inclination angle β. The magnet coverage angle is calculated as

$$\alpha_{m2} = \frac{\pi c_{m2}}{2p} \tag{5.32}$$

To find an easier and faster solution, the flux-barrier on top of the magnet is approximated to the rectangular triangle $\overset{\triangle}{ABP}$. As a matter of fact, the cathetus

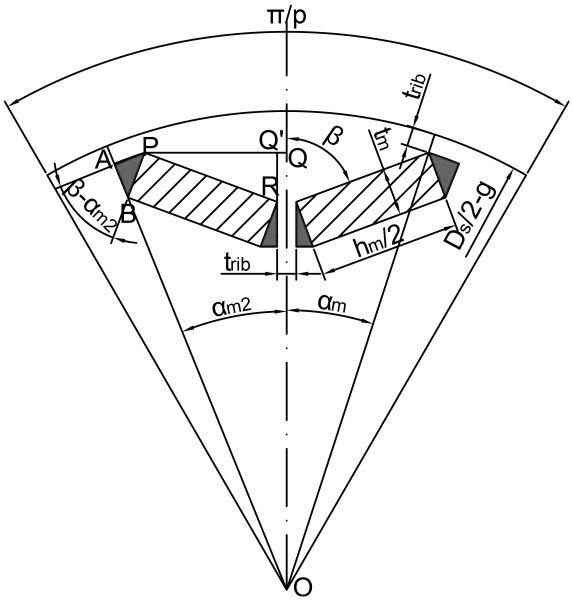

Figure 5.7: Single pole of the v-shape geometry with main dimensional data.

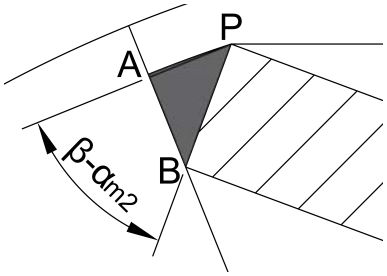

Figure 5.8: Detail of the approximated triangle of the v-shape geometry.

$\overline{AP}$ is about the same length of the little arc of the rib (figure 5.8). The angle between $\overline{BP}$ and $\overline{AP}$ is $\beta - \alpha_{m2}$. Using the difference between the arc of α_{m2} and the approximated little arc $\overline{AP}$, the arc of α_m is computed and α_m can be derived as

$$\alpha_m = \alpha_{m2} - \frac{t_m}{D_s/2 - g - t_{rib}} \cos(\beta - \alpha_{m2}) \tag{5.33}$$

The length of $\overline{PQ}$ can be computed considering the triangle $\overset{\triangle}{PQO}$. Then considering the triangle $\overset{\triangle}{PQ'R}$, the height of the magnet is calculated as

$$\frac{h_m}{2} = \frac{(D_s/2 - g - t_{rib}) \sin \alpha_m - t_{rib}/2}{\sin \beta} \tag{5.34}$$

Once α_m and h_m are calculated, the same equations described in the section 5.2.1 can be used. But, in the v-shape configuration there are 3 ribs instead of 2, so N_{rib} must be changed appropriately.

5.3 MTPA

The electrics loads K_{sd} and K_{sq} are proportional to the respective d-axis and q-axis currents and the number of conductors N. Thanks to the linearity of the magnetic circuit, the solutions B_{sd} and B_{sq} are also proportional to the currents and the number of conductors. So, the unitary solution found with $N^* = 1$, $\alpha_{ie}^* = \frac{\pi}{4}$, $\hat{I}^* = \sqrt{2}$ and so $I_d = I_q = 1$, can be easily used to find a generic solution:

$$\begin{aligned} B_{sd} &= B_{sd}^* N I_d \\ B_{sq} &= B_{sq}^* N I_q \\ K_{sd} &= K_{sd}^* N I_d \\ K_{sq} &= K_{sq}^* N I_q \end{aligned} \tag{5.35}$$

The possibility to calculate a generic solution for different I_d, I_q and N, gives the possibility to find the Maximum Torque Per Ampere point (MTPA). The maximum torque is found by imposing the current limit $\hat{I}^2 = I_d^2 + I_q^2$ and the number of conductors N. The torque T of an IPM motor is composed of two terms: the cylindrical torque T_{pm} and the reluctance torque T_{rel}. Neglecting the

torque ripple, both torques can be calculated using the p harmonics of flux density and electric load. The torques equations can be expressed as [12]

$$T_{pm} = \frac{\pi}{4} D_s^2 L_{stk} \hat{B}_{gmp} \hat{K}_{sqp} \tag{5.36}$$

$$T_{rel} = \frac{\pi}{4} D_s^2 L_{stk} (\hat{B}_{sdp} \hat{K}_{sqp} - \hat{B}_{sqp} \hat{K}_{sdp}) \tag{5.37}$$

$$T = T_{pm} + T_{rel} = \frac{\pi}{4} D_s^2 L_{stk} (\hat{B}_{gmp} \hat{K}_{sqp} + \hat{B}_{sdp} \hat{K}_{sqp} - \hat{B}_{sqp} \hat{K}_{sdp}) \tag{5.38}$$

Using the generic solutions defined in (5.35), also the p harmonics can be written as a function of the unitary solutions, the currents and the number of conductors. Thus, the total torque equation becomes

$$\begin{aligned} T &= \frac{\pi}{4} D_s^2 L_{stk} (\hat{B}_{gmp} K^*_{sq} N I_q + B^*_{sdp} K^*_{sqp} N^2 I_d I_q - B^*_{sqp} K^*_{sdp} N^2 I_d I_q) \\ &= \frac{\pi}{4} D_s^2 L_{stk} (\hat{B}_{gmp} K^*_{sq} N I_q + (B^*_{sdp} K^*_{sqp} - B^*_{sqp} K^*_{sdp}) N^2 I_d I_q) \end{aligned} \tag{5.39}$$

To obtain a more compact equation, the constant terms are gathered in:

$$\begin{aligned} n &= \hat{B}_{gmp} K^*_{sq} \\ m &= B^*_{sdp} K^*_{sqp} - B^*_{sqp} K^*_{sdp} \end{aligned} \tag{5.40}$$

$$T = \frac{\pi}{4} D_s^2 L_{stk} (n N I_q + m N^2 I_d I_q) \tag{5.41}$$

The maximum torque is obtained by imposing the derivative of the current I_d equal to zero:

$$\begin{aligned} \frac{dT}{dI_d} = 0 &= \frac{d}{dI_d} (n N I_q + m N^2 I_d I_q) \\ &= \frac{d}{dI_d} \left(n N \sqrt{\hat{I}^2 - I_d^2} + m N^2 I_d \sqrt{\hat{I}^2 - I_d^2} \right) \\ &= n N \frac{-I_d}{\sqrt{\hat{I}^2 - I_d^2}} + m N^2 \left[\sqrt{\hat{I}^2 - I_d^2} + \frac{-I_d^2}{\sqrt{\hat{I}^2 - I_d^2}} \right] \\ &= n \frac{-I_d}{\sqrt{\hat{I}^2 - I_d^2}} + m N \frac{\hat{I}^2 - 2 I_d^2}{\sqrt{\hat{I}^2 - I_d^2}} \\ &= -n I_d + m N (\hat{I}^2 - 2 I_d^2) \\ &= 2 m N I_d^2 + n I_d - m N \hat{I}^2 = 0 \end{aligned} \tag{5.42}$$

The solutions are

$$I_{d1,2} = \frac{-n \pm \sqrt{n^2 + 8 m^2 N^2 \hat{I}^2}}{4 m N} \tag{5.43}$$

The direct current of an IPM motor is negative, while $m < 0$ and $n > 0$, so, the

correct solution is the one with the plus:

$$I_d = \frac{-n + \sqrt{n^2 + 8m^2N^2\hat{I}^2}}{4mN} \tag{5.44}$$

Then, the q-axis current and the MTPA angle are calculated as

$$I_q = \sqrt{\hat{I}^2 - I_d^2} \tag{5.45}$$

$$\alpha_{ie,MTPA} = \arctan\left(\frac{I_q}{I_d}\right) \cdot \frac{180}{\pi} + 180 \tag{5.46}$$

5.4 Iron saturation

The hypothesis of infinite iron magnetic permeability leads to an overestimate of the actual air gap flux density and thus, an overestimate of torque. To account the magnetic voltage drop in the teeth and in the back-iron, a fictitious saturation coefficient is used [14]. This coefficient is used to reduce the air gap flux density, acting independently on every slot pitch section. This is not perfectly correct because the reduction of flux density in one slot pitch does not change the flux density in another one. In reality, the reduction of flux density due to magnetic voltage drop could lead to an increase of flux in another pole pitch section. Anyway, it guarantees to get the torque solution and the flux densities in the teeth and in the back-iron closer to the real ones. The fictitious saturation coefficient is expressed as

$$k_{sat} = \frac{H_g g + H_t h_t + H_{bi} l_{bi}}{H_{g(\mu=\infty)} g} \tag{5.47}$$

where $H_{g(\mu=\infty)}$ is the air gap magnetic field strength found with infinite iron permeability, H_g is the reduced air gap magnetic field strength, H_t is the teeth magnetic field strength, and H_{bi} is the back-iron magnetic field strength. The values of magnetic field strength in the teeth and in the back-iron sections depend on the distribution of the air gap flux density. Moreover, to find the values of H_g, H_t and H_{bi}, an iterative method must be used because of the non-linearity of the iron B-H curve.

First, the average air gap flux density in the k slot pitch (in front of the k tooth) is calculated as

$$B_g(k) = \frac{1}{\alpha_s} \int_{\theta_k - \frac{\alpha_s}{2}}^{\theta_k + \frac{\alpha_s}{2}} B_{tot}(\theta_m) d\theta_m \tag{5.48}$$

where α_s is the slot pitch angle, and θ_k is the mechanical angle of the center of the k tooth. Then, the average air gap magnetic field strength of the k slot pitch is expressed as

$$H_g(k) = \frac{B_g(k)}{\mu_0} \tag{5.49}$$

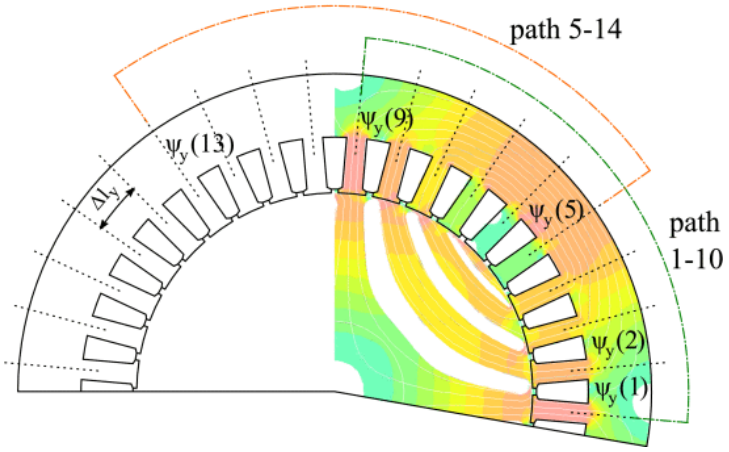

Figure 5.9: Sectioning of the back-iron. [14]

The k tooth flux density is computed as

$$B_t(k) = \frac{B_g(k)p_s}{w_t k_{stack}} \tag{5.50}$$

where p_s is the slot pitch, w_t is the tooth width and k_{stack} is the stacking coefficient of the laminations. The tooth magnetic field strength $H_t(k)$ is found by interpolating the B-H curve.

The flux density of the back-iron can be computed from the teeth flux density [14]. The sum of the fluxes of the teeth (with the sign) must be conserved in the back-iron. So, the flux of a section of the back-iron is the sum of all previous teeth fluxes minus the mean value of the back-iron fluxes. The section of the back-iron is considered as the portion between two teeth (figure 5.9). The back-iron section flux, before the mean value correction is calculated as

$$\tilde{\phi}_{bi}(k) = w_t L_{stk} \sum_{j=1}^{k} B_t(j) \tag{5.51}$$

The back-iron section flux corrected is calculated as

$$\phi_{bi}(k) = \tilde{\phi}_{bi}(k) - \frac{1}{Q} \sum_{j=1}^{Q} \tilde{\phi}_{bi}(j) \tag{5.52}$$

Finally, the flux density of the k back-iron section is given by

$$B_{bi}(k) = \frac{\phi_{bi}(k)}{h_{bi} L_{stk}} \tag{5.53}$$

The value of magnetic field strength $H_{bi}(k)$ is found by interpolating the B-H curve. The magnetic voltage drop of a single back-iron section is given by

$$\psi_{bi}(k) = H_{bi}(k)\Delta l_{bi} \tag{5.54}$$

where $\Delta l_{bi} = \frac{\pi(D_e - h_{bi})}{Q}$ is the length of the section. The corresponding magnetic voltage drop saw by one tooth is found by summing the magnetic voltage drops along the total flux line [14]. The flux lines do not have a constant length, especially if the motor has fractional slots. But considering the flux lines produced by the magnets, which are usually higher than the current ones, they flow for approximately a full pole $\sim \frac{Q}{2p}$. Finally, the magnetic voltage drop referred to a single tooth is calculated as [14]

$$\begin{aligned} \psi_{bi,t}(k) &= \left| \frac{1}{2} \sum_{j=k}^{k+\frac{Q}{2p}-1} H_{bi}(j) \Delta l_{bi} \cdot sign(\phi_{bi}(j)) \right| \\ &= \Delta l_{bi} \left| \frac{1}{2} \sum_{j=k}^{k+\frac{Q}{2p}-1} H_{bi}(j) \Delta l_{bi} \cdot sign(\phi_{bi}(j)) \right| \end{aligned} \tag{5.55}$$

The equivalent magnetic field strength of a single back-iron section referred to the tooth is the term in the module:

$$H_{bi,t}(k) = \left| \frac{1}{2} \sum_{j=k}^{k+\frac{Q}{2p}-1} H_{bi}(j) \cdot sign(\phi_{bi}(j)) \right| \tag{5.56}$$

Thus, the corresponding magnetic voltage drop of the back-iron referred to the tooth can be expressed also as

$$\psi_{bi,t}(k) = \Delta l_{bi} H_{bi,t}(k) \tag{5.57}$$

Finally, the fictitious saturation factor of the k tooth can be calculated as

$$k_{sat}(k) = \frac{H_g(k)g + H_t(k)h_t + H_{bi}(k)\Delta l_{bi}}{H_{g,\mu=\infty}(k)g} \tag{5.58}$$

To obtain the correct saturation factor, the process must be iterated. The solver is reliable and fast thanks to a weighted average with the previous value of k_{sat}, and to a random deviation used for relaxation and improve the converge stability [14]:

$$\begin{aligned} k_{sat,m+1}(k) =& 0.15 \cdot \frac{H_g(k)g + H_t(k)h_t + H_{bi}(k)\Delta l_{bi}}{H_{g,\mu=\infty}(k)g} + 0.85 \cdot k_{sat,m}(k) + \\ &+ 0.4 \cdot rand \cdot (k_{sat,m}(k) - k_{sat,m-1}(k)) \end{aligned} \tag{5.59}$$

In every iteration, the total flux density is corrected

$$B_{tot,m+1} = \frac{B_{tot,\mu=\infty}}{k_{sat,m+1}} \tag{5.60}$$

and used to calculate the teeth and back-iron flux densities.

Finally, the fictitious saturation factor is applied separately to the solutions

B_{gm}, B_{sd} and B_{sq} as in the equation (5.60). Then, the p harmonics of these flux densities are calculated as in (5.25)

$$\begin{aligned} B_{gmp} &= \frac{1}{\pi}\int_0^{2\pi} \frac{B_{gm}(\theta_m)}{k_{sat}(\theta_m)}\cos(p\theta_m)d\theta_m \\ B_{sdp} &= \frac{1}{\pi}\int_0^{2\pi} \frac{B_{sd}(\theta_m)}{k_{sat}(\theta_m)}\cos(p\theta_m)d\theta_m \\ B_{sqp} &= \frac{1}{\pi}\int_0^{2\pi} \frac{B_{sq}(\theta_m)}{k_{sat}(\theta_m)}\sin(p\theta_m)d\theta_m \end{aligned} \tag{5.61}$$

The torque is again calculated with (5.38).

5.5 Weight

In this section, the description of the motor geometry is completed, starting by the values of D_s, D_e, L_{stk}, h_{bi}, w_t, Q, J and $\hat{I}$. Once all the geometrical parameters are defined, the weight of the motor is calculated. It will be used to calculate the losses and finally, to evaluate the optimal geometry during the genetic algorithm optimization.

5.5.1 Stator geometry

The tooth height h_t is calculated as

$$h_t = \frac{D_e - 2h_{bi} - D_s}{2} \tag{5.62}$$

Then, the slot area can be derived, but it is partially occupied by the teeth tips, the slot-opening and the fittings between the teeth and the back-iron. The average value of use of the gross space for the slot is calculated starting from the data taken by multiple IEC stator laminations of similar diameter (D_s between $40\,mm$ and $55\,mm$). From these data, an average coefficient of use

$$k_{trap} = \frac{S_{slot}}{A} = 94.6\% \tag{5.63}$$

is obtained, where S_{slot} is the effective slot section and A is the gross space for the slot. A can be geometrically calculated as

$$A = \frac{\pi}{4}[(D_e - 2h_{bi})^2 - D_s^2]/Q - wt \cdot h_t \tag{5.64}$$

Using the slot area S_{slot}, the peak current $\hat{I}$ and the current density J, the number of conductors are calculated as

$$N = \frac{Q}{3}\frac{\sqrt{2}}{\hat{I}} J S_{slot} k_{fill} \tag{5.65}$$

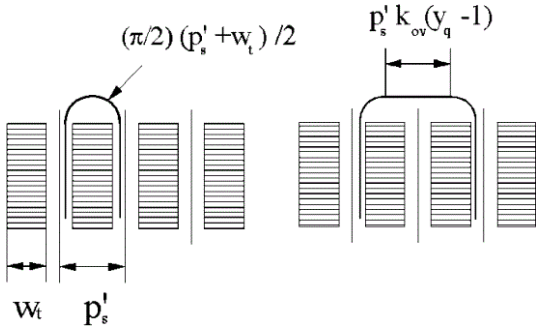

Figure 5.10: End-winding length with $y_q = 1$ and $y_q = 2$. [15]

where k_{fill} is the filling factor of the slot. Furthermore, the external slot width can be approximately calculated as

$$w_{se} = \pi(D_s + 2h_t)/Q - w_t \tag{5.66}$$

The end-winding length can be calculated as [15] (figure 5.10)

$$L_{ew} = \frac{\pi}{2}\frac{p'_s + w_t}{2} + p'_s k_{ov}(y_q - 1) \tag{5.67}$$

where $p'_s = \frac{\pi(D_s+h_t)}{Q}$ is the slot pitch calculated in the middle of the slot, $y_q \geq 1$ is the coil pitch (in number of slots) and $k_{ov} \simeq 1.8$ is an increasing factor for windings with $y_q > 1$. The coil pitch is calculated with the following formula rounded down to a minimum value of 1

$$y_q = floor\left(\frac{Q}{2p}\right) \tag{5.68}$$

5.5.2 Volumes and weights

The volumes (V) and the weights (G) of the motor parts can be expressed as:

- Back iron:

$$\begin{aligned} V_{febi} &= \frac{\pi}{4}[D_e^2 - (D_e - 2h_{bi})^2)L_{stk}k_{stack} \\ G_{febi} &= \gamma_{fe}V_{febi} \end{aligned} \tag{5.69}$$

- Teeth:

$$\begin{aligned} V_{fet} &= Qw_t h_t L_{stk}k_{stack} \\ G_{fet} &= \gamma_{fe}V_{fet} \end{aligned} \tag{5.70}$$

- Additional iron due to the coefficient of use:

$$\begin{aligned} V_{trap} &= (1 - k_{trap})AQL_{stk}k_{stack} \\ G_{trap} &= \gamma_{fe}V_{trap} \end{aligned} \tag{5.71}$$

- Winding:

$$\begin{aligned} V_{Cu} &= QS_{slot}k_{fill}(L_{stk} + L_{ew}) \\ G_{Cu} &= \gamma_{Cu}V_{Cu} \end{aligned} \tag{5.72}$$

- Winding resin:

$$\begin{aligned} V_{res} &= QS_{slot}(1 - k_{fill})L_{stk} \\ G_{res} &= \gamma_{res}V_{res} \end{aligned} \tag{5.73}$$

- Permanent magnet:

$$\begin{aligned} V_{pm} &= 2p \cdot t_m h_m L_{stk} \\ G_{pm} &= \gamma_{pm}V_{pm} \end{aligned} \tag{5.74}$$

- Rotor iron:

$$\begin{aligned} V_{fer} &= \left[\frac{\pi}{4}(D_s - 2g)^2 - 2p \cdot t_m h_m\right] L_{stk}k_{stack} \\ G_{fer} &= \gamma_{fe}V_{fer} \end{aligned} \tag{5.75}$$

where $\gamma_{fe}, \gamma_{pm}, \gamma_{Cu}, \gamma_{res}$ are respectively the densities of iron, magnets, copper and winding resin. Finally, the total weight of the slotted motor is the sum of the weights of the parts:

$$G_{tot} = (G_{febi} + G_{fet} + G_{trap}) + G_{Cu} + G_{res} + G_{pm} + G_{fer} \tag{5.76}$$

5.6 Losses

In this section, the main losses of the slotted motor are calculated. The losses are used to evaluate the motor performance, and to verify that the thermal steady state is sustainable with respect to the chosen insulation class (section 2.1.3).

First, the mechanical losses are evaluated to see if they are negligible compared to the other main losses: the joule and iron losses. Regarding the iron losses, only the stator ones are calculated, because the rotor losses are usually lower, and moreover, they are difficult to calculate analytically.

5.6.1 Mechanical losses

The mechanical losses are estimated in the worst-case scenario, to see if their maximum value is comparable to the main losses. Two components of mechanical losses are considered: one produced in the air gap by the friction of moving air with the stator and the rotor, and one produced by the bearings.

Air gap losses

The air gap losses are calculated using the friction losses derived by the equations of a rotating cylinder [16]. The worst-case scenario is evaluated with the maximum speed of the rotor of $n_{max} = 20000\,rpm$, a maximum rotor diameter of $D_s = 70\,mm$, and a maximum length of $L_{stk} = 70\,mm$. The Couette–Reynolds number of the air at this velocity is calculated as

$$Re_g = \frac{\rho \omega r g}{\mu} = 2433 \tag{5.77}$$

where $\rho = 2.224\,kg/m^3$ is the air density, $\omega = \frac{20000 \cdot 2\pi}{60} = 2094\,rad/s$ is the rotor angular speed, $r = 0.035\,m$ is the rotor radius, $g = 0.5 \cdot 10^{-3}\,m$ is the air gap width, and $\mu = 2.345 \cdot 10^{-5}\,Pa \cdot s$ is the air dynamic viscosity at $140°C$. The friction coefficient for the Reynolds numbers between $500 < Re_g < 10^4$ is expressed as

$$C_f = 0.515 \frac{(g/r)^{0.3}}{Re_g^{0.5}} = 0.0026226 \tag{5.78}$$

Finally, the air gap losses are calculated with the theory of rotating cylinders, using a roughness coefficient of $k = 2.5$ that is for the axially slotted surfaces ($k = 1$ for the smooth surfaces):

$$P_{airgap} = k C_f \pi \rho \omega^3 r^4 L_{stk} = 44.2\,W \tag{5.79}$$

Even in the worst-case scenario, the air gap losses can be neglected compared to the motor power, that can reach about $35\,kW$. Moreover, the air gap losses are proportional to $\omega^{2.5}$, thus at the nominal speed of $10000\,rpm$ they are further reduced to $7.8\,W$.

Bearings losses

The bearings losses are computed following the SKF model of calculation of the bearings moment of friction [17]. Neglecting the sealing moment of friction, the total moment of friction can be expressed as the sum of the rolling moment M_{rr} and the sliding moment of friction M_{sl}:

$$M = M_{rr} + M_{sl}\,[Nmm] \tag{5.80}$$

The rolling moment of friction and its terms are expressed as

$$M_{rr} = \Phi_{ftag} \Phi_{rs} G_{rr} (\nu n)^{0.6} \tag{5.81}$$

$$\Phi_{ftag} = \frac{1}{1 + 1.84 \cdot 10^{-9} (n d_m)^{1.28} \nu^{0.64}} \tag{5.82}$$

$$\Phi_{rs} = \frac{1}{e^{K_{rs} \cdot \nu n (d+D) \sqrt{\frac{K_z}{2(D-d)}}}} \tag{5.83}$$

$$G_{rr} = R_1 d_m^{1.96} F_r^{0.54} \tag{5.84}$$

where:

- Φ_{ftag} is the reduction factor due to heat up of cutting phenomena
- Φ_{rs} is the kinematic correction factor
- G_{rr} is the friction variable of the radial loading
- $\nu = 68\,\frac{mm^2}{s}$ is the grease viscosity
- $n\,[rpm]$ is the rotational speed
- $d\,[mm]$ is the internal diameter of the bearing
- $D\,[mm]$ is the external diameter of the bearing
- $d_m = 0.5(d + D)\,[mm]$ is mean diameter of the bearing
- $K_{rs} = 6 \cdot 10^{-8}$ is the filling constant of the grease
- $K_z = 3.1$ is the geometric constant of the ball bearings
- $R_1 = 4.5 \cdot 10^{-7}$ is the rolling geometric constant
- $F_r\,[N]$ is the radial load

It is assumed to use two ball bearings, with $d = 20\,mm$ and $D = 32\,mm$, to hold the motor, which weighs $\sim 3\,kg$. Thus, each ball bearing holds half of the motor weight, which is equivalent to a radial load of $F_r \simeq 15\,N$. At the maximum speed of $20000\,rpm$, the rolling moment of friction results equal to $M_{rr} \simeq 0.80\,Nmm$.

The sliding moment of friction and its terms are expressed as

$$M_{sl} = G_{sl}\mu_{sl} \tag{5.85}$$

$$G_{sl} = S_1 d_m^{-0.26} F_r^{\frac{5}{3}} \tag{5.86}$$

where:

- G_{sl} is the sliding variable of the radial loading
- $\mu_{sl} \simeq 0.15$ is the sliding friction coefficient
- $S_1 = 3.5 \cdot 10^{-3}$ is the sliding geometric constant

With the same previous hypothetical ball bearing, it results $M_{sl} \simeq 0.02\,Nmm$.

The total moment of friction is $M = 0.82\,Nmm$, that, at the speed of $20000\,rpm$, produces $1.72\,W$ of losses that are clearly negligible.

5.6.2 Joule losses

The joule losses are computed using the imposed current density and the copper volume calculated in (5.72). The copper temperature is $165°C$ in the worst-case scenario, that is $15°C$ lower than the insulation class temperature [18]. The copper resistivity is refereed to the working temperature with the formula:

$$\rho_{Cu,165°C} = \rho_{Cu,20°C}(1 + \alpha_{Cu}(165 - 20)) \tag{5.87}$$

where $\rho_{Cu,20°C}$ is the copper resistivity at room temperature, and α_{Cu} is copper resistivity thermal coefficient. The joule losses can be calculated as

$$P_J = \rho_{Cu,165°C} J^2 V_{Cu} \tag{5.88}$$

5.6.3 Iron losses

The specific iron losses in the stator are calculated using the Steinmetz formula, with the hysteresis coefficient $k_{hyst} = 0.7$ and the eddy current coefficient $k_{ec} = 0.3$. The starting values are taken from the lamination steel data sheet: the specific iron losses $p^*_{B,f}$ at the frequency f^* and flux density B^*.

The iron losses depend on the frequency that is strongly dependent on the number of poles because the motor speed is fixed to the car speed. A higher number of poles increase the supply frequency needed, so the specific iron losses increase. On the other hand, a higher number of poles reduces the thickness of the back-iron, thus the back-iron volume and its total losses decrease. So, there is not a clear trend for the choice of the number of poles according to the iron losses. The Steinmetz formula is

$$p_{fe,B,f} = k_{hyst} \cdot p^*_{B,f} \left(\frac{B}{B^*}\right)^2 \left(\frac{f}{f^*}\right) + k_{ec} \cdot p^*_{B,f} \left(\frac{B}{B^*}\right)^2 \left(\frac{f}{f^*}\right)^2 \tag{5.89}$$

where f is the working frequency, and B is the maximum flux density of the teeth or of the back-iron. These values were previously calculated in section 5.4. Once the specific iron losses have been calculated with the Steinmetz formula, the total iron losses in the teeth and in the back-iron are computed with the increase factors of 2 and 1.5 respectively [18], due to the imperfections produced by the laminations machining:

$$\begin{aligned} P_{fet} &= 2 p_{fet} G_{fet} \\ P_{febi} &= 1.5 p_{febi} G_{febi} \end{aligned} \tag{5.90}$$

5.6.4 Total losses

Finally, the total losses are approximately the sum of the joule and stator iron losses:

$$P_{tot} = P_J + P_{fet} + P_{febi} \tag{5.91}$$

Then, the nominal power and the efficiency of the motor can be calculated as

$$P_{nom} = T \cdot \frac{\omega_{me}}{p} \tag{5.92}$$

$$\eta = \frac{P_{nom}}{P_{nom} + P_{tot}} \tag{5.93}$$

5.7 Feasibility check

In addition to the objectives of the slotted model (torque, weight and losses), the feasibility of the geometry must be verified. The three checks that are made are:

- **Thermal verification**: the motor must not exceed the insulation class temperature defined in section 2.1.3.
- **Speed verification**: the motor must reach the base speed defined in table 3.1.
- **Moment of inertia verification**: the motor must not exceed the moment of inertia defined in section 3.3.

5.7.1 Thermal verification

The feasibility of the motor thermal steady state is verified by checking the winding maximum temperature, that must not exceed the maximum insulation temperature ($165°C$). The thermal steady state is verified by assuming that the stator losses, including the end-windings losses, are dissipated only radially. The external water cooled surface has a constant temperature equal to the one of the water, that is $80°C$ and it was defined in section 2.1.3. As a matter of fact, the end-windings are enclosed inside the aluminium housing, that has stationary air inside. Thus, the main heat dissipation of the end-windings will be through the windings. The air gap losses are neglected because they are smaller compared to the stator losses, and they are also dissipated axially with an air exchange with the air enclosed in the housing. Thanks to these assumptions, the end-windings temperature will be the higher one and it is the only one checked.

The thermal model consists in an electrical circuit of resistances and current generators (figure 5.11). The resistances represent the thermal resistances of the stator parts, while the current generators represent the stator losses. Where the current generators are:

- P_{febi} are the losses in the back-iron,
- P_{fet} are the losses in the teeth,
- $P_c = P_J \frac{L_{stk}}{L_{stk}+L_{ew}}$ are the joule losses in the active parts of the winding,
- $P_{ew} = P_J \frac{L_{ew}}{L_{stk}+L_{ew}}$ are the joule losses in end-windings,

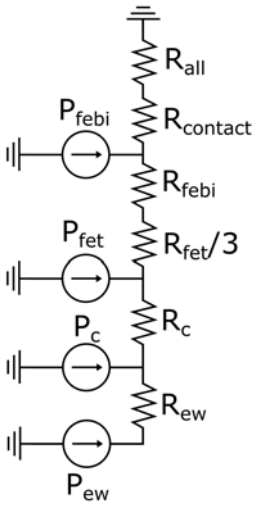

Figure 5.11: Equivalent electrical circuit of the thermal model of a slotted motor.

and the resistances are:

- R_{all} is the thermal resistance of the aluminium housing,
- $R_{contact}$ is the thermal contact resistance between the housing and the laminations,
- R_{febi} is the thermal resistance of the back-iron,
- R_{fet} is the radial thermal resistance of the teeth,
- R_c is the thermal resistance between the windings and the iron
- R_{ew} is the thermal resistance between the end-windings and the active parts.

The thermal resistance of the housing is calculated using the hollow cylinder formula:

$$R_{all} = \frac{1}{2\pi L_{stk}\lambda_{all}} ln\left(\frac{D_e + 2s_{all}}{D_e}\right) \tag{5.94}$$

where λ_{all} is the aluminium thermal conductivity, and s_{all} is the thickness of the aluminium housing.

The thermal contact resistance between the housing and the laminations is calculated with an equivalent air gap thickness of $s_{gap} = 0.01\,mm$ as reported in [19] for aluminium housings. The air gap is filled with air, that has a thermal conductivity of $\lambda_{air} = 0.026\,W/mK$. In reality, the assembly of the housing on the laminations is made with the help of thermal paste to reduce the thermal resistance. Despite this, air bobbles are unavoidable and thus, this equivalent configuration is considered. Finally, the thermal contact resistance is expressed as

$$R_{contact} = \frac{s_{gap}}{\lambda_{air}\pi D_e L_{stk}} \tag{5.95}$$

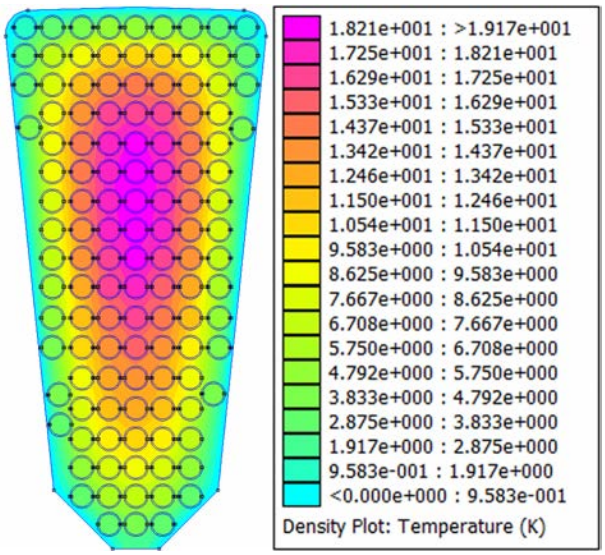

Figure 5.12: Thermal FEA of a hypothetical slot with constant temperature of the slot perimeter.

The thermal resistance of the back-iron is calculated using the hollow cylinder formula:

$$R_{febi} = \frac{1}{2\pi L_{stk}\lambda_{fe}} ln\left(\frac{D_e}{D_e - 2h_{bi}}\right) \tag{5.96}$$

The radial thermal resistance of the teeth is divided by 3 in the circuit (figure 5.11) because it takes account that not all heat from the slot goes through the entire length of the tooth, and also not all the tooth losses goes through its resistance. The radial thermal resistance of the teeth, without the reduction, is calculated as

$$R_{fet} = \frac{h_t}{\lambda_{fe} w_t L_{stk} Q} \tag{5.97}$$

The thermal resistance between windings and the laminations represents the complex system of the copper wires covered by the varnish and immersed in the winding potting. Moreover, the wires are at different temperatures. For this reason, an analytical model of this thermal resistance is too complicated to be found. An equivalent model [20][19] is used where all the copper wires are concentrated in the center of the slot, surrounded by a uniformly insulator that is the equivalent of the varnish and the winding potting. The thermal conductivity of this equivalent insulator is calculated using a thermal FEA with a real slot geometry (figure 5.12). The simulation is performed using a filling factor of $k_{fill} = 0.4$, a wire geometry taken by the conductors table of [18] and the following thermal conductivities of materials:

- $\lambda_{Cu} = 380\,W/mK$ is the copper thermal conductivity,
- $\lambda_{varnish} = 0.15\,W/mK$ is the varnish thermal conductivity,
- $\lambda_{potting} = 1.34\,W/mK$ is the winding potting thermal conductivity.

The slot perimeter is imposed at a constant temperature, because the laminations present a low temperature gradient along the perimeter thanks to his higher thermal conductivity. Furthermore, the temperature of the slot perimeter depends also on the teeth losses and on the teeth geometry, variables whose impact cannot be assessed. The slot thermal resistance is calculated with any heat sources in the copper wires, and measuring the temperature difference between the slot perimeter and the maximum temperature of copper. As a matter of fact, this problem is linear, thus, the ratio between the temperature difference and the heat power is constant, and it depends only on the slot geometry. Finally, the slot thermal resistance can be calculated as

$$R_c = \frac{T_c - T_{fe}}{P_J} \tag{5.98}$$

The thermal conductivity of the equivalent insulator can be computed as

$$\lambda_{iso} = \frac{s_{iso}}{R_c l_{slot} L_{stk} Q} \tag{5.99}$$

where l_{slot} is the slot perimeter and s_{iso} is the equivalent insulator thickness. They are calculated as

$$l_{slot} = w_{se} + 2h_t \tag{5.100}$$

$$s_{iso} = \frac{S_{slot}(1 - k_{fill})}{l_{slot}} \tag{5.101}$$

The thermal conductivity of the equivalent insulator depends on the filling factor, on the geometry, and also on the potting and varnish thermal conductivity. With the FEA thermal simulation performed in figure 5.12, the value of $\lambda_{iso} = 0.73\ \frac{W}{mK}$ is found, and it agrees with experimental values found in [20]. To account any air bubbles present in the potting, the thermal conductivity of the insulator is further reduced to $\lambda_{iso} \simeq 0.7\ \frac{W}{mK}$. Finally, the thermal resistances of the slot is expressed as

$$R_c = \frac{s_{iso}}{\lambda_{iso}(w_{se} + 2h_t) L_{stk} Q} \tag{5.102}$$

The thermal resistance between the end-windings and the active parts is calculated with the approximated formula [18]:

$$R_{ew} = \frac{L_{stk} + L_{ew}}{14 Q \lambda_{Cu} S_{Cu}} \tag{5.103}$$

Finally, the end-winding temperature can be calculated as the voltage drop on the resistances plus the housing external temperature:

$$\begin{aligned} T_{ew} =& T_w + (R_{all} + R_{contact}) \cdot (P_{ew} + P_c + P_{febi} + P_{fet}) + \\ & (R_{fet}/3 + R_{febi}) \cdot (P_{ew} + P_c + P_{fet}) + R_c \cdot (P_{ew} + P_c) + R_{ew} \cdot P_{ew} \end{aligned} \tag{5.104}$$

5.7.2 Speed verification

Once the number of conductors is calculated in (5.65), the base speed of the motor can be verified. It must be higher than the one defined in table 3.1. For simplicity of calculation, only the p-harmonic fluxes are considered. The concatenated fluxes of the currents and of the magnets are calculated as

$$\begin{aligned}\Lambda_d &= \frac{k_w N}{2}\Phi_d = \frac{k_w N}{2}\frac{D_s L_{stk}}{p}B_{sdp}\\ \Lambda_q &= \frac{k_w N}{2}\Phi_q = \frac{k_w N}{2}\frac{D_s L_{stk}}{p}B_{sqp}\\ \Lambda_{mg} &= \frac{k_w N}{2}\Phi_{mg} = \frac{k_w N}{2}\frac{D_s L_{stk}}{p}B_{gmp}\end{aligned} \tag{5.105}$$

Then, the maximum motor speed reached with the supply voltage U (calculated in (2.3)) is expressed as

$$\begin{aligned}\omega_B &= \frac{U}{\sqrt{\Lambda_q^2 + (\Lambda_{mg} + \Lambda_d)^2}}\\ &= \frac{U}{\frac{k_w N}{2}\frac{D_s L_{stk}}{p}\sqrt{B_{sqp}^2 + (B_{gmp} + B_{sdp})^2}}\end{aligned} \tag{5.106}$$

5.7.3 Moment of inertia verification

As explained in section 3.3, the moment of inertia of the motor can have a big impact on the car performance. Thus, its value must be checked to be lower than the limit found in section 3.3. The moment of inertia, formulated in (3.10), can be expressed for the slotted motor as

$$M_J = \frac{1}{8}(G_{fer} + G_{pm})(D_s - 2g)^2 \tag{5.107}$$

Chapter 6

Design variables

In this chapter, the entire exploration space of the genetic algorithm is defined. Exploration space in which the algorithm will search the optimal motor geometry. Thus, it is important to define properly the boundaries of the motor variables, to obtain a feasible and performing motor solution. The motor variables that change in the optimization are:

- the combination of the number of slots Q and the number of poles $2p$,
- the geometrical parameters of the stator: D_s, D_e, w_t, h_{bi},
- the geometrical parameters of the rotor: c_{m2}, t_m, β,
- the nominal current density J and the nominal current I_{nom}.

In addition, the air gap width and the rib thickness are defined. Lastly, the motor materials are chosen.

6.1 Slots and poles

An initial skimming of the slots/poles combinations must be performed because the combinations that have a bad behaviours, which are not evaluated through the slotted model, must be discarded. For example, a slots/poles combination could have good performance of torque, but an unsustainable torque ripple. Furthermore, the reduction of the number of combinations simplifies the comparison of the performances and reduces the computational time.

First, the range of the number of slots and the number of poles is defined. Considering the maximum supply frequency of the inverter $f_{max} \simeq 1670 Hz$, and the maximum motor speed to be achieved $n_{max} = 20000\, rpm$, the maximum number of pole pairs is then $\frac{f_{max} \cdot 60}{n_{max}} \simeq 5$. In addition, the minimum number of pole pairs is $p = 3$ because a lower number would increase too much the back-iron height. Thus, the chosen range of the number of poles is $2p = 6 \div 10$. Then, considering that the stator diameter will be about $60\, mm$, and that a slot pitch $p_s < 5\, mm$ is not reliable, the maximum number of slots is $\frac{\pi 60\, [mm]}{5\, [mm]} \simeq 36$. So, the chosen range of the number of slots is $Q = 9 \div 36$.

The behaviours of the slots/poles combinations are evaluated through the parameters explained in the following sections:

- Winding factor
- MMF THD
- Cogging torque
- Radial force
- Winding topology

6.1.1 Winding factor

The winding factor k_w influences the magnitude of the electric loading K_s and thus, the produced torque [21]. So, using a winding with $k_w < 1$ to obtain the same torque of an integer winding $k_w = 1$, the needed current must be $\frac{1}{k_w}$ higher, which results in copper losses $\frac{1}{k_w^2}$ higher. For example, a $k_w = 0.866$ could lead to a current 115.5% higher and copper losses 133.3% higher compared to an integer winding with $k_w = 1$. The winding factors of the slots/poles combinations are reported in table 6.1.

Q\2p	6	8	10
9	0.866	0.945	0.945
12		0.866	0.933
15		0.711	0.866
18	1	0.945	0.735
21		0.890	0.953
24		1	0.925
27	0.945	0.941	0.877
30		0.910	1
33		0.954	0.946
36	0.966	0.945	0.924

Table 6.1: Winding factors k_w of slots/poles combinations.

6.1.2 MMF THD

The MMF (Magneto Motive Force) produced by the winding is composed by many harmonics. The only one that produced the useful torque, is the main harmonic of order p, while the other harmonics cause rotor losses, torque fluctuations and waste the available voltage. The Total Harmonic Distortion (THD) of the MMF is calculated to evaluate qualitatively these phenomena (table 6.1). It is important to remember that the MMF produced by the magnets is usually higher than the winding one. Thus, the MMF distortion of the winding, evaluated by the THD, has a lower impact.

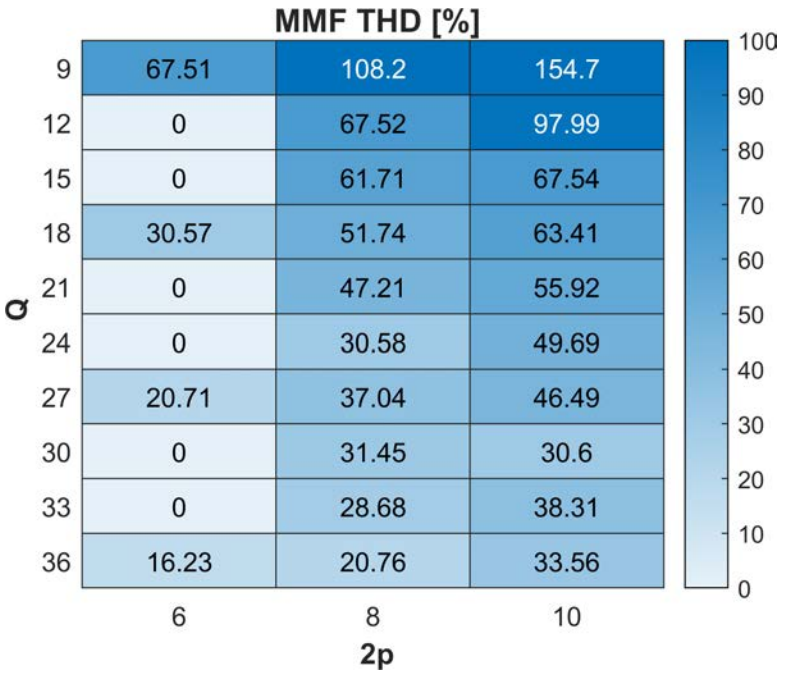

Figure 6.1: MMF THD of slots/poles combinations.

6.1.3 Cogging torque

The fundamental frequency order of the cogging torque can be found computing the Lowest Common Multiple (LCM) of the number of slots and the number of poles (table 6.2). Its frequency should be as high as possible. Furthermore, a high LCM value decreases qualitatively the amplitude of the cogging torque [21]. So, $LCM\{Q, 2p\}$ must be as high as possible.

Q\2p	6	8	10
9	18	72	90
12		24	60
15		120	30
18	18	72	90
21		168	210
24		24	120
27	54	216	270
30		120	30
33		264	330
36	36	72	180

Table 6.2: $LCM\{Q, 2p\}$, cogging torque fundamental frequency order of slots/poles combinations.

6.1.4 Radial force

The motor symmetry is indicated by the Greatest Common Divisor (GCD) of the number of slots and the number of poles (table 6.3). If the $GCD\{Q, 2p\}$ is even, the radial forces of the motor are better balanced. Thus, the $GCD\{Q, 2p\}$ must be even to have a low resulting radial force [21]. It is obvious that with odd number of slots it is impossible to obtain an even $GCD\{Q, 2p\}$.

Q\2p	6	8	10
9	3	1	1
12		4	2
15		1	5
18	6	2	2
21		1	1
24		8	2
27	3	1	1
30		2	10
33		1	1
36	6	4	2

Table 6.3: $GCD\{Q, 2p\}$, motor symmetry of slots/poles combinations.

6.1.5 Winding topology

The winding topology is distinct only in the Concentrated Winding (CW) configuration and the Distributed Winding (DW) configuration. To find the winding topology, the coil pitch is calculated as (5.68)

$$y_q = floor\left(\frac{Q}{2p}\right) \tag{6.1}$$

If $y_q = 1$, the winding has a CW configuration because the coil is wounded around the tooth. If $y_q > 1$, the winding has a DW configuration and there is an overlapping of coils. The CW configuration is nowday an attractive solution in automotive applications, thanks to the following advantages in respect to the conventional DW configuration [21]:

- Shorter end-windings, resulting in less copper weight and fewer joule losses. Furthermore, the total axial length of the motor is reduced, as shown in figure 6.2.

- Possibility to segment the stator to obtain a higher filling factor and a reduction of machine manufacturing cost.

- Higher inductance with the same magnet flux, that results in a better flux-weakening operation.

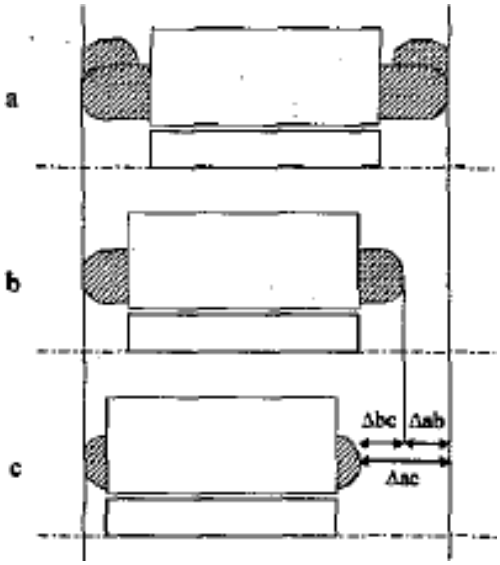

Figure 6.2: Comparison of axial end-winding length of: a)Distributed windings, b) Single-layer concentrated winding c) Double-layer concentrated winding [22]

On the other hand, as a disadvantage, the concentrated winding presents higher MMF spatial harmonic content that increases the rotor losses, the torque fluctuations and wastes the available voltage. The winding topologies of the slots/poles combinations are reported in table 6.4.

Q\2p	6	8	10
9	CW	CW	CW
12		CW	CW
15		CW	CW
18	DW	DW	CW
21		DW	DW
24		DW	DW
27	DW	DW	DW
30		DW	DW
33		DW	DW
36	DW	DW	DW

Table 6.4: Winding topology of slots/poles combinations: CW (Concentrated winding) and DW (Distributed winding)

6.1.6 Initial skimming

To avoid a poor NVH (Noise, Vibration, Harshness) behaviour due to asymmetrical radial force, usually the combinations with odd $GCD\{Q, 2p\}$ are discarded in automotive applications [21][23]. Using the same criteria, the combinations with $LCM\{Q, 2p\} < 50$ are eliminated to avoid low frequency and high amplitude cogging torques. Using the winding factor criteria, the combinations with $k_w < 0.8$ are eliminated. These criteria lead to the following remaining combinations:

2p	Q	k_w	MMF THD	Cogg. torque	Wind. topology
8	18	0.945	51.74	72	DW
	30	0.910	31.45	120	DW
	36	0.945	20.76	72	DW
10	12	0.933	97.99	60	CW
	24	0.925	49.69	120	DW
	36	0.924	33.56	180	DW

Table 6.5: Initial skimming of the slots/poles combinations

The combinations with $2p = 6$ have been eliminated completely due to their poor cogging torque and radial force behaviour.

The MMF THD and the winding topology have not been evaluated yet because their impact on the motor performance is relative. Once the torque and the losses of each slots/poles combination is presented, the MMF THD and the winding topology can be used to make the final choice. The star of slot and the winding scheme of each combination have been produced with the Dolomites software [24] and are reported in the appendix.

6.2 Boundaries

The boundaries of the motor variables are the lower and upper limit, within which the genetic algorithm looks for a solution. Thus, the boundaries must be as small as possible to find a reasonable solution with a reasonable computational time. Furthermore, the solution found will have the right overall dimensions. Anyway, a too small boundary range will cause the algorithm to converge to the boundary itself. In this case, the range can be fixed accordingly.

Stator diameter

The stator diameter range cannot be defined precisely, but values around $60\,mm$ are expected. So the range is arbitrarily chosen between $D_s = 50 \div 70\,mm$.

External diameter

The maximum external diameter of the housing must not exceed $96\,mm$ (section 2.1.1). The housing material chosen is aluminium, to ensure lightness and

good thermal conductivity. A minimum housing thickness of $1\,mm$ is defined by the competition rules. Finally, the chosen thickness is $1.5\,mm$ to provide a discrete mechanical resistance to accidental bumps.

The housing of the previous electric motor was $3\,mm$ thick. Considering the same external diameter and the same length, the new thickness halves the weight. In particular, the weight of the lateral part of the housing is reduced from $260\,g$ to $132\,g$ per motor, with a total reduction of $521\,g$ for the four motors. It is an important weight reduction for this race car type, in which a small reduction in each component can make a difference on the lap time results. Furthermore, it is an unsprung mass, that usually worsens the suspension dynamics.

Finally, the maximum external diameter is $D_e = 93\,mm$. The minim value is arbitrarily chosen to be $80\,mm$. The possibility of variation of the external diameter permits to evaluate if a lower value can be better than the maximum one.

Stack length

The motor stack length range cannot be defined precisely, but a value of $60\,mm$ is expected. So the boundaries are extended to $L_{stk} = 50 \div 70\,mm$.

Magnet coverage

The range of the magnet coverage c_{m2} must be chose properly to obtain the maximum flux in the air gap. As a matter of fact, the equation (5.30) indicates that the value of α_m must be as close as possible to $\frac{\pi}{2p}$. However, it must ensure a minimum space between the poles for the flow of the q-axis flux without saturation. On the other hand, the maximum magnet flux, obtained with the maximum value of c_{m2}, could not be the optimal geometry to minimize the losses. So, a reasonable range of $c_{m2} = 70 \div 85\%$ is chosen.

Magnet thickness

The magnet thickness range is chosen with the same criteria used for the Surface Permanent Magnet (SPM) motor. The SPM no load air gap flux density, considering an infinite iron magnetic permeability, can be easily calculated as

$$B_g = \frac{B_{rem}}{1 + \frac{\mu_r g}{t_m}} \tag{6.2}$$

where B_{rem} is the remanent flux density of the magnet, μ_r is the relative magnetic permeability of the magnet, t_m is the magnet thickness and g is the air gap width. The curve of this equation is presented in figure 6.3. To obtain an air gap flux density between $B_g = (0.75 \div 0.875)B_{rem}$, the magnet thickness range must be between $t_m \simeq (3 \div 7)g$. A high magnet thickness is not necessarily the best option because it would geometrically reduce the magnet height, thus also the total flux.

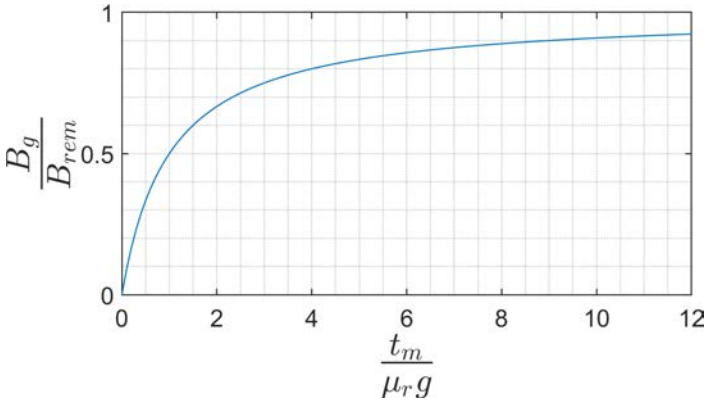

Figure 6.3: Flux densities ratio in function of the magnet thickness.

Magnet inclination

The maximum magnet inclination angle β is 90°, that is the radial magnet configuration but with a rib in between. Decreasing the inclination angle, the magnet height increases and so the magnet flux. Anyway, values lower than 25° are not geometrically feasible because the pole island would become too narrow and the magnet could impact the motor shaft.

Tooth width

The tooth width can be calculated starting from the expected values of the air gap flux density B_g and the flux density in the tooth B_t. The tooth width can be expressed as

$$w_t = \frac{B_g \pi D_s}{B_t Q} = \frac{B_g}{B_t} p_s \tag{6.3}$$

where p_s is the slot pitch. The expected values of the flux densities of electric motors are $B_g = 0.65 \div 1\,T$ and $B_t = 1.4 \div 1.8\,T$. Then, the tooth width boundaries are found in percentage of the slot pitch

$$w_t \simeq (0.35 \div 0.7) p_s \tag{6.4}$$

The tooth width of multiple IEC stator laminations (the same used in section 5.5.1) has the range $w_t \simeq (0.4 \div 0.5) p_s$. Anyway, the range is kept as it was calculated because the designed motor will have a higher power density and thus a wider range must be explored.

Back-iron height

The back-iron height can be calculated starting from the expected values of the air gap flux density B_g and the flux density in the back-iron B_{bi}. The back-iron height can be expressed as

$$h_{bi} = \frac{B_g \pi D_s}{B_{bi} 4p} \tag{6.5}$$

The expected values of the flux densities of electric motors are $B_g = 0.65 \div 1\,T$ and $B_{bi} = 1.3 \div 1.7\,T$. Then, the back-iron height boundaries are found in percentage of the stator diameter divided by the number of pole pairs:

$$h_{bi} \simeq (0.3 \div 0.6)\frac{D_s}{p} \tag{6.6}$$

Current density

The current density of a water-cooled PM motors can vary between $J = 10 \div 15\,A/mm^2$. The maximum current density does not necessarily correspond to the motor with the best performance. As a matter of fact, the joule losses grow with the square of the current density (5.88), moreover, the number of conductors depends on the current density (5.65).

Nominal current

As it was said in section 2.1.2, the motor nominal current depends on the ratio between the nominal torque and the maximum torque. The nominal torque upper value of table 3.1 is 45% of the maximum torque, while the inverter nominal current is 41% of the peak current. With these values, it is possible to achieve the requested performance. However, the small margin between the percentages of current and torque does not allow to operate in saturation as the torque must increase almost linearly with the current. Thus, to explore the possibility to operate with higher saturation, the rated current can vary between $35 \div 43\,A$. The $35\,A$ value, which is already one third of the maximum current, is not lowered further to avoid too much difference between the rated current and the peak current.

6.3 Constants

The values of the air gap width and of the rib thickness are maintained constants to simplify the optimization. Furthermore, their choice can be made to maximize the motor performance.

Air gap width

The air gap width of medium motors can range approximately from 0.015" to 0.020" [25], that is from $\sim 0.35\,mm$ to $\sim 0.5\,mm$ in the SI (International System of Units). Thanks to the choice of the small cogging torque and the small radial force, the air gap width can be minimized to $g = 0.35\,mm$.

Rib thickness

The rib thickness must be as small as possible because it represents a leakage flux for the magnet. However, it has the important mechanical purpose to connect the magnetic island to the rotor internal region. The main force that acts

on the magnetic island is the centrifugal force, while the electromagnetic force contributes for only $5 \div 10\%$ and can be neglected in the initial approximated sizing [26]. This analytical sizing is performed considering the static loading of the centrifugal force with a safety factor [26]. The magnetic island area of the figure 5.7 can be approximately calculated as

$$A_c = \alpha_m(D_s/2 - g)^2 + \frac{[(D_s/2 - g)\sin\alpha_m]^2}{\tan\beta} - (D_s/2 - g)^2 \sin\alpha_m \cos\alpha_m \quad (6.7)$$

Then, the centripetal radial force of the magnetic island is defined as

$$F_c = \gamma_{fe} A_c L_{stk} R_c \Omega^2 \quad (6.8)$$

where γ_{fe} is the steel density, R_c is the center of gravity radius and Ω is the mechanical speed of the rotor. Assuming that all the force is applied to the central rib, the rib thickness is calculated as [26]

$$\begin{aligned} t_{rib} &= k_s \frac{F_c}{\sigma_S L_{stk}} \\ &= k_s \frac{\gamma_{fe} A_c R_c \Omega^2}{\sigma_S} \end{aligned} \quad (6.9)$$

where k_s is the safety factor, and σ_S is the yield strength of the lamination steel. The rib thickness depends on many geometrical parameters. Thus, the rib thickness sizing is computed in the worst case scenario:

- low poles number $2p = 8$
- maximum magnet coverage $c_m \simeq 0.8$
- minimum magnet inclination angle $\beta = 25°$
- maximum motor speed $n_{max} = 20000\, rpm$
- expected stator diameter $D_s = 60\, mm$

Using these values, it results $A_c \simeq 197.8\, mm^2$. The center of gravity radius is approximately $R_c \simeq 23\, mm$. The yield strength of the lamination steel is $\sigma_S = 360\, MPa$. The safety factor used in [26] is 1.5. Finally, the rib thickness calculated with (6.9) is $t_{rib} \simeq 0.5\, mm$. The same rib thickness is also used for the two ribs near the air gap (figure 5.7). Once the optimal rotor geometry is obtained, the rib static load must be verified.

6.4 Materials

6.4.1 Electric steel

The choice of the electric steel takes into account the quality of the material but also the cost and the feasibility of the manufacturing. Thus, the chosen

electric steel is a conventional silicon steel alloy, which for example does not require complex manufacturing as opposed to the cobalt-iron alloys. The following electric steels have been considered:

	kA/m at 1.5T	**kA/m at 1.8T**	**W/kg at 1.5T 1000Hz**
HI-LITE NO10-1270N	1.5	10.5	86
HI-LITE NO18-1160H	1.52	12	95.5
HI-LITE NO20-1350N	1.4	9.8	112
SURA M235-35A	1.95	12	164
DI-MAX HF-10X	1.52	12.2	248
Powercore NO20-13	2.62	14	121
Powercore NO27-15	1.501	12.2	144.7

Table 6.6: Comparison between several silicon electric steels present on the European market

The best two electric steels are clearly the HI-LITE NO10 and NO20. The first minimize the losses at high frequency, the second minimize the magnetic field strength. In any case, the choice between these two steels cannot be done, because the NO10 steel is difficult to find on the market, thus, the more available NO20 is chosen.

6.4.2 Magnets

The most important characteristics of the permanent magnets are the resistance to demagnetization, the maximum working temperature and the remanent flux density. The latter must be as high as possible because it is strictly correlated to the torque density of the motor. Thus, the chosen magnet material is the neodymium-iron-boron (NdFeB) that, in the industry, is the most used material for high performances of torque and efficiency. The maximum working temperature must be at least $180°C$, that is the insulation class temperature chosen in section 2.1.3. The resistance of demagnetization is given by the intrinsic coercivity, which should be as high as possible to avoid the magnet demagnetizations even with high currents.

Finally, the chosen magnet is the Vacodym 974 TP of Vacuumschmelze GmbH & Co. KG. The main characteristics are reported in the table 6.7, where the magnetic relative permeability has been calculated as

$$\mu_r = \frac{B_{rem}}{\mu_0 H_{cB}} \tag{6.10}$$

Assuming that the magnets have a temperature 20 degrees lower than the maximum winding temperature that is $165°C$, the magnet properties at $145°C$

Vacodym 974 TP		
Remanence induction	B_{rem}	$1.28T$
Coercivity	H_{cB}	$980kA/m$
Intrinsic Coercivity	H_{cJ}	$2070kA/m$
Relative permeability	μ_r	1.0394
Energy density	$(BH)_{max}$	$315kJ/m^3$
Temperature coefficients $20 \div 150°C$	$\frac{\Delta B_{rem}}{\Delta T}$	$-0.102/\%°C$
	$\frac{\Delta H_{cJ}}{\Delta T}$	$-0.467\%/°C$
Maximum operating temperature	T_{max}	$200°C$
Density	γ_{pm}	$7700kg/m^3$

Table 6.7: Characteristics of Vacodym 974 TP at room temperature $20°C$

can be calculated as

$$\begin{aligned} B_{rem,145°C} &= B_{rem}\left(1+\frac{\Delta B_{rem}}{\Delta T}\cdot\frac{145-20}{100}\right) = 1.117T \\ H_{cB,145°C} &= \frac{B_{rem,145°C}}{\mu_0\mu_r} = 855kA/m \\ H_{cJ,145°C} &= H_{cJ}\left(1+\frac{\Delta H_{cJ}}{\Delta T}\cdot\frac{145-20}{100}\right) = 862kA/m \end{aligned} \tag{6.11}$$

Chapter 7

Genetic algorithm optimization

A first skimming of the slots and poles combinations has been performed in section 6.1. In this chapter, the final comparison is performed between the Pareto fronts of each slots/poles combination. The Pareto fronts are found using a genetic algorithm with the boundaries defined in chapter 6, except for the external diameter and the motor stack length that are fixed to simplify the comparison and to shorter the computational time. In addition, the comparison between the slotless and the slotted model performance are presented. Once the slots/poles combination is selected, the genetic algorithm optimization is performed, no longer holding constant the external diameter and the lamination stack length.

7.1 Genetic algorithm

The genetic algorithm (GA) is a search technique to find the minimum of a function. It is based on the principles of the genetics and the evolution of a population in a natural system. The input variables of the function are the genotypes of the individuals. The function results, that are the objectives to be minimized, represent the "fitness values" of the individuals.

First, an initial population is generated with random variables within the boundaries. Then, the objectives are calculated using the function and they are compared with each other. Because the objectives are more than one, the individuals who survive are those who have the best and unique combination of objectives. The following generation is produced by reusing the genome of the best individuals modifying with random mutation and cross-over of genotypes. The fitness evaluation is performed again and the process is iterated. Finally, the best individuals are saved in an archive and represent the obtained optimization.

The GA is used with the analytical models of the slotless and the slotted motors formulated in chapters 4 and 5. In particular, the variables and their boundaries of the slotted model are defined in section 6.2. The objectives to be optimized are the nominal torque, the maximum torque, the weight and the losses. The first two must be maximized, thus the negative values of torques are considered. The structure of the fitness function of the slotted model can be summarized in figure 7.1. In addition to the computation of the motor objectives, the three verification described in sections 5.7.1, 5.7.2 and 5.7.3 are performed. In

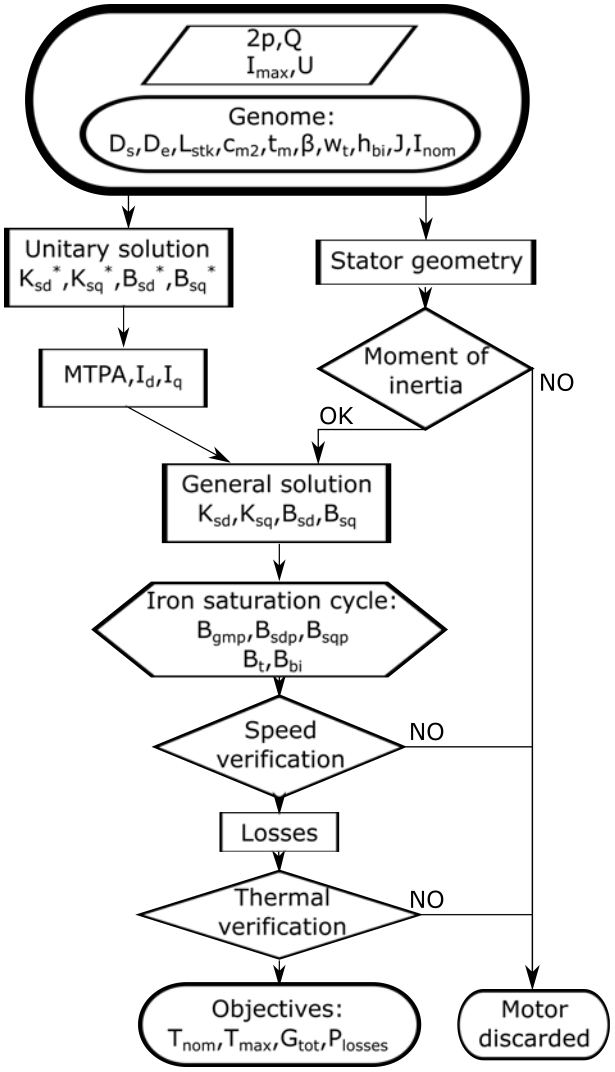

Figure 7.1: Structure of slotted model fitness function

case of the motor does not pass the checks, the individual is discarded imposing the maximum values of objectives.

7.2 Slots/poles selection

The comparison between different slots and poles combinations is performed fixing the external diameter to $D_e = 93\,mm$ and the stack length to $L_{stk} = 60\,mm$. Thus, the weight can be neglected. Moreover, to simplify further the comparison, only the nominal torque and the losses are evaluated. In this way, the computational time of each GA optimization is reduced and the comparison is easier and can be made on a bi-dimensional chart.

Since the external diameter and the stack length are fixed, the moment of inertia verification is not performed to avoid a distortion of the results. As a matter of fact, the inertia constraint limits the stator diameter that could generate a disparity between the slots/poles combinations whose optimized stator diameter

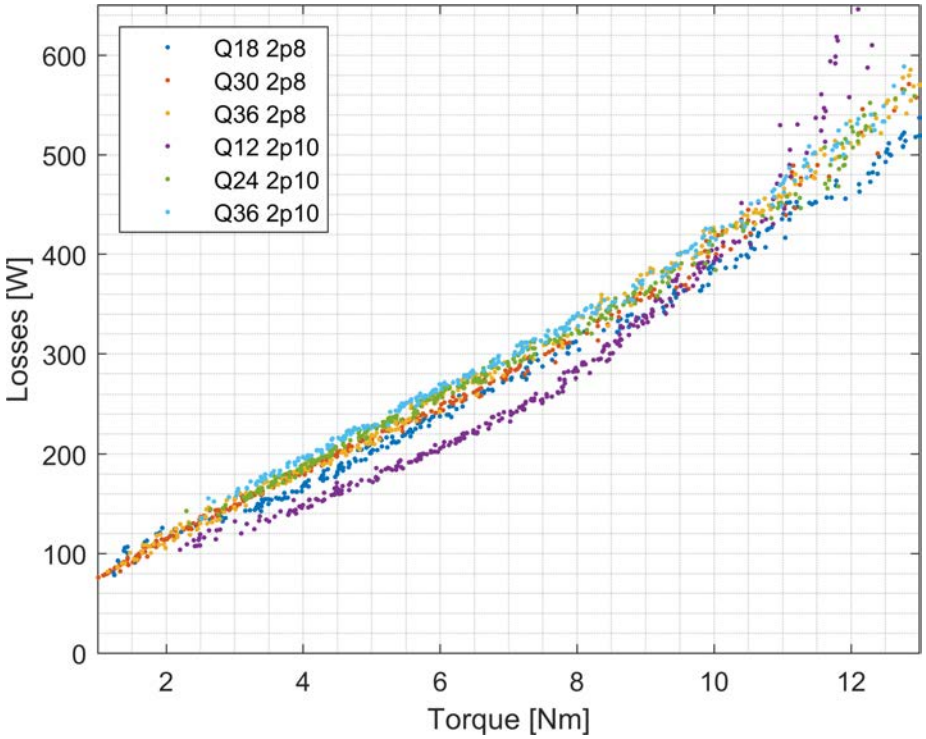

Figure 7.2: Nominal torque and losses Pareto fronts of different slots and poles combinations.

is different.

The found results are presented in figure 7.2. The losses grow linearly with the nominal torque, but at the end, the distribution tends to distort due to the thermal limit. The Pareto fronts of the slots/poles combinations are almost overlapped except for the 12/10 that presents better performance. Unfortunately, the thermal limit worsens the 12/10 Pareto front with a curvature. As a matter of fact, the 12/10 has bigger slots due to the smaller number of slots. Bigger slots have a greater difficulty to dissipate heat, and thus, the thermal limit is reached more easily. Finally, all combinations have approximately the same performance near the $9.8\,Nm$ objective.

The chosen combination is the 12/10 that, although presents the worst MMF THD and the worst cogging torque order, is the only CW topology (table 6.5). While the cogging torque $LCM\{Q, 2p\}$ is in any case greater than the defined minimum value, the CW advantages are believed to be greater than the disadvantage of the high MMF THD.

7.3 Slotless capability

The same comparison made between the slots and poles combinations is repeated between the chosen 12/10 and the slotless motor. As previously, only the nominal torque and the losses are evaluated. The optimization of the slotless motor is performed the first time with a fixed external diameter and a fixed stack length, and neglecting the moment of inertia. The second time, the limit of the

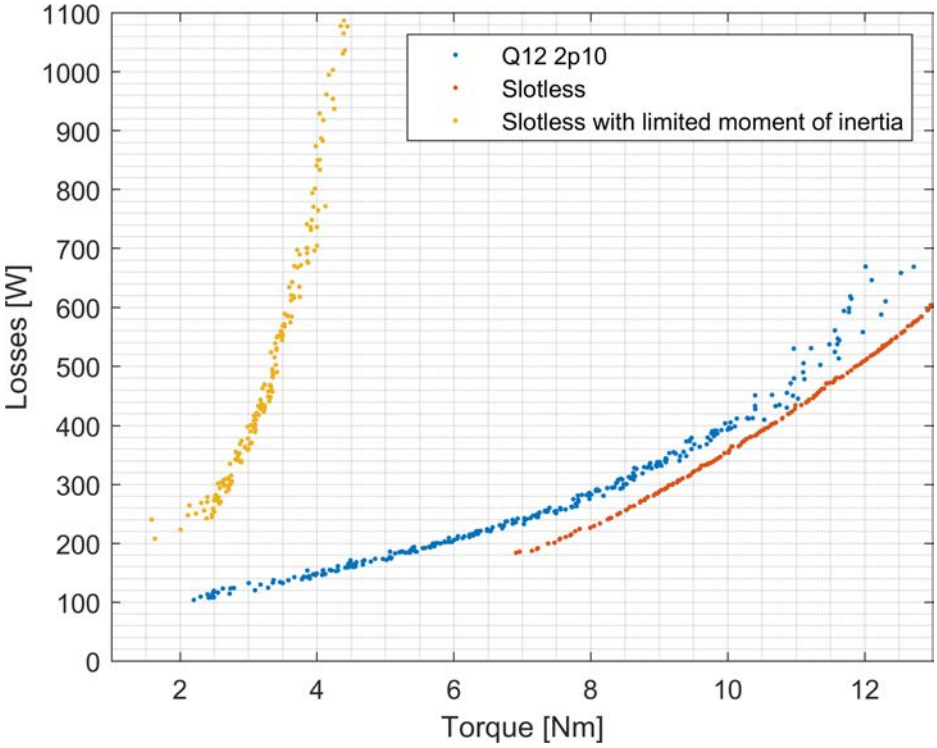

Figure 7.3: Nominal torque and losses Pareto fronts of the slotted 12/10, the slotless model and the slotless model with the moment of inertia limit.

moment of inertia, defined in section 3.3, is considered and the external diameter is free to change. Indeed, the moment of inertia has an important role in the slotless motor. Moreover, for this preliminary comparison, the thermal limit and the speed limit are not taken into account. The found results are presented in figure 7.3.

Neglecting the moment of inertia, the slotless motor has performances slightly better than the ones of the slotted motor. On the other hand, to achieve these performances the magnet volume is very high. As said in chapter 4, the high magnet volume, which increases the manufacturing cost, is not a problem because the motor performance have the priority. These good performances are achieved with a high stator diameter, that increases dramatically the motor moment of inertia. As a matter of fact, considering the moment of inertia limit, the torque achieved is much lower than the objective. To achieve the torque objective, the stack length should be increased by $3 \div 3.5$ times, which is not feasible. Thus, the slotted motor is chosen thanks to its low moment of inertia.

The question that spontaneously arises is if it is possible to use a slotless motor with a different gearbox ratio. As a matter of fact, the motor moment of inertia is multiplied by τ^2 as described by the equation (3.9). Thus, one might speculate that a motor with a higher torque and a higher moment of inertia could respect the limit while having better performance of the slotted motor. First, the wheel torque C, which is fixed and imposed by the car demanding, can be calculated as

$$C = constant = c \cdot \tau \tag{7.1}$$

where c is the motor torque, which is approximately proportional to the square of the stator diameter $c \propto D^2$ as described by the equation (5.38). Thus, the wheel torque is

$$C = constant \propto \tau \cdot D^2 \tag{7.2}$$

The motor moment of inertia depends on the diameter to the fourth $M_{J,m} \propto D^4$ as described by the equation (3.12). The motor moment of inertia reported to the wheel is

$$M_J = \tau^2 \cdot M_{J,m} \propto \cdot \tau^2 D^4 \tag{7.3}$$

However, the product $\tau \cdot D^2$ is constant due to (7.2), so even the equation (7.3) is constant. Thus, if the same drivetrain configuration is maintained, any slotless motor can not satisfy the inertia requirement. However, it could be possible to implement a slotless drivetrain with a different axial length or with a hollow rotor.

7.4 Final optimization

Once the slots and poles combination has been chosen, a final GA optimization can be performed of the four objectives: the nominal torque, the maximum torque, the weight and the losses. Finally, the external diameter and the stack length are free to change. Because of the fact that the objectives are four, the Pareto front can not be visualized in a chart with all the objectives. However, the torque objectives have been already defined in section 3.4, so the motors that do not satisfy these values can be simply discarded. In this way, the remaining individuals can be visualized in a weight and losses chart (figure 7.4). Since the slotted model overestimates the nominal torque and underestimates the maximum torque, as shown later in chapter 8, the nominal torque objective is increased by 10% and the maximum torque objective is reduced by 10%. Furthermore, due to the bigger tooth tips of the 12/10, the coefficient k_{trap} must be decreased to 0.9.

The results in figure 7.4 show the motors that minimize the weight and the losses at the bottom of the distribution. The points above are the motors that have a greater nominal and maximum torque. Since the torque objectives are already satisfied, there is no reason to take these geometries. The distribution shows that an increase of weight reduces the losses of about $50\,W$. Since the losses are already low compared to the AMK motor losses (about $1550\,W$, table 2.1), the chosen geometry is the one that minimize the weight (red star figure 7.4). The found set of values is reported in table 7.1.

The parameters are approximated to the first digit after the decimal point. The values of D_e, c_{m2} and β are approximated to their boundary. The ratios of the tooth width and back-iron height are first transformed to their values in mm and then are approximated.

With the found current density, according to (5.65), the number of conductors are $N \simeq 68.5$. The value of J must be approximated to obtain a round value of N, moreover, the number of series conductors in one slot must be even to allow the realization of a symmetric double-layer winding. The number of series

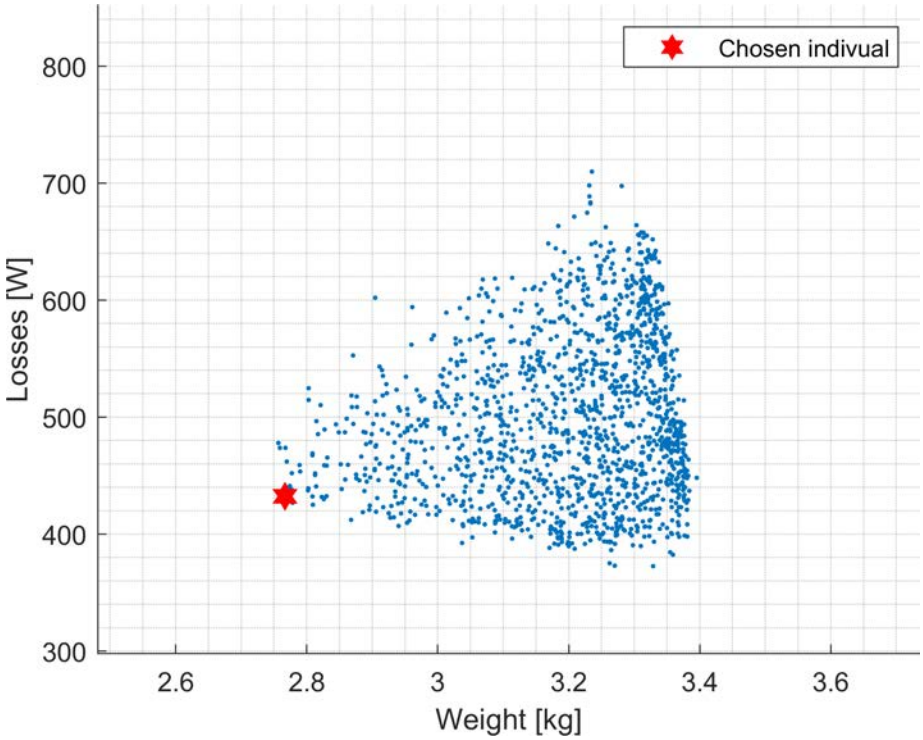

Figure 7.4: Weight and losses of 12/10 motor designs that satisfy the torque objectives.

conductors in one slot is calculated as

$$n_c = n_{pp} \cdot n_{cs} = n_{pp} \cdot \frac{3N}{Q} \tag{7.4}$$

where n_{pp} is the number of parallel paths. 10 poles winding can have $n_{pp} = 1$ or $n_{pp} = 5$ [18]. With $n_{pp} = 1$, the number of series conductors in one slot would be $n_c = 17.125$ and the conductor diameter would be

$$d_c = \sqrt{\frac{4}{\pi} S_c} = \sqrt{\frac{4}{\pi} \frac{S_{slot} k_{fill}}{n_{pp} n_{cs}}} \simeq 1.75\, mm \tag{7.5}$$

where S_c is the conductor cross section. Since the conductor diameter is already comparable to the copper penetration depth, that in the worst-case scenario ($n_{max} = 20000\, rpm$, copper at $20°C$) is

$$\delta = \sqrt{\frac{2\rho_{Cu.20°C}}{\omega \mu_0}} = \sqrt{\frac{2\rho_{Cu.20°C}}{\frac{2\pi p n_{max}}{60} \mu_0}} \simeq 1.6\, mm \tag{7.6}$$

the current inside the conductor is approximately evenly distributed, and there is no reason to further decrease the conductor size. Thus, $n_{pp} = 1$ is chosen to avoid complex connection between coils. So, $n_c = n_{cs}$ and the number of equivalent series conductors in one slot must be even. The number of conductors (7.4) can be approximated to the values reported in table 7.2. $N = 72$ is chosen because

Parameter	**Optimized**	**Approximated**
D_s	$60.6023\,mm$	$60.6\,mm$
D_e	$92.9833\,mm$	$93\,mm$
L_{stk}	$57.1171\,mm$	$57\,mm$
c_{m2}	0.8487	0.85
t_m	$2.3207\,mm$	$2.3\,mm$
β	$25.1693°$	$25°$
w_t/p_s	$0.4542 \rightarrow w_t = 7.2062\,mm$	$w_t = 7.2\,mm$
$h_{bi}/(D_s/p)$	$0.4937 \rightarrow h_{bi} = 5.9839\,mm$	$h_{bi} = 6\,mm$
I_{nom}	$35.7933\,A$	$35.8\,A$
J	$14.7214\,A/mm^2$	$15.48\,A/mm^2$

Table 7.1: Set of values of the chosen optimized design

n_c	N	$J\,[A/mm^2]$
16	64	13.76
18	72	15.48

Table 7.2: Approximation of the number of conductors.

it is the closer to the original value and does not cause a reduction of torque.

The value of I_{nom} is not the real thermal steady state current of the motor, but it is the value used to find the number of conductors with the imposed current of density and the nominal torque. Indeed, a higher current could be tolerated by the motor from the thermal point of view, so further analysis are necessary.

Chapter 8

Finite element analysis

In this chapter, referring to the obtained geometry with the GA optimization, the results of the Slotted Model (SM) are compared to the solutions that can be found with the Finite Element Analysis (FEA). In particular, the flux density, the torque and the thermal steady-state are evaluated, testing the reliability of the analytical model. Later, the torque ripple of the motor is computed, and a rotor shaping is performed to reduce it. Finally, the performance of the obtained geometry is calculated and compared to the AMK motor.

8.1 Obtained geometry

The found optimized geometry has been drawn in figure 8.1. In addition to the geometric parameters defined in table 7.1, the following construction elements has been added:

- The sharp corners has been rounded to avoid a concentration of mechanical stress. Furthermore, the slot sharp corners could damage the wire insulation.
- The tooth tip has been added to better convey the flux from the air gap. The shape should be drawn to avoid the iron saturation and to minimize the space stolen to the slot. Furthermore, the slot opening width must guarantee the insertion of the conductors.
- The magnet inclination angle β has been decreased to 24° to increase the available space for the magnet insertion. A minimum gap of $0.25\,mm$ is ensured on both magnet extremes. The shape of these gaps is drawn to maintain constant the rib thickness.

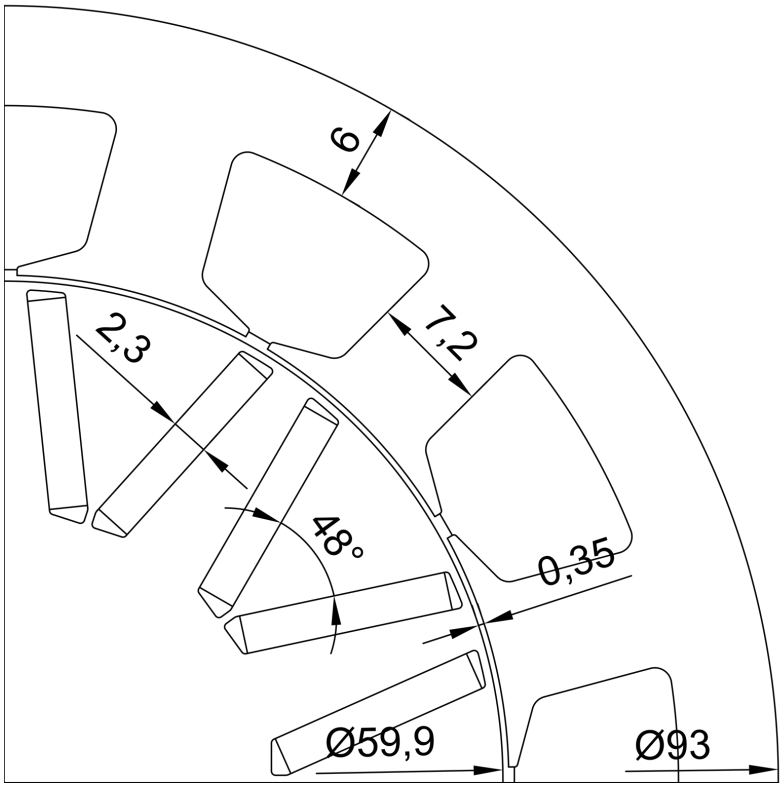

Figure 8.1: Optimized geometry with some additional construction elements.

8.2 Flux density

In this section, the flux density results of the SM and the FEA are compared. Indeed, by the flux density results are derived the calculation of the torque and the iron losses in the SM. Thus, three out of four objectives depend on the solving method of the motor flux density.

As expected, the SM solving method, which saturates the iron after finding the air gap flux density, has a solution different from the FEA one, as shown in figure 8.2. A perfect solution like in figure 5.6 is far from being achieved. Anyway, the SM found solutions are not completely wrong because the shape and the amplitude are similar to the FEA ones. This could result in a good evaluation of the torques and the losses.

The comparison is made also of the mean value of the teeth flux density defined in (5.50). The teeth are counterclockwise numbered starting from the orizontal axis in figure 8.1. The flux density results are reported in table 8.1. Since the teeth flux density presents a difference and the back-iron flux densities are derived from the latter, there is no reason to make this further comparison.

The calculation errors of the air gap and the teeth flux densities are attributable to several reasons:

- The iron saturation method: the fictitious saturation coefficient decreases only locally the flux density in each slot pitch. In reality, the saturation of one tooth or one back-iron section should change the solution of the whole

		$B_t(k)\,[T]$											
	k	1	2	3	4	5	6	7	8	9	10	11	12
$I = 35\,A$	SM	1.97	2.03	1.73	1.78	0.46	1.92	1.97	2.03	1.73	1.78	0.46	1.92
$\alpha_{ie} = 110°$	FEA	1.38	1.91	1.75	1.69	0.43	0.60	1.38	1.91	1.75	1.69	0.43	0.60
$I = 105\,A$	SM	2.26	2.28	0.92	1.25	1.09	2.49	2.27	2.28	0.92	1.25	1.09	2.45
$\alpha_{ie} = 110°$	FEA	2.02	2.07	1.40	0.81	1.24	2.00	2.02	2.07	1.40	0.81	1.24	2.00

Table 8.1: Teeth flux density of SM and FEA solutions with $I = 35\,A$ and $\alpha_{ie} = 110°$ and $I = 105\,A$ and $\alpha_{ie} = 110°$.

magnetic network. For example, the saturation of one tooth would deviate the fluxes to the adjacent teeth, causing their increase of flux density. Instead, the solution of the magnetic network is first found without the iron saturation, and then it is corrected with the fictitious saturation coefficient. This approximation is enhanced by the results of the teeth flux density in table 8.1: the teeth with high flux density have a higher value in the SM in respect to the FEA solution, while the adjacent teeth of high flux density tooth have a higher value in the FEA, thanks to the phenomena explained before.

- Only the saturation of the teeth and the back-iron sections is considered. In reality, also the rotor parts have a relevant flux density and so a magnetic voltage drop, as shown in figure 8.3.

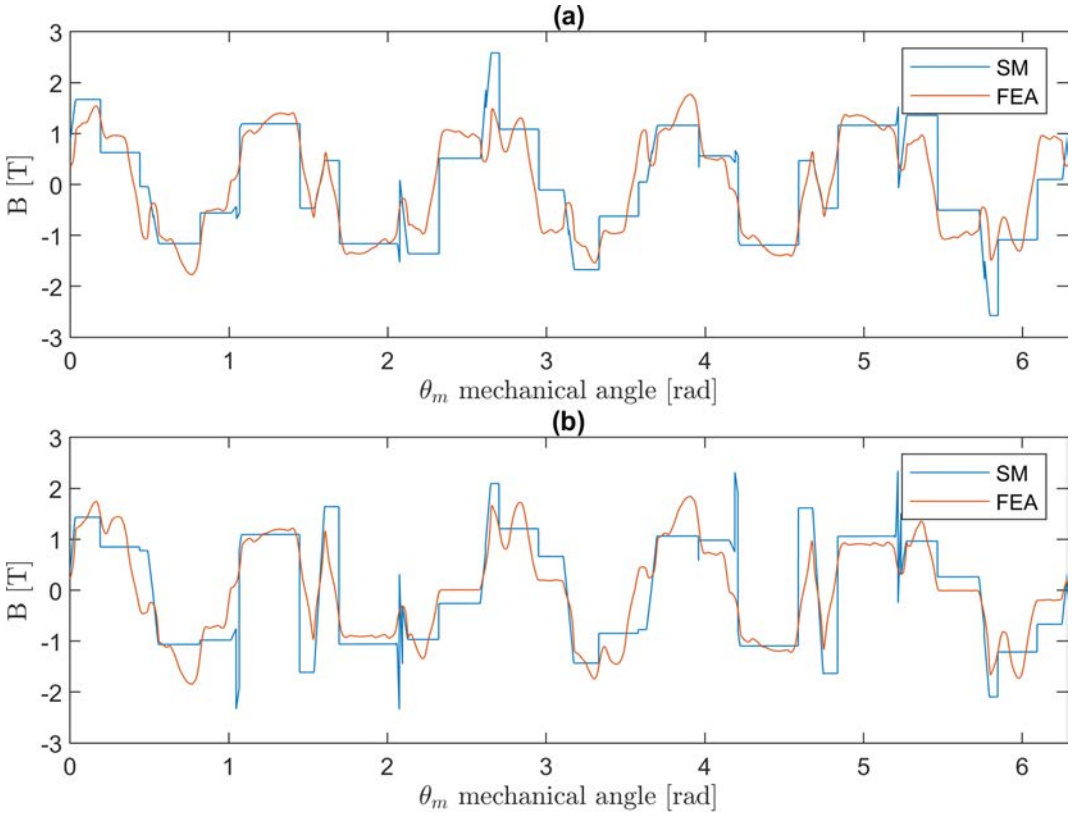

Figure 8.2: Comparison between SM and FEA solutions of the total air gap flux density with: (a) $I = 35\,A$ and $\alpha_{ie} = 110°$ and (b) $I = 105\,A$ and $\alpha_{ie} = 110°$.

	$I = 35\,A,\ \alpha_{ie} = 110°$		$I = 105\,A,\ \alpha_{ie} = 110°$	
	$\hat{B}_{dp}\,[T]$	$\hat{B}_{qp}\,[T]$	$\hat{B}_{dp}\,[T]$	$\hat{B}_{qp}\,[T]$
SM	1.0388	0.7295	0.6330	0.8765
FEA	1.2110	0.4136	0.8494	0.7372

Table 8.2: p harmonics of air gap flux density of SM and FEA with $\alpha_{ie} = 110°$, and $I = 35\,A$ or $I = 105\,A$.

- The flux density in the iron is assumed homogeneous. In reality, the local saturations cause a distortion of the air gap flux density. For example, the teeth tips or the iron parts near the magnets have a higher flux density (figure 8.3).

The difference between the SM and FEA flux density can be enhanced calculating the p harmonics, that are responsible for the generation of torque. The amplitude of the p harmonics of the d-axis and the q-axis are calculated as

$$\begin{aligned} \hat{B}_{dp} &= \frac{1}{\pi}\int_0^{2\pi} B(\theta_m)\cdot\cos(p\theta_m)d\theta_m \\ \hat{B}_{qp} &= \frac{1}{\pi}\int_0^{2\pi} B(\theta_m)\cdot\sin(p\theta_m)d\theta_m \end{aligned} \tag{8.1}$$

The values, found for both solution method, are reported in table 8.2. With both nominal and maximum current, the SM underestimate the d-axis flux density and overestimate the q-axis one.

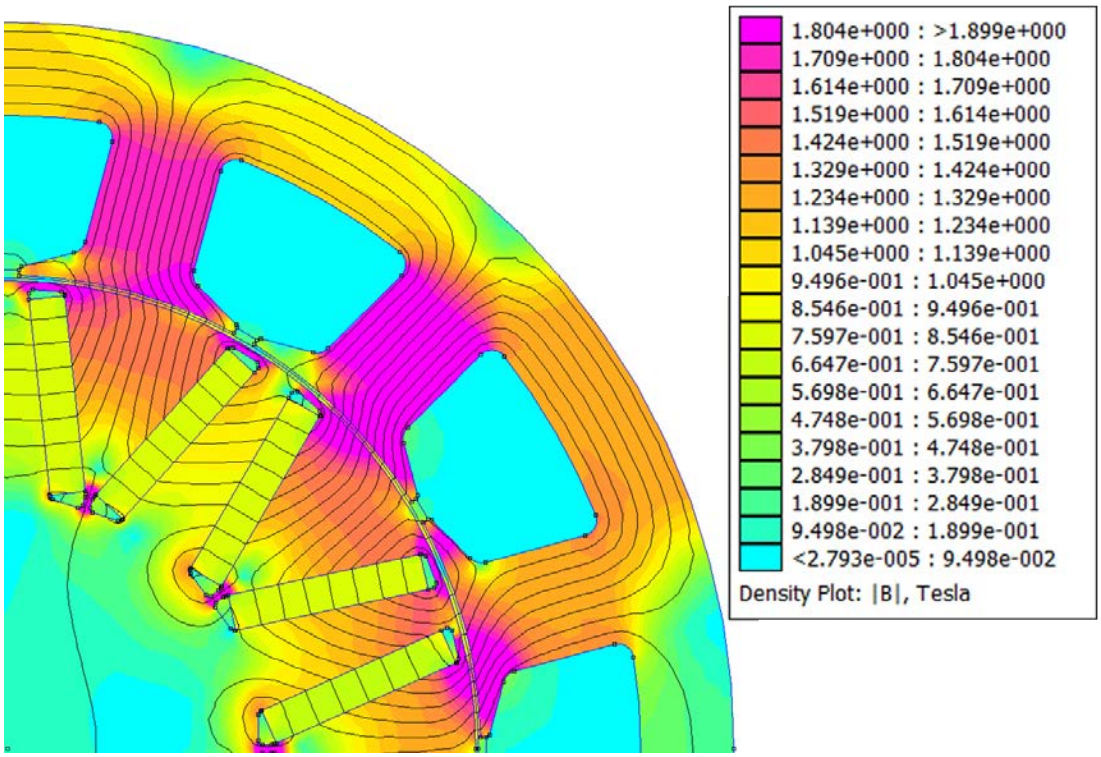

Figure 8.3: FEA flux density result with $I = 35\,A$ and $\alpha_{ie} = 110°$.

8.3 Torque

The reliability of the SM torque result is evaluated increasing the current from $0\,A$ to $105\,A$ and comparing the solutions to the FEA Maxwell stress tensor result (figure 8.4). First, the torque is obtained using the MTPA angle found by the SM (continuous line), and then with the MTPA angle found by the FEA. Although the MTPA angles found by the two different methods present a big difference (figure 8.5), the torque results are similar for each method. Thus, the MTPA point found neglecting the saturation, could be a reliable method to approximate the MTPA torque. Instead, the comparison between the SM and FEA torques present a relevant difference. Near the nominal current, the SM torque is about 9% higher than the FEA. At higher currents, this difference reverses and the SM underestimates the torque by 14%. These differences were taken into account in the final optimization of section 7.4, increasing and decreasing the torque objectives.

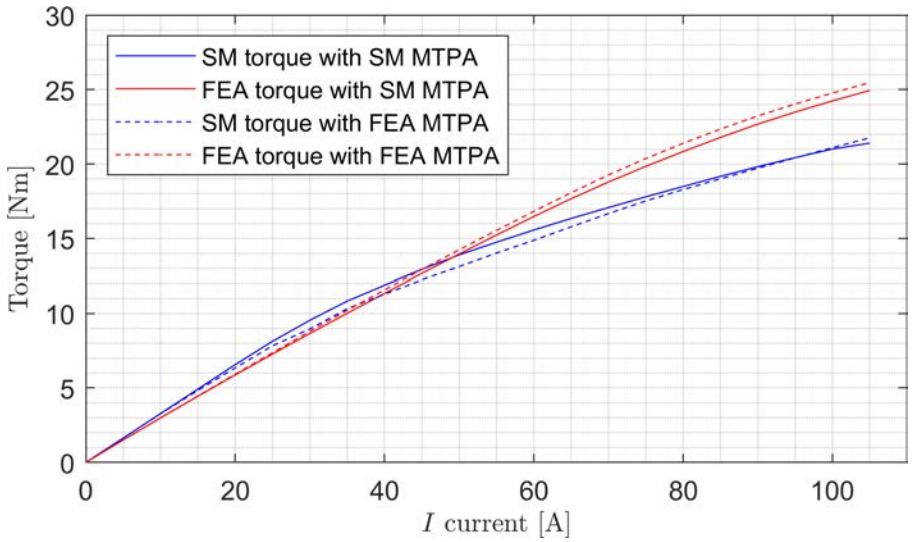

Figure 8.4: SM (blue) and FEA (red) torque with SM (continuous) and FEA (dashed) MTPA angle.

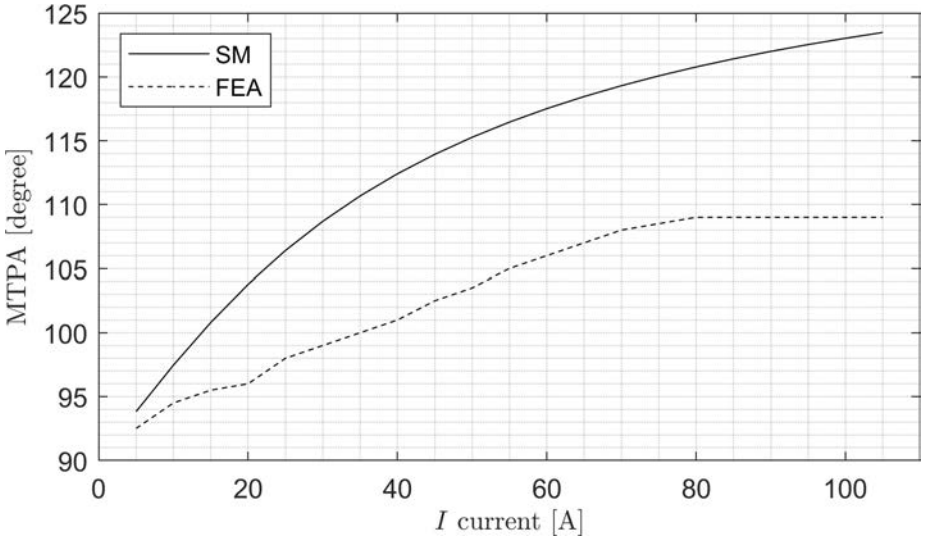

Figure 8.5: SM (continuous) and FEA (dashed) MTPA angle.

8.4 Thermal verification

In this section, a comparison of the temperature result is evaluated between the simplified thermal network of the section 5.7.1 (used in the SM) and the equivalent thermal FEA. The specific losses used for both methods are the ones of the SM. Indeed, if the FEA teeth and back-iron flux density values (like the ones in table 8.1) were used, the temperature results would be further different, and the analytical model would not be verified. Since the thermal FEA is computed with a 2D model of the motor, the comparison can not be done between the end-windings temperatures, so the maximum conductors temperature in the slot is evaluated.

The SM conductors temperature is calculated using (5.104) removing the last term in the sum:

$$\begin{aligned} T_c =& T_w + (R_{all} + R_{contact}) \cdot (P_{ew} + P_c + P_{febi} + P_{fet}) + \\ & (R_{fet}/3 + R_{febi}) \cdot (P_{ew} + P_c + P_{fet}) + R_c \cdot (P_{ew} + P_c) \\ =& 134.3°C \end{aligned} \tag{8.2}$$

The end-windings temperature is not much greater than the conductors temperature thanks to the short end-windings length and the good copper conductivity. As a matter of fact, (5.104) results $T_{ew} = 136.2°C$.

The FEA model (figure 8.6) has been set up as similar as possible to the analytical model of section 5.7.1, in particular:

- The used conductors and their insulator thickness are chosen from the table of [18].
- The joule losses, including the end-windings ones, are all dissipated through the slot, as it had been assumed in the SM.
- The teeth losses are distributed only on the rectangular part, since the SM

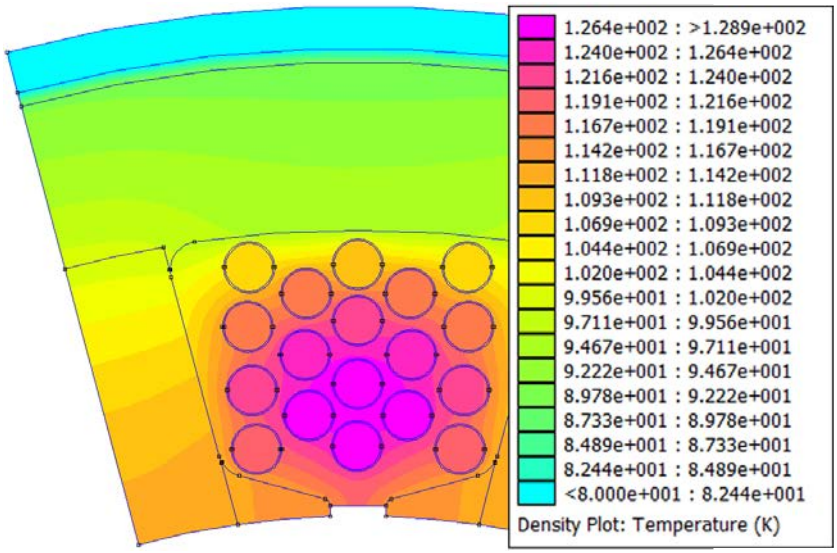

Figure 8.6: Thermal FEA of a single slot.

does not have the tooth tips.

- To avoid an excessive thickening of the mesh in the small contact gap between the lamination and the housing, the gap is drawn $0.5\,mm$ wide, and the thermal conductivity is accordingly scaled.
- The external surface of the housing is imposed at the constant temperature of $80°C$, as it had been assumed in the SM.

The joule losses have been calculated in (5.88). The copper resistivity multiplied by the square of the current density is already the specific joule losses. Thus, the specific joule losses, concentrating all the joule losses in the copper stack length, can be simply computed as

$$p_{s,J} = \rho_{Cu,165°C} J^2 \cdot \frac{L_{stk} + L_{ew}}{L_{stk}} = 8.58 \cdot 10^6\, W/m^3 \tag{8.3}$$

Similarly, the specific iron losses of the teeth and the back-iron can be derived by (5.90) as

$$\begin{aligned} p_{s,fet} &= 2 p_{fet} \gamma_{fe} = 2.55 \cdot 10^6\, W/m^3 \\ p_{s,febi} &= 1.5 p_{febi} \gamma_{fe} = 1.20 \cdot 10^6\, W/m^3 \end{aligned} \tag{8.4}$$

The thermal conductivity of the contact resistance between the housing and the laminations is scaled to the thickness $0.5\,mm$:

$$\lambda_{gap} = \lambda_{air} \frac{0.5\,mm}{0.01\,mm} = 1.3\,W/mK \tag{8.5}$$

Finally, the found solution is presented in figure 8.6. The maximum conductors temperature is $128.9°C$. The thermal analytical model is verified, except for a little difference. This little temperature difference could be generated by:

- The extra heat flow in the tooth tips, that are not present in the analytical model. Thus, the slot thermal resistance of the FEA is lower thanks to a higher exchange surface.
- The housing has a greater external diameter due to the increased thickness of the contact resistance. Thus, the heat exchange surface is slightly wider.

The maximum end-windings temperature is lower than the insulation class temperature ($165°C$), so the nominal current can be increased up to $43\,A$ with a $T_{ew} = 156.9°C$ without overcoming the thermal limit. Since the maximum end-windings temperature is not reached, it is evident that the restriction that has limited the shrinking of the optimized geometry is not the thermal limit but the maximum torque objective. As a matter of fact, a smaller motor does not present thermal infeasibility, but it does not reach the maximum torque objective.

Anyway, the found temperature margin allows to operate safely, because there are two considerations that have not been taken into account in the design:

- The torque as expected is not linear with the current, as shown in figure 8.4. Thus, the hypothesis of linearity made in section 3.2.1 to use the RMS value of torque, in reality, it slightly underestimates the RMS torque.
- Only the thermal steady-state is considered. In case of a sudden increase of torque demanding, the copper temperature increases above the steady-state temperature. Thus, the temperature margin guarantees to not overcome the insulation class temperature. For example, the maximum current has the following current density:

$$J_{max} = J \cdot \frac{35\,A}{105\,A} = 46.44\,A/mm^2 \tag{8.6}$$

that produces the following specifi joule losses:

$$p_{s,Jmax} = \rho_{Cu,165°C} J_{max}^2 = 56.984 \cdot 10^6\,W/m^3 \tag{8.7}$$

The adiabatic increase of copper temperature in 1 second of peak torque demanding is calculated as

$$\Delta T = \frac{p_{s,Jmax} \cdot 1\,s}{c_{s,Cu} \cdot \gamma_{Cu}} = 16.6°C \tag{8.8}$$

where $c_{s,Cu} = 385\,\frac{J}{KgK}$ is the specific heat of the copper. Thus, the temperature margin ensures that this peak torque can be maintained for about 2 seconds without overcoming the insulation class.

8.5 Torque ripple

The optimized geometry has been obtained without considering the torque fluctuations during the rotation. It is necessary to verify that the torque ripple is not too high. Unfortunately, a torque ripple limit is not defined because the

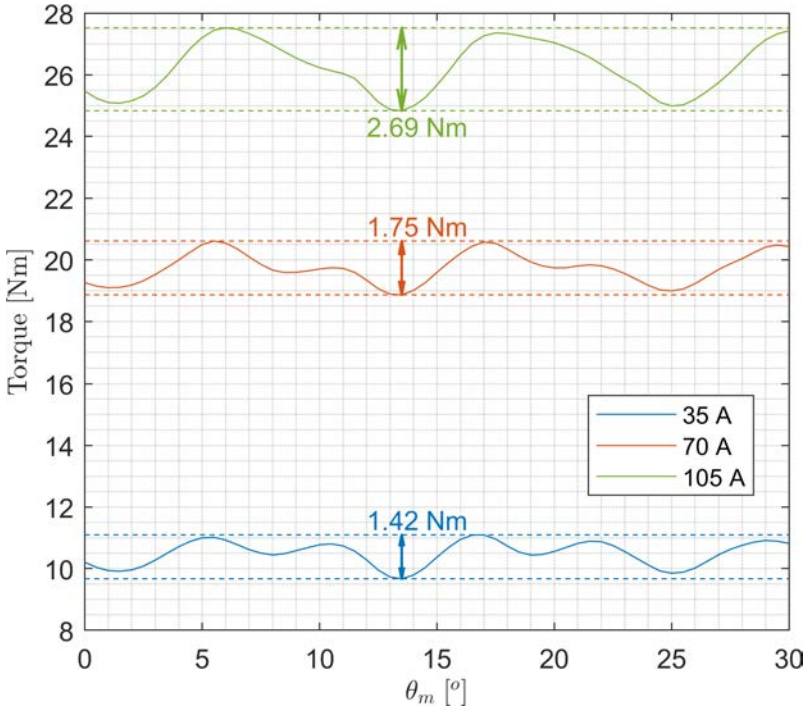

Figure 8.7: Torque ripple of the original geometry with different current levels.

custom application does not follow precise standards. Anyway, to remain under reliable torque ripple levels, the FreedomCAR standards are chosen. In particular, the "Freedom CAR 2020 Advanced Motor Performance requirements" [27] imposes that the peak-to-peak torque ripple must be lower than the 5% of the peak torque.

The torque ripple level is computed with a FEA, rotating the rotor from 0° to 30° with different current levels. The results are presented in figure 8.7. The peak-to-peak torque ripple is higher than the 5% of the peak torque for every current level. To satisfy the FreedomCAR standard, it should be at least lower than $1.3\,Nm$.

To reduce the torque ripple, the technique of round shaping the pole island is chosen. The technique allows to achieve a different air gap flux density distribution, in order to obtain a different EMF (Electro-Magnetic Force) shape and especially a reduction of torque ripple [28]. The rotor shaping is often obtained with an increase of the air gap width. In particular, the maximum increase Δr is reached on the q-axis, as shown in figure 8.8. On the other hand, this technique increases the air gap losses because the not round rotor has a greater friction with the air. Moreover, it reduces the q-axis inductance, hence the torque. The three evaluated geometries, shown in figure 8.8, are:

(a) **Full arch**: the entire pole is round shaped with an arch.

(b) **Wide pole arch**: the arch covers up to the end of the ribs.

(c) **Pole arch**: the arch covers only the magnet island.

The torque ripples of the three geometries, computed with $\Delta r = 0.70\,mm$, $35\,A$ and $105\,A$, are presented in figure 8.9. The peak-to-peak torque ripples and

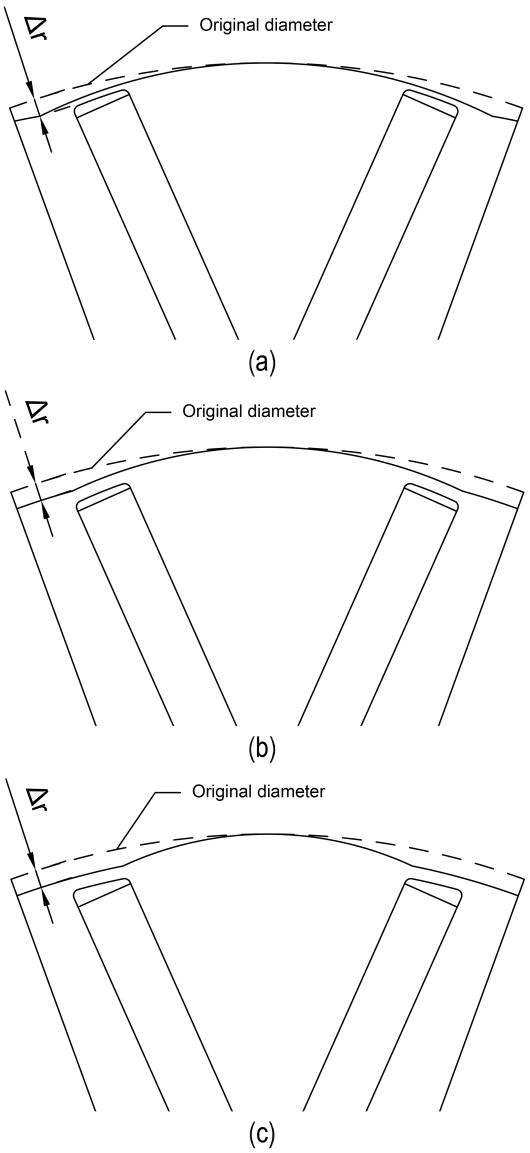

Figure 8.8: Round shape designs: (a) full arch, (b) wide pole arch, (c) pole arch.

the mean torque values are reported in table 8.3. All three geometries present a torque ripple reduction compared to the original rotor. The increase of air gap width is accompanied with a reduction of torque, except for the full arch geometry. Its increase is due to the magnet flux that is less short-circuited by the higher q-axis air gap reluctance. The pole arch geometries have a lower torque ripple than the full arch. On the other hand, the mean torque is lower, but, since the torque objectives are nevertheless satisfied, the reduction is negligible. Finally, the wide pole arch geometry is chosen because presents the same torque ripple reduction of the pole arch but with a higher mean torque.

Then, the comparison of different values of Δr is performed. The torque fluctuations are presented in figure 8.10. The peak-to-peak torque ripples, their percentage reduction and the mean torque values are reported in table 8.4. It results evident that the $\Delta r = 0.70\,mm$ is the value that has the best compromise

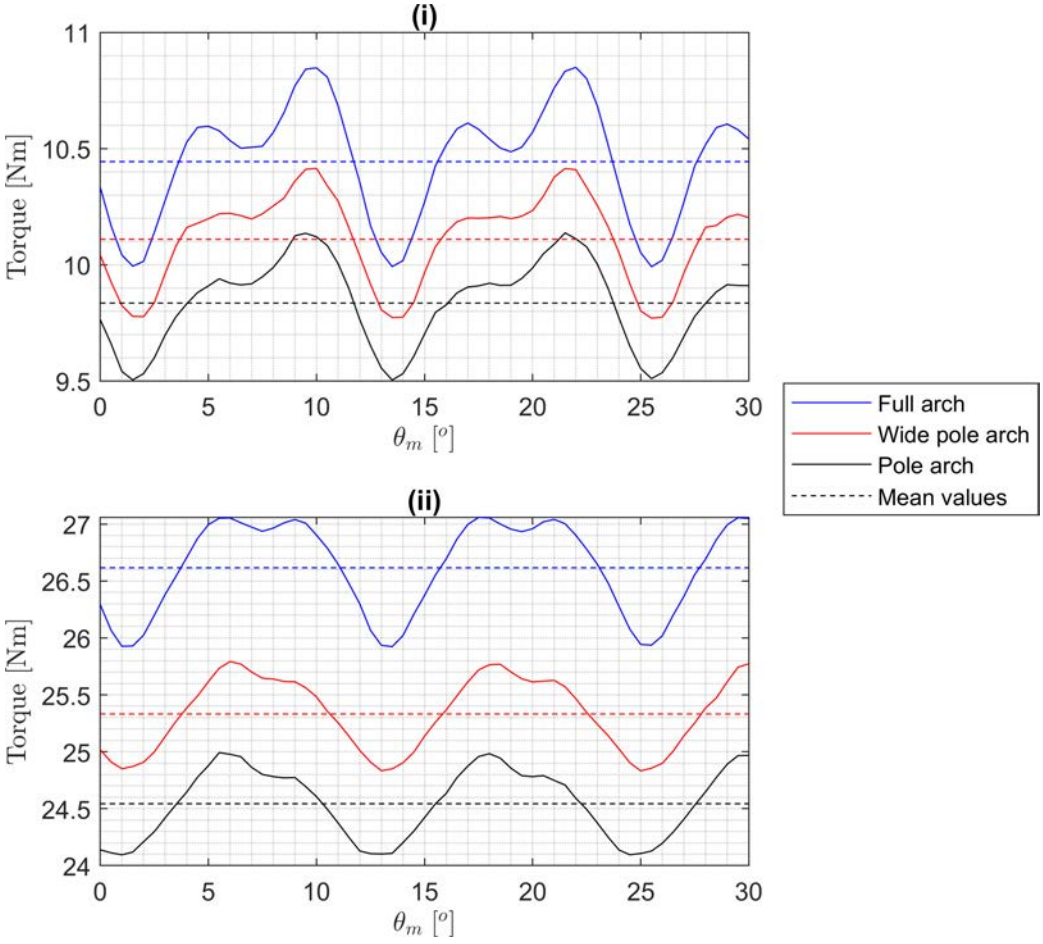

Figure 8.9: Torque ripple of the three geometries with: (i) $I = 35\,A$, (ii) $I = 105\,A$

Current	**Geometry**	**Torque ripple** $[Nm]$	**Mean torque** $[Nm]$
$I = 35\,A$	Original	1.42	10.49
	Full arch	0.86	10.44
	Wide pole arch	0.64	10.11
	Pole arch	0.63	9.84
$I = 105\,A$	Original	2.69	26.23
	Full arch	1.14	26.62
	Wide pole arch	0.96	25.33
	Pole arch	0.90	24.54

Table 8.3: Peak-to-peak torque ripple and mean torque of the original motor and of three geometries with $I = 35\,A$ and $I = 105\,A$.

of torque ripple and mean torque reduction. As a matter of fact, the data highlight that the torque ripple is reduced linearly for every considered step of Δr. Instead, the mean torque reduces faster for values higher than $0.70\,mm$. Moreover, the torque ripple limit of the FreedomCAR requirements has been widely satisfied. If it were necessary to reduce further the torque ripple, slot skewing can be used [28].

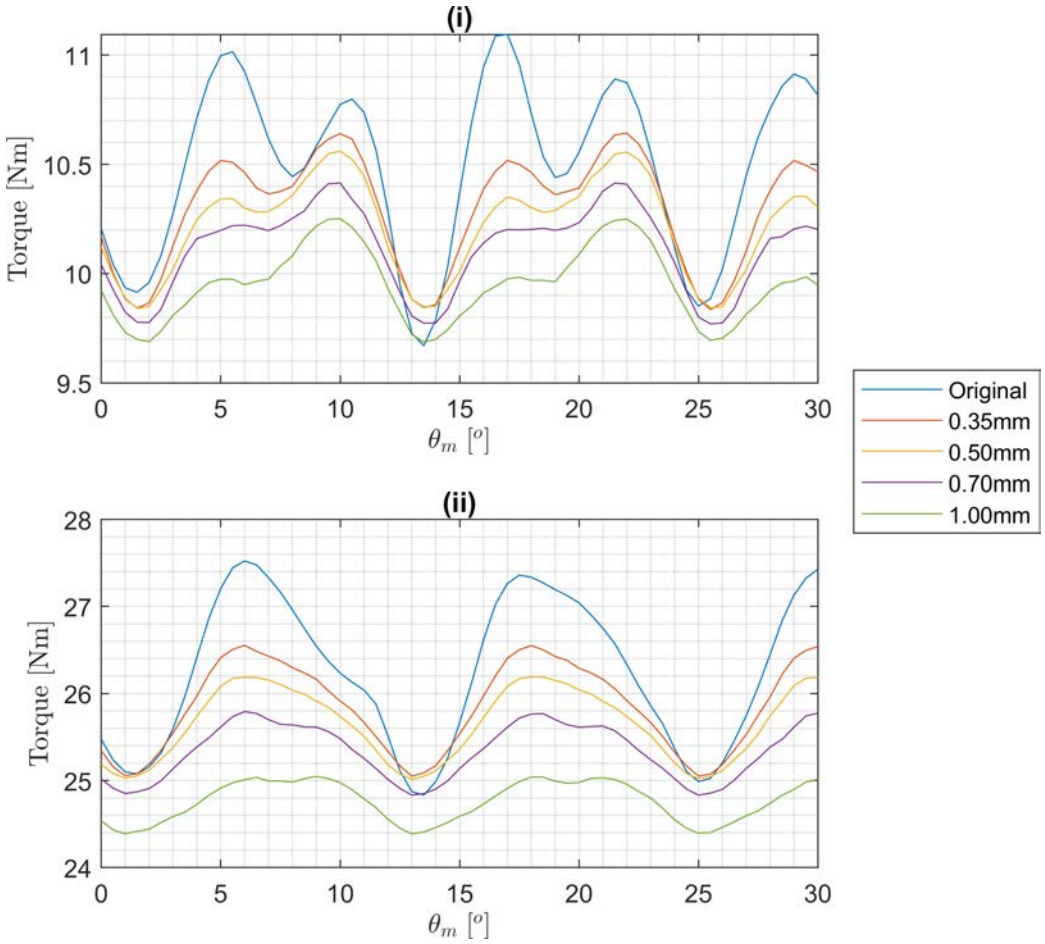

Figure 8.10: Torque ripple of different Δr with: (i) $I = 35\,A$, (ii) $I = 105\,A$

Current	**Δr**	**Torque ripple**		**Mean torque**	
	mm	Nm	%	Nm	%
$I = 35\,A$	Original	1.42	0	10.49	0
	0.35	0.81	-43	10.29	-1.9
	0.50	0.72	-49	10.21	-2.6
	0.70	0.64	-55	10.11	-3.6
	1.00	0.56	-60	9.95	-5.1
$I = 105\,A$	Original	2.69	0	26.23	0
	0.35	1.50	-44	25.84	-1.5
	0.50	1.18	-56	25.64	-2.3
	0.70	0.96	-64	25.33	-3.4
	1.00	0.66	-75	24.76	-5.6

Table 8.4: Peak-to-peak torque ripple and mean torque of the original motor and of different Δr with $I = 35\,A$ and $I = 105\,A$.

8.5.1 Cogging torque

The cogging torque is evaluated to verify that the assumptions made in section 6.1.3 are true. The FEA of both the original rotor geometry and the new one are performed with zero current rotating the rotor from 0° to 30°. The torque, calculated with the Maxwell stress tensor, is shown in figure 8.11 as a function of the rotor angle θ_m. The torque curve has a periodicity of 5 times in 30°. So, in 360° the torque curve repeats 60 times, as expected by the value of the $LCM\{Q, 2p\}$. The results highlight that the round shaping of the pole island also produced a beneficial cogging torque reduction.

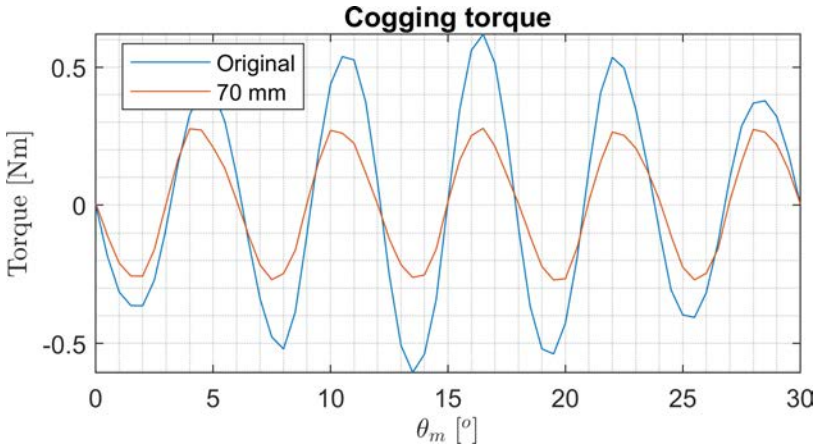

Figure 8.11: Cogging torque of the original geometry and the $\Delta r = 0.70\,mm$ wide pole arch geometry.

8.6 Demagnetization check

To ensure that the magnets do not demagnetize in any operating condition, a FEA is computed imposing the maximum current with $\alpha_{ie} = 180°$. This condition is the most unsafe one, because the current produces a d-axis flux in the opposite direction of the magnets. The result, shown in figure 8.12, highlights some small critical points in the magnet that have a low flux density. According to the coercivities calculated in (6.11), the magnet demagnetizes if negative flux densities are reached. Instead, the minimum flux densities are about $0.1\,T$ with some local minima of $0.05\,T$. Thus, even with the maximum current, there is no demagnetization of the magnets. Anyway, these values could produce demagnetization helped by the magnet ageing or manufacturing imperfections.

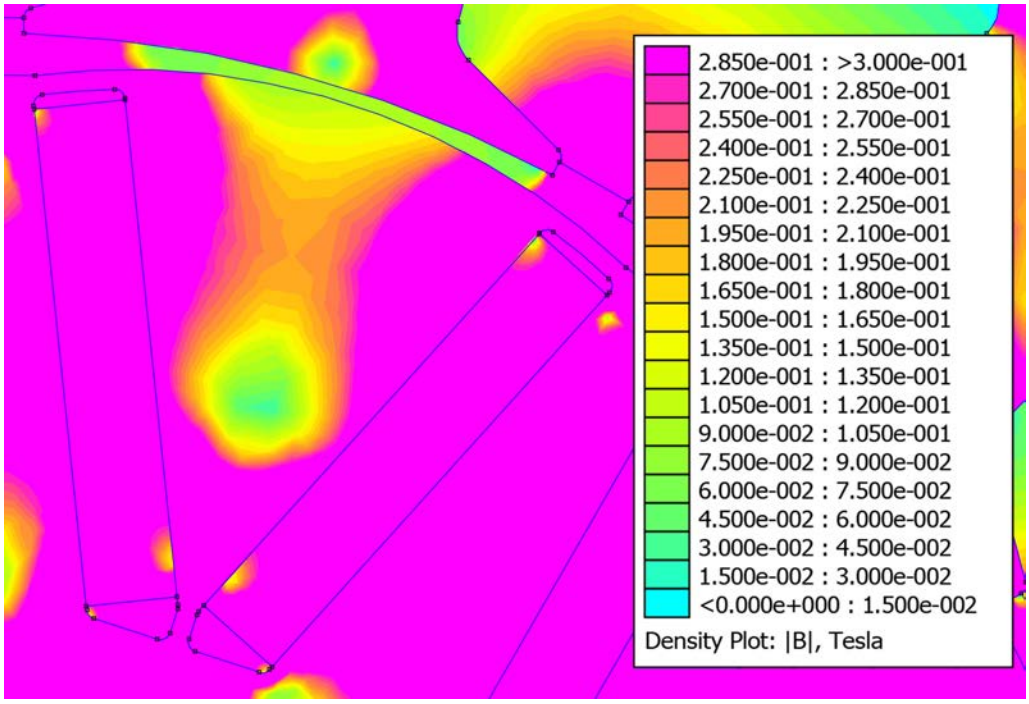

Figure 8.12: Magnet detail of the FEA result with $I = 105\,A$ and $\alpha_{ie} = 180°$.

8.7 Flux density THD

In this section, the distortion of the air gap flux density is calculated to evaluate the impact of the choice of the 12/10 winding, which was the one with the higher MMF THD in table 6.5. Unfortunately, not having the optimized motors with the other windings, a direct comparison is not possible. Anyway, the THD value of the total flux density can be evaluated and compared to the THD of the winding and the magnets.

The air gap flux density and its p harmonic, produced with $\alpha_{ie} = 110°$ and the nominal and maximum currents, are presented in figure 8.13. As expected, the higher current produces a higher distortion. The round shaping of the pole island improved the shape of the flux density compared to the not shaped rotor solution of figure 8.2. The improvement is confirmed by the THD values reported in table 8.5, that have been calculated as

$$THD\,\% = 100 \cdot \sqrt{\sum_{k \neq p}^{\infty} \left(\frac{B_k}{B_p}\right)^2} \tag{8.9}$$

where B_k is the RMS value of the generic k harmonic of the air gap flux density B, and B_p is the RMS value of the specific p harmonic. The RMS value B_k has

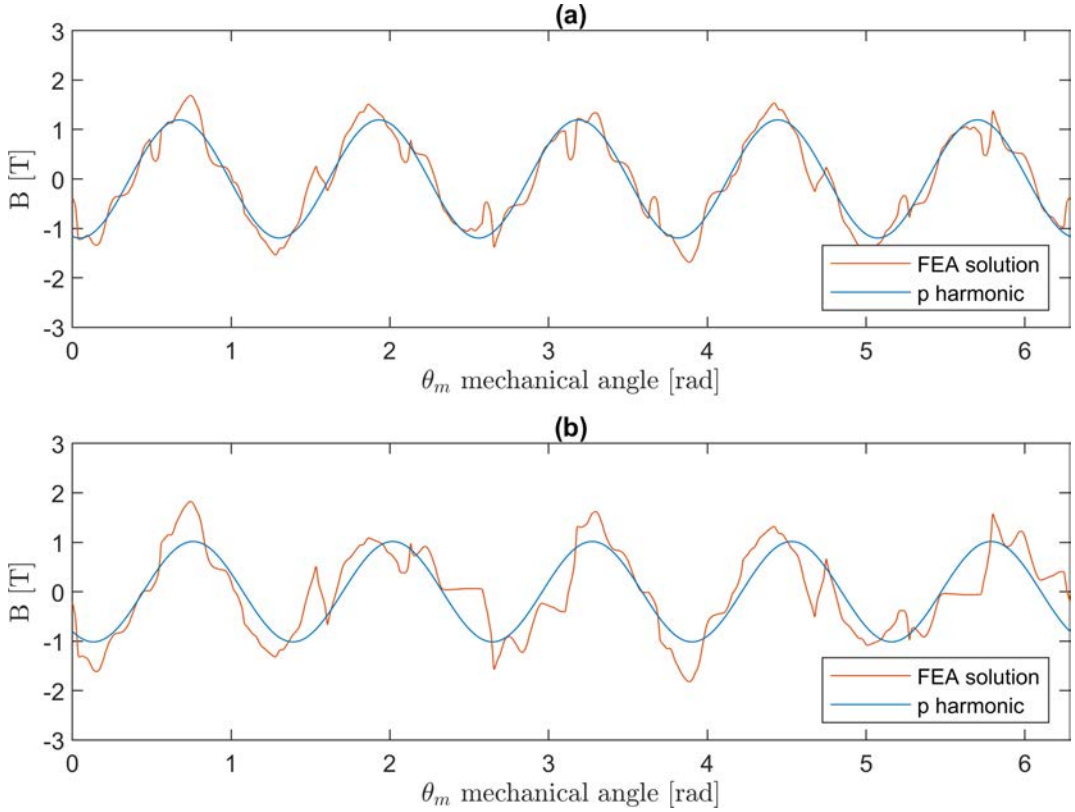

Figure 8.13: FEA solution of the total air gap flux density and the respective p harmonic with: (a) $I = 35\,A$ and $\alpha_{ie} = 110°$ and (b) $I = 105\,A$ and $\alpha_{ie} = 110°$.

	THD of B [%]	
	$I = 35\,A$	$I = 105\,A$
Original rotor	43.74	66.57
Wide pole arch	31.43	65.52

Table 8.5: Comparison of the flux density THD between the original geometry and the new wide pole arch geometry, with $\alpha_{ie} = 110°$, $I = 35\,A$ and $I = 105\,A$.

been calculated as

$$\begin{aligned} B_k &= \sqrt{\frac{\hat{B}_{d,k}^2 + \hat{B}_{q,k}^2}{2}} \\ \hat{B}_{d,k} &= \frac{1}{\pi}\int_0^{2\pi} B\cos(k\theta_m) \\ \hat{B}_{q,k} &= \frac{1}{\pi}\int_0^{2\pi} B\sin(k\theta_m) \end{aligned} \tag{8.10}$$

The 12/10 winding THD, as reported in table 6.5, was 97.99%, while the magnet THD, considering a modified square wave of width $c_m = 0.605$, is 35.66%. These values highlight that the impact of the winding distortion is weak, regarding the nominal current results obtained in table 8.5. Thus, the choice to use a winding with a high THD but with other advantages, is verified. In this evaluation

between the magnet and winding THD, the distortion of the local saturations and of the slot-openings is not taken into account. These factors could improve or worsen the flux density shape, but their evaluation is difficult.

To minimize the magnet THD to 28.91%, the magnet coverage c_m should be increased to 0.7422. Another choice might be to cancel out the third harmonic, with a $c_m = 0.6667$ [28]. The choice of a different magnet coverage must also evaluate the reduction of the q-axis iron, which therefore saturates more easily, and the change of the fundamental amplitude of magnet flux density.

8.8 Motor map

To save computational time, the motor is only mapped close to the expected MTPA trajectory, that should be between 90° and 110° according to figure 8.5. Thus, a FEA is performed increasing the current level from $0\,A$ to $105\,A$, and rotating the α_{ie} angle. The results are matrices $\boldsymbol{M\{\alpha_{ie}, I\}}$, in which each element has been calculated with a certain current level and current angle. The MTPA trajectory can be identified searching the maximum torque value for every current level. The torque map and the MTPA trajectory are presented in figure 8.14. The figure shows that as the current grows, the motor saliency has a greater contribution to the total torque, so the MTPA angle increases. As expected, the increasing distance of the iso-torque curves highlights that the torque does not grow linearly with the current.

From the same analysis, it is also possible to map the inductances L_d, L_q and the saliency ratio ξ. The permanent magnet flux linkage depends on the q-axis current due to the cross saturation (as shown later in section 8.8.1). Thus, the permanent magnet flux linkage is equal to the values of the d-axis flux with $\alpha_{ie} = 90°$ (the d-axis current is zero and the motor is fed only with the q-axis current):

$$\boldsymbol{\Lambda_{PM}\{90°, I\} \equiv \Lambda_d\{90°, I\}} \tag{8.11}$$

where $\boldsymbol{\Lambda_d}$ is the matrix of the d-axis flux linkage, and $\boldsymbol{I}$ is the array of the current level. The d-axis and q-axis inductance matrices are calculated as

$$\begin{aligned} \boldsymbol{L_d\{\alpha_{ie}, I\}} &= \frac{\boldsymbol{\Lambda_d\{\alpha_{ie}, I\} - \Lambda_{PM}\{90°, I\}}}{\boldsymbol{I_d\{\alpha_{ie}, I\}}} \\ \boldsymbol{L_q\{\alpha_{ie}, I\}} &= \frac{\boldsymbol{\Lambda_q\{\alpha_{ie}, I\}}}{\boldsymbol{I_q\{\alpha_{ie}, I\}}} \end{aligned} \tag{8.12}$$

where $\boldsymbol{\alpha_{ie}}$ is the array of the current angle, $\boldsymbol{I_d}$ and $\boldsymbol{I_q}$ are the matrices of the d/q-axis currents, and $\boldsymbol{\Lambda_q}$ is the matrix of the q-axis flux linkage. The inductance maps are presented in figure 8.15. The q-axis inductance is higher than the d-axis one in any current region, thanks to the lower path reluctance. Increasing the q-axis current, the L_q decreases due to the saturation of the q-axis iron path. Indeed, the greater the reluctance the lower the associated inductance. Instead, for the d-axis it is observed the opposite, because the d-axis current produces a counter flux of the PM flux, so the saturation of the d-axis path is reduced as the

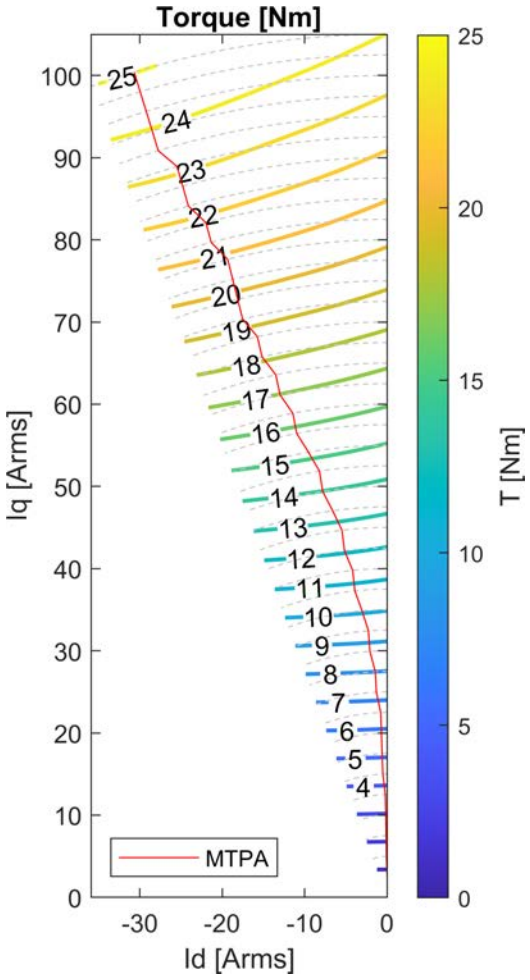

Figure 8.14: Torque map between 90° and 110°, 0 A and 105 A, and MTPA trajectory (red line).

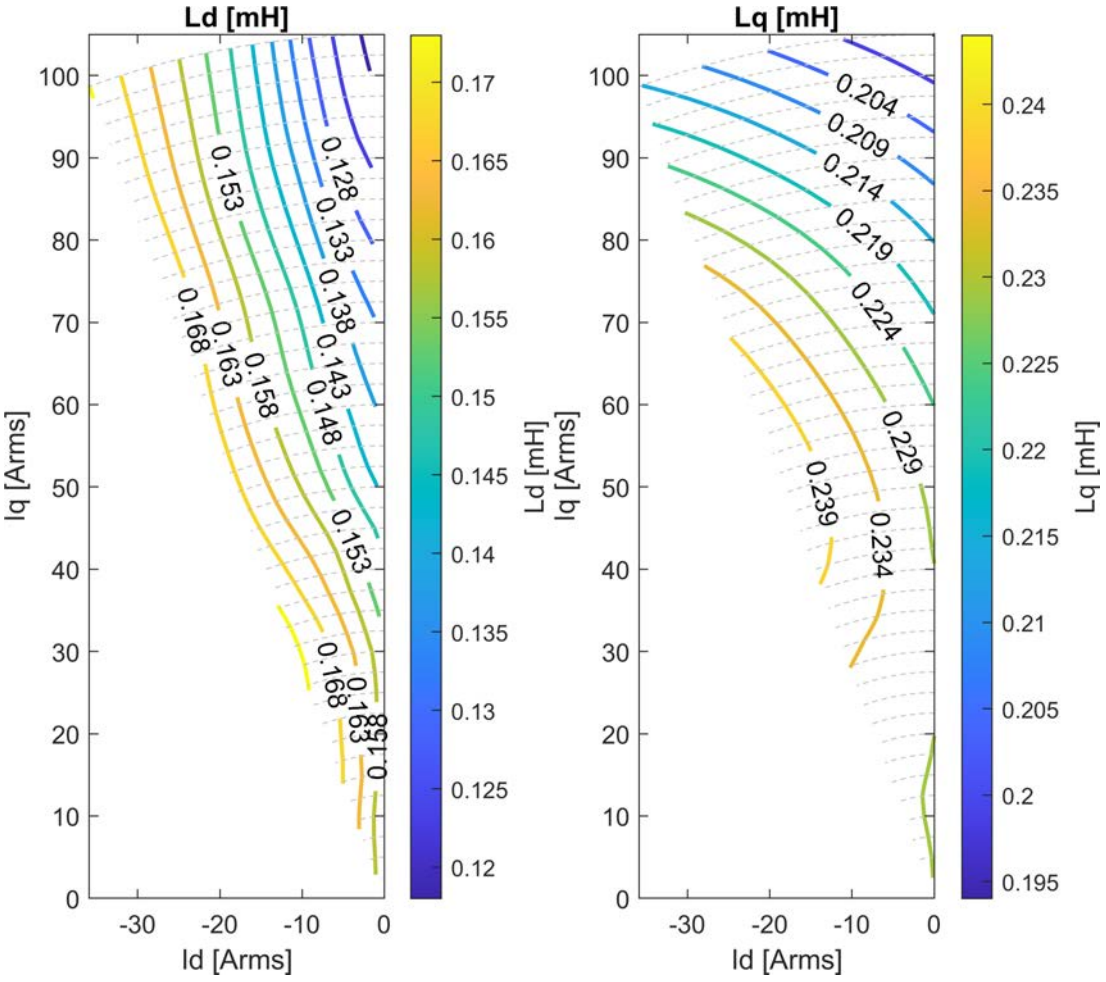

Figure 8.15: Inductance map between 90° and 110°, 0 A and 105 A.

current grows.

Then, the saliency ratio can be calculated as

$$\boldsymbol{\xi\{\alpha_{ie}, I\}} = \frac{\boldsymbol{L_q\{\alpha_{ie}, I\}}}{\boldsymbol{L_d\{\alpha_{ie}, I\}}} \tag{8.13}$$

The saliency ratio map is presented in figure 8.16. The map shows that in the MTPA trajectory the saliency ratio is almost constant and equal to $\xi \simeq 1.5$ up to 70 A, where it starts to decrease down to $\xi \simeq 1.3$.

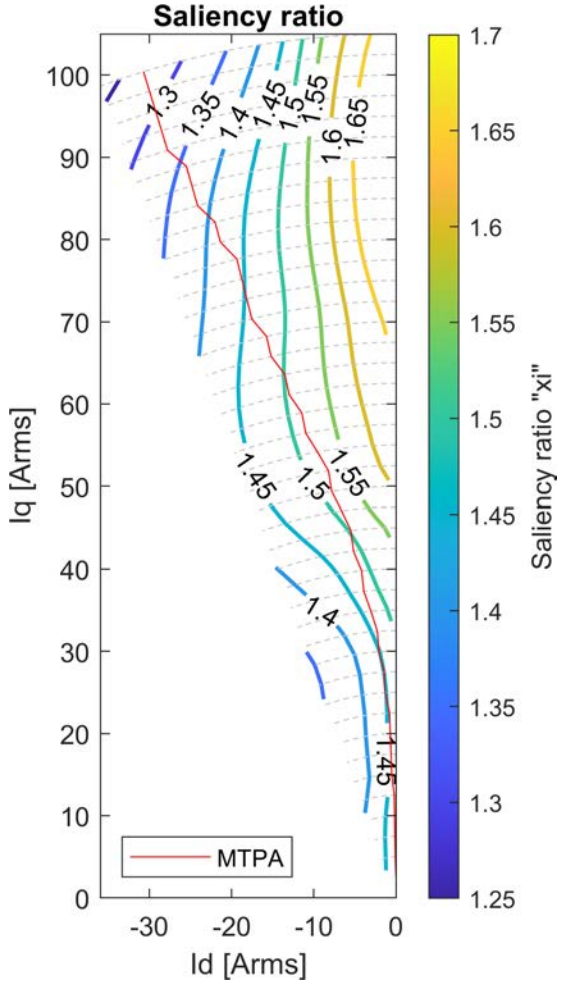

Figure 8.16: Saliency ratio map between 90° and 110°, 0 A and 105 A, and MTPA trajectory (red line).

8.8.1 Inductances

A further analysis is performed to calculate the inductances along the d/q-axis, so the cross saturation is neglected. The FEA is performed maintaining the current angle to $\alpha_{ie} = 180°$ for the d-axis or to $\alpha_{ie} = 90°$ for the q-axis, and increasing progressively the current level. The inductances are calculated with (8.12), except for the PM flux linkage that is always equal to the value with $I_q = 0$. The flux linkage and the inductances are presented in figure 8.17. The only result with cross saturation is the PM flux linkage used in (8.11), which decreases with greater q-axis current. It is evident the same phenomena of reduction of the inductance with greater saturation, which was described before. The dashed line of the d-axis indicates the current region not used in the MTPA operation. Considering the not-dashed line, there is a second confirmation that $L_q > L_d$.

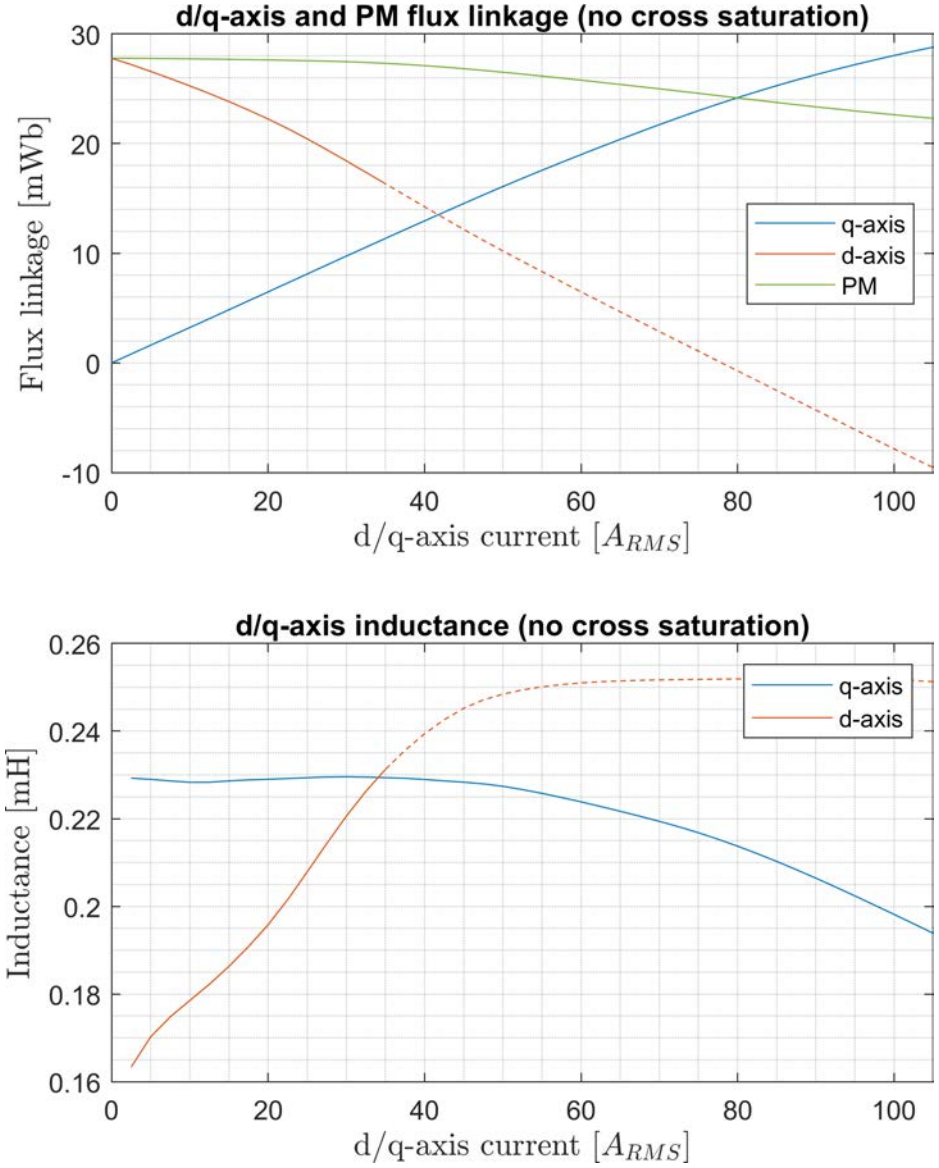

Figure 8.17: Flux linkages and inductances without cross saturation, except for the PM flux linkage. The dashed line is the current region not used in the MTPA operation.

8.8.2 Speed and field weakening

The values of flux linkages computed in the MTPA trajectory can be used to calculate the maximum speed with the maximum available voltage U, which was estimated in (2.3). The maximum speed in rpm is expressed as

$$\boldsymbol{n\{\alpha_{ie}, I\}} = \frac{60}{2\pi p} \cdot \frac{U}{\sqrt{\boldsymbol{\Lambda_q\{\alpha_{ie}, I\}}^2 + \boldsymbol{\Lambda_d\{\alpha_{ie}, I\}}^2}} \tag{8.14}$$

The maximum speed of the MTPA torque is presented in figure 8.18. When the speed 16.3 $krpm$ is exceeded, it is not possible to maintain the maximum current level. The current level is reduced along the MTPA trajectory to achieve greater speeds up to 19.7 $krpm$, where the torque is zero. The objective of maximum speed 20 $krpm$ is not achieved. Thus, it is necessary to operate in flux weakening to increase the speed. The flux weakening (FW) is performed by maintaining the current level to 105 A, while the current angle is progressively increased to reduce both the d-axis and q-axis flux linkages. The FW operation allows to reach the speed objective with 22 Nm, as shown by the dashed line in figure 8.18.

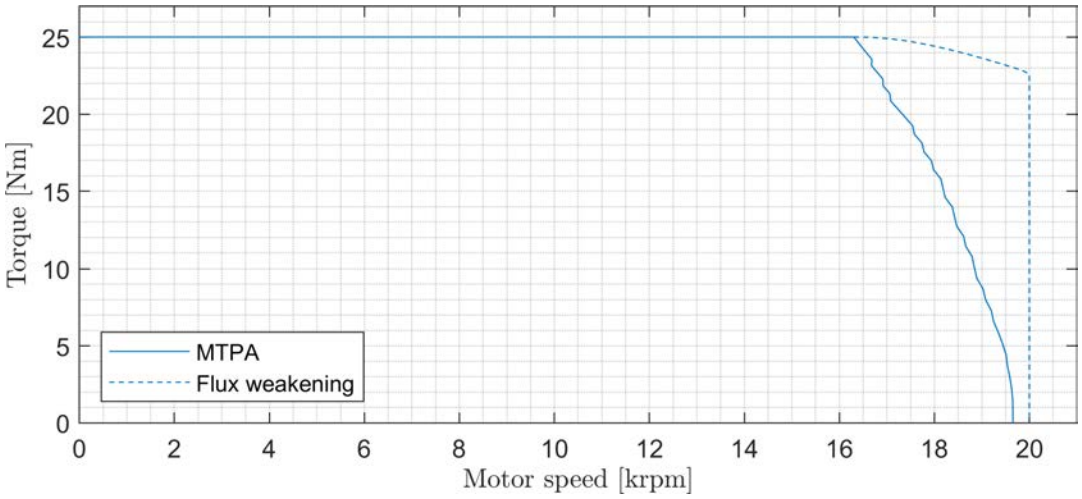

Figure 8.18: Torque as a function of speed in MTPA and FW operation.

If the ball bearings are sized properly, the flux weakening allows to overcome the 20 $krpm$ speed. These speeds could be useful only during the acceleration event. As a matter of fact, in figure 3.2 and 3.3 was shown that the drive cycle of other events does not require these speeds. The full range speed of the flux weakening operation is shown in figure 8.19. An hypothetical speed of 57 $krpm$ is reachable.

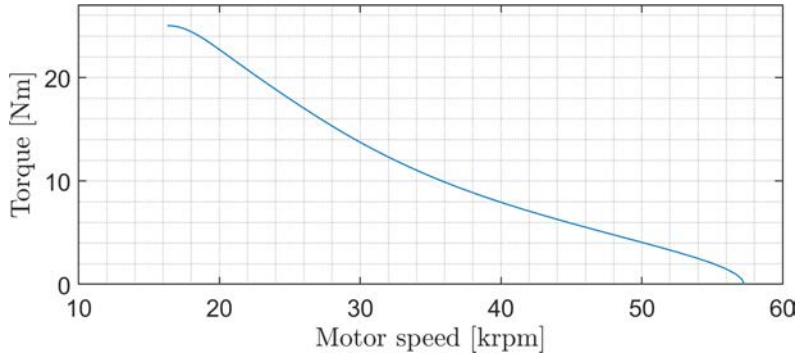

Figure 8.19: Torque as a function of speed in FW operation.

8.9 Performance comparison

In this section, the characteristics of the new design are compared to the AMK motor. First, in figure 8.20, the torque and speed curve of the new design (presented before in figure 8.18) is compared to the AMK motor characteristic, extrapolated from the datasheet. The MTPA curves show that the AMK motor can reach higher speeds without flux weakening. This could be the result of a lower PM flux linkage, which results in a lower maximum torque. Anyway, the FW operation allows the new design to achieve much greater performance.

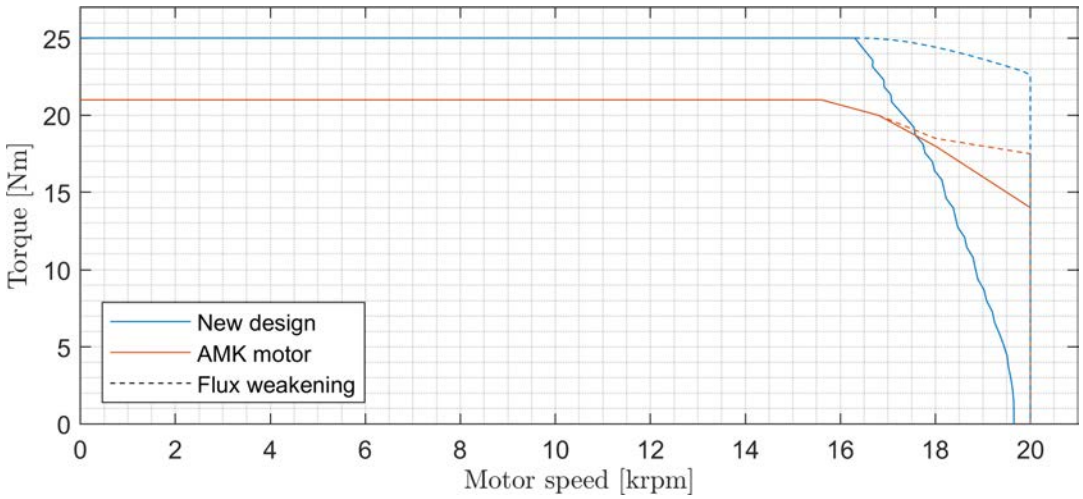

Figure 8.20: Torque and speed curve of the AMK motor and the new design.

Finally, the main characteristics of both motors are summarized in table 8.6. The new design has achieved better values in every characteristic, except for the moment of inertia. Anyway, the results of section 3.3 showed that moments of inertia lower than $7\,kgcm^2$ do not offer better car performance. In the case that a lower torque is necessary, the motor stack length can be reduced to reduce both the weight and the moment of inertia.

Characteristic	**AMK motor**	**New design**
Nominal torque	9.8 Nm	10.1 Nm
Nominal speed	12000 rpm	15000 rpm
Nominal power	12.3 kW	16.2 kW
Nominal efficiency	87.34 %	$\sim$ 96.77 %
Nominal current	41 A	35.8 A
Maximum torque	21 Nm	25.3 Nm
Maximum speed	20000 rpm	20000 rpm
Poles number "$2p$"	10	10
Saliency ratio "ξ"	2	1.45
q-axis inductance "L_q"	0.24 mH	0.232 mH
d-axis inductance "L_d"	0.12 mH	0.158 mH
Insulation class	F	H
Weight	3.55 kg	$\sim$ 3 kg
Moment of inertia	2.74 $kgcm^2$	5.31 $kgcm^2$

Table 8.6: Main characteristics of the AMK motor and the new design.

Chapter 9

Conclusions

This work dealt with the design and the optimization of a permanent magnet motor for the Formula SAE race car. The analytical models of the slotless and the slotted motor have been presented, and they were used to optimize the objectives of torque, weight and losses. The optimization has been computed to compare the slots/poles combination, finding that the best one is the 12/10. It has been used also to compare the slotted to the slotless motor, highlighting that the latter has a too high moment of inertia. Lastly, the optimization has been computed to obtain the geometry that satisfied the torque objectives, minimizing the weight and the losses.

The torque objectives were extrapolated from the drive cycle of another Formula SAE car and a lap time simulation. The lack of the actual drive cycles of the specific motor of the electric car has required to approximate the analysis. Consequently, the maximum torque objective was not clearly defined. Since the motor size depends mainly by the maximum torque, the overestimate of the objective may have produced a geometry with a heavier weight than necessary. The use of the RMS torque to define the motor nominal torque is not completely reliable, because the torque is not proportional to the losses. A more correct verification could be the simulation of the motor during the entire drive cycle.

The use of the analytical model, instead of the finite element analysis (FEA), has drastically reduced the computational time. As a matter of fact, the slottel model requires about three seconds to complete the calculations. Although it is a short time, the script has not been optimized at its best, indeed it uses some functioning but slow operations. Improving the code, the calculations could be completed in a tenth of the time. Moreover, the method of discarding the not feasible motors lengthens the optimization time.

The slotted model presents some problems, which have been already highlighted in chapter 8:

- The wrong computation of the flux density causes an error in the calculation of the torque and the iron flux densities, which results in an overestimate of the iron losses. To improve the solving method, the magnetic network should be extended to the iron reluctances of both the stator and the rotor, which should be able to saturate. In this way, a better solution is obtained, although the local saturation of the FEA would still cause a small difference.

- The calculation of the torque presents an error due to the wrong flux density and the wrong MTPA angle. The latter does not produce a big error, and it can be neglected. Anyway, the estimate of the torque is reliable, but to have a more precise value the model must be improved.
- The thermal verification is very reliable with the hypotheses made. On the other hand, the rotor losses have been neglected and could change the result. A check should be made.
- The model does not calculate the torque ripple, which therefore must be reduced only subsequently. In the case study, the pole shaping was necessary. For example, the use of a different magnet coverage c_m, in the beginning of the optimization, could reduce the torque ripple, so a less invasive subsequent intervention can be done.

The goal of the thesis was largely achieved, because all the motor characteristics have been improved. In the case a lower torque is needed, the motor stack length can be reduced to obtain a lighter geometry. The project is not ready to be built, because the mechanical simulation is necessary to verify the thickness of the ribs. Moreover, if the chosen materials are not available and are exchanged for similar ones, the design may need to be adapted. If the torque ripple is still too high, it may be necessary to change the slots/poles combination. In that case, the promising combination is the 18/8 because it has a lower cogging torque and it has only one coil overlapping.

Bibliography

[1] "Formula Student Germany Concept", https://www.formulastudent.de/about/concept/

[2] "Formula SAE Italy", https://www.formula-ata.it/formula-sae-italy/

[3] "Formula SAE", https://www.fsaeonline.com/

[4] "Race UP our history", https://www.raceup.it/en/team/history.html

[5] "Race UP: SG-e 03", https://raceup.it/en/cars/ed.html

[6] E. Carraro, M. Morandin and N. Bianchi, "Traction PMASR Motor Optimization According to a Given Driving Cycle" in *IEEE Transactions on Industry Applications*, vol. 52, no. 1, pp. 209-216, Jan.-Feb. 2016, doi: 10.1109/TIA.2015.2477479.

[7] D. A. Doyle, G. Cunningham, G. White and J. Early, "Lap Time Simulation Tool for the Development of an Electric Formula Student Car" in *SAE Technical Paper* 2019-01-0163, 2019, doi:10.4271/2019-01-0163.

[8] "Formula Student Germany Results", https://www.formulastudent.de/fsg/results/2019/

[9] S. G. Min and B. Sarlioglu, "Advantages and Characteristic Analysis of Slotless Rotary PM Machines in Comparison With Conventional Laminated Design Using Statistical Technique," in *IEEE Transactions on Transportation Electrification*, vol. 4, no. 2, pp. 517-524, June 2018, doi: 10.1109/TTE.2018.2810230.

[10] A. Tessarolo and M. Bortolozzi, "A sizing equation for slotless surface-mounted radially-magnetized permanent-magnet machines," *2016 XXII International Conference on Electrical Machines (ICEM)*, Lausanne, 2016, pp. 1264-1269, doi: 10.1109/ICELMACH.2016.7732687.

[11] A. Tessarolo, L. Branz and C. Bruzzese, "A compact analytical expression for the load torque in Surface Permanent-Magnet machines with slotless stator design," *2013 IEEE Workshop on Electrical Machines Design, Control and Diagnosis (WEMDCD)*, Paris, 2013, pp. 8-17, doi: 10.1109/WEMDCD.2013.6525160.

[12] N. Bianchi, "Analysis of the IPM motor - part I, analytical approach, in design, analysis, and control of interior PM synchronous machines" in *IEEE IAS Tutorial Course Notes*, IAS Annu. Meeting, CLEUP, N. Bianchi and T.M. Jahns, Eds.,Seattle, WA, Oct.3,2004 pp. 3.1-3.33

[13] N. Bianchi, S. Bolognani and F. Luise, "Analysis and design of a PM Brushless Motor for high-speed operations," in *IEEE Transactions on Energy Conversion*, vol. 20, no. 3, pp. 629-637, Sept. 2005, doi: 10.1109/TEC.2005.847991.

[14] G. Bacco, N. Bianchi and H. Mahmoud, "A Nonlinear Analytical Model for the Rapid Prediction of the Torque of Synchronous Reluctance Machines," in *IEEE Transactions on Energy Conversion*, vol. 33, no. 3, pp. 1539-1546, Sept. 2018, doi: 10.1109/TEC.2018.2808168.

[15] N. Bianchi, S. Bolognani and P. Frare, "Design criteria for high-efficiency SPM synchronous motors," in *IEEE Transactions on Energy Conversion*, vol. 21, no. 2, pp. 396-404, June 2006, doi:10.1109/TEC.2005.853720.

[16] Z. Huang, J. Fang, X. Liu and B. Han, "Loss Calculation and Thermal Analysis of Rotors Supported by Active Magnetic Bearings for High-Speed Permanent-Magnet Electrical Machines," in *IEEE Transactions on Industrial Electronics*, vol. 63, no. 4, pp. 2027-2035, April 2016, doi: 10.1109/TIE.2015.2500188.

[17] Modello SKF per il calcolo del momento di attrito: pdf link

[18] Bianchi N., Bolognani S., "Metodologie di Progettazione delle Macchine Elettriche", CLEUP, pp. 48, 52, 245, 267-268, 353-354, 2001, ISBN:88-7178-529-0

[19] D. Staton, A. Boglietti and A. Cavagnino, "Solving the more difficult aspects of electric motor thermal analysis in small and medium size industrial induction motors," in *IEEE Transactions on Energy Conversion*, vol. 20, no. 3, pp. 620-628, Sept. 2005, doi: 10.1109/TEC.2005.847979.

[20] W. Wang, Y. Zhou and Y. Chen, "Investigation of lumped-parameter thermal model and thermal parameters test for IPMSM," *2014 17th International Conference on Electrical Machines and Systems (ICEMS), Hangzhou, 2014, pp. 3246-3252, doi: 10.1109/ICEMS.*2014.7014052.

[21] A. M. EL-Refaie and T. M. Jahns, "Optimal flux weakening in surface PM machines using fractional-slot concentrated windings," in *IEEE Transactions on Industry Applications*, vol. 41, no. 3, pp. 790-800, May-June 2005, doi: 10.1109/TIA.2005.847312.

[22] F. Magnussen and C. Sadarangani, "Winding factors and Joule losses of permanent magnet machines with concentrated windings," *IEEE International*

Electric Machines and Drives Conference, 2003. IEMDC'03., Madison, WI, USA, 2003, pp. 333-339 vol.1, doi: 10.1109/IEMDC.2003.1211284.

[23] E. Carraro, N. Bianchi, S. Zhang and M. Koch, "Design and Performance Comparison of Fractional Slot Concentrated Winding Spoke Type Synchronous Motors With Different Slot-Pole Combinations," in *IEEE Transactions on Industry Applications*, vol. 54, no. 3, pp. 2276-2284, May-June 2018, doi: 10.1109/TIA.2018.2807382.

[24] "Source forge: dolomites", https://sourceforge.net/projects/dolomites/

[25] J. R. Hendershot Jr, T. J. E. Miller, "Design of brushless permanent-magnet motors", Magna Physics Publications, Oxford Science Publications, 1994, pp. 3-23

[26] M. Barcaro, G. Meneghetti and N. Bianchi, "Structural Analysis of the Interior PM Rotor Considering Both Static and Fatigue Loading," in *IEEE Transactions on Industry Applications*, vol. 50, no. 1, pp. 253-260, Jan.-Feb. 2014, doi: 10.1109/TIA.2013.2268048.

[27] P. B. Reddy, A. M. El-Refaie, K. Huh, J. K. Tangudu and T. M. Jahns, "Comparison of Interior and Surface PM Machines Equipped With Fractional-Slot Concentrated Windings for Hybrid Traction Applications," in *IEEE Transactions on Energy Conversion*, vol. 27, no. 3, pp. 593-602, Sept. 2012, doi: 10.1109/TEC.2012.2195316.

[28] D. Sc. Pia Salminen, Prof Juha Pyrhönen, Lic. Sc. Florence Libert, D. Sc. Juliette Soulard, "Torque Ripple of Permanent Magnet Machines with Concentrated Windings", ISEF, 2005

Appendix

Electric steel datasheet

NO20-1350N Data sheet
thin non-oriented electrical steel

The Hi-Lite grade NO20-1350N fulfils all requirements in the standards EN 10303:2015 and IEC 60404-8-8:2017. In many cases the minimum / maximum properties are better than those of the grades with the same nominal thickness in these standards.

Magnetic properties

	Min / Max values	Typical values
Specific total loss at 1.0 T and 50 Hz	-	0.85 W/kg
Specific total loss at 1.5 T and 50 Hz	-	2.24 W/kg
Specific total loss at 1.0 T and 400 Hz	Max 13.5 W/kg	12.1 W/kg
Specific total loss at 1.5 T and 400 Hz	Max 32.5 W/kg	30.1 W/kg
Specific total loss at 1.0 T and 700 Hz	Max 29.1 W/kg	27.0 W/kg
Specific total loss at 1.0 T and 2500 Hz	-	188 W/kg
Peak magnetic polarisation at 2500 A/m and 50 Hz	Min 1.55 T	1.58 T
Peak magnetic polarisation at 5000 A/m and 50 Hz	Min 1.65 T	1.68 T
Peak magnetic polarisation at 10000 A/m and 50 Hz	Min 1.77 T	1.81 T
Relative peak permeability at 1.5 T and 50 Hz	-	900
Relative peak permeability at 1.0 T and 400 Hz	-	7500

Guaranteed values for losses are maximum total specific losses and guaranteed values for magnetic polarisations are minimum peak polarisations

Physical and mechanical properties

Nominal thickness 0.20 mm
Density (assumed) 7.65 kg/dm^3

	Min / Max values	Typical values
Electrical resistivity at 23 °C	-	51 μΩ·cm
Thermal conductivity at 23 °C	-	23 W/(m·K)
Thermal expansion 0-100 °C	-	$12 \cdot 10^{-6}$ /°C
Yield strength $R_{p0.2}$	Min 320 MPa	360 MPa
Tensile strength R_m	Min 410 MPa	450 MPa
Elongation at fracture A_{80}	Min 14 %	19 %
Young's modulus	-	190 GPa

Values for the yield strength, tensile strength and Young's modulus are given for the rolling direction. Corresponding values for the transverse direction are approximately 2 % higher.

For more information and contact:
www.hi-lite.se
www.tatasteeleurope.com
sales@sura.se

TATA STEEL

HI-LITE™
HIGH PERFORMANCE · ULTRA LIGHT

NO20-1350N Data sheet

thin non-oriented electrical steel

Typical specific total loss

J_{peak} (T)	Typical specific total loss (W/kg)								
	50 Hz	100 Hz	200 Hz	400 Hz	700 Hz	1000 Hz	2500 Hz	5000 Hz	10000 Hz
0.1	0.02	0.04	0.09	0.21	0.45	0.77	3.01	8.83	25.0
0.2	0.06	0.14	0.31	0.76	1.65	2.78	10.7	31.1	90.0
0.3	0.12	0.28	0.63	1.56	3.38	5.63	22.0	63.1	186
0.4	0.19	0.44	1.02	2.56	5.54	9.26	36.1	105	311
0.5	0.28	0.62	1.47	3.72	8.14	13.6	53.1	156	467
0.6	0.37	0.82	1.99	5.06	11.1	18.6	73.2	216	
0.7	0.47	1.06	2.56	6.56	14.4	24.2	96.2	288	
0.8	0.58	1.31	3.20	8.23	18.2	30.6	123	373	
0.9	0.71	1.60	3.90	10.1	22.3	37.7	153	473	
1.0	0.85	1.93	4.70	12.1	27.0	45.7	188		
1.1	1.02	2.31	5.61	14.4	32.2	54.7	228		
1.2	1.23	2.77	6.69	17.2	38.2	65.3	276		
1.3	1.49	3.35	8.07	20.5	45.5	77.3	332		
1.4	1.84	4.14	9.87	25.0	55.0	93.2			
1.5	2.24	4.98	11.9	30.1	66.0	112			
1.6	2.61	5.82	13.7	34.6	76.3	129			
1.7	2.99	6.54							
1.8	3.37	7.41							
1.9	3.86	8.53							

Typical peak magnetic polarisation (magnetisation curve)

H_{peak} (A/m)	Typical peak magnetic polarisation, J_{peak} (T)								
	50 Hz	100 Hz	200 Hz	400 Hz	700 Hz	1000 Hz	2500 Hz	5000 Hz	10000 Hz
20	0.041	0.040	0.038	0.036	0.034	0.032	0.031	0.024	0.024
30	0.12	0.12	0.11	0.10	0.09	0.08	0.07	0.04	0.03
50	0.56	0.53	0.47	0.36	0.26	0.21	0.14	0.09	0.06
70	0.86	0.82	0.78	0.65	0.50	0.42	0.22	0.14	0.10
100	1.06	1.04	1.00	0.96	0.88	0.77	0.40	0.24	0.16
150	1.21	1.20	1.18	1.17	1.13	1.11	0.75	0.46	0.27
200	1.28	1.28	1.27	1.25	1.24	1.24	1.02	0.67	0.40
400	1.38	1.38	1.38	1.37	1.37	1.37	1.33	1.10	0.92
800	1.45	1.45	1.45	1.45	1.45	1.45	1.42	1.32	
1500	1.52	1.52	1.52	1.52	1.52	1.52	1.50		
2500	1.58	1.58	1.58	1.58	1.58	1.58	1.57		
5000	1.68	1.68	1.68	1.68	1.68				
7500	1.75	1.75							
10000	1.81	1.81							
20000	1.92	1.92							

For more information and contact:
www.hi-lite.se
www.tatasteeleurope.com
sales@sura.se

TATA STEEL

The information and data in this data sheet is accurate to the best of Surahammars Bruk's knowledge but are intended for general information only. Surahammars Bruk and its businesses accept no liability for errors or information which is found to be misleading.

Mar 2019

2p=8 winding schemes

p=4 Q=18 q=0.75 t=2

Slot matrix:
ka=-[1 0 -1 0 0.5 0 0 -0.5 0 1 0 -1 0 0.5 0 0 -0.5 0]
kb=-[0 0.5 0 0 -0.5 0 1 0 -1 0 0.5 0 0 -0.5 0 1 0 -1]
kc=-[0 -0.5 0 1 0 -1 0 0.5 0 0 -0.5 0 1 0 -1 0 0.5 0]
The a-axis is on the slot 2.

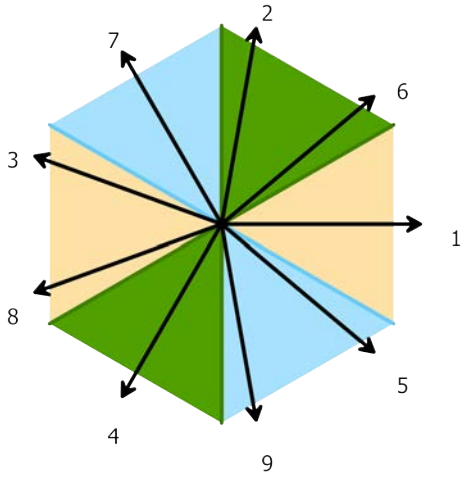

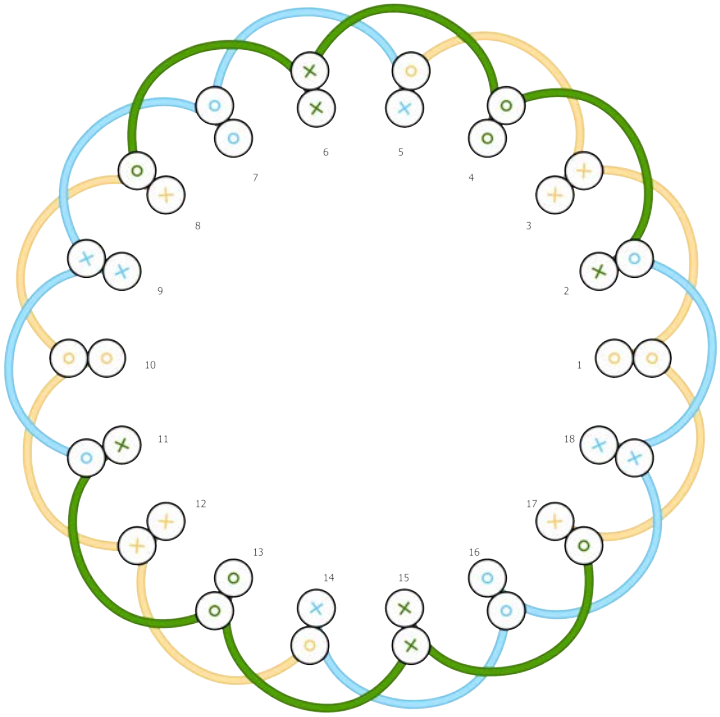

p=4 Q=30 q=1.25 t=2

Slot matrix:

ka=-[0.5 0 0 -0.5 -0.5 0 0 1 0.5 0 -0.5 -1 0 0 0.5 0.5 0 0 -0.5 -0.5 0 0 1 0.5 0 -0.5 -1 0 0 0.5]

kb=-[0 0 1 0.5 0 -0.5 -1 0 0 0.5 0.5 0 0 -0.5 -0.5 0 0 1 0.5 0 -0.5 -1 0 0 0.5 0.5 0 0 -0.5 -0.5]

kc=-[-0.5 -1 0 0 0.5 0.5 0 0 -0.5 -0.5 0 0 1 0.5 0 -0.5 -1 0 0 0.5 0.5 0 0 -0.5 -0.5 0 0 1 0.5 0]

The a-axis is between the slots 2 and 3.

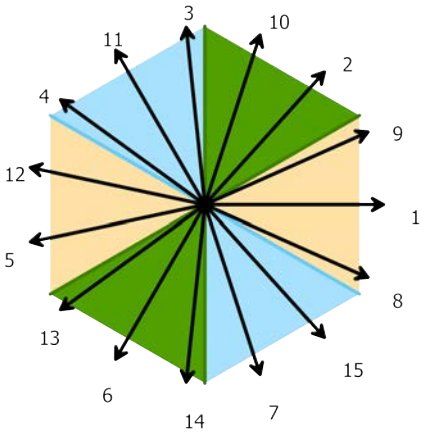

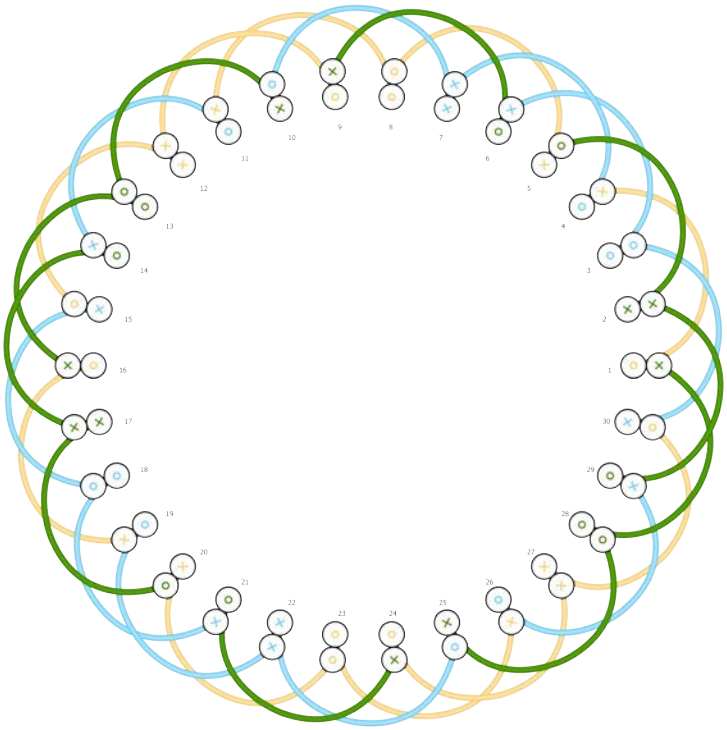

p=4 Q=36 q=1.5 t=4

Slot matrix:

ka=[1 0 0 0 -1 -0.5 0 0 0.5 1 0 0 0 -1 -0.5 0 0 0.5 1 0 0 0 -1 -0.5 0 0 0.5 1 0 0 0 -1 -0.5 0 0 0.5]

kb=[0 0 0.5 1 0 0 0 -1 -0.5 0 0 0.5 1 0 0 0 -1 -0.5 0 0 0.5 1 0 0 0 -1 -0.5 0 0 0.5 1 0 0 0 -1 -0.5]

kc=[0 -1 -0.5 0 0 0.5 1 0 0 0 -1 -0.5 0 0 0.5 1 0 0 0 -1 -0.5 0 0 0.5 1 0 0 0 -1 -0.5 0 0 0.5 1 0 0]

The a-axis is between the slots 7 and 8.

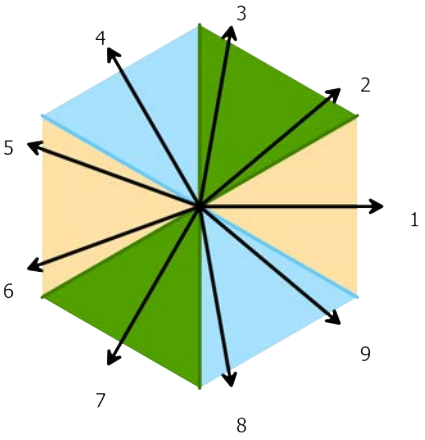

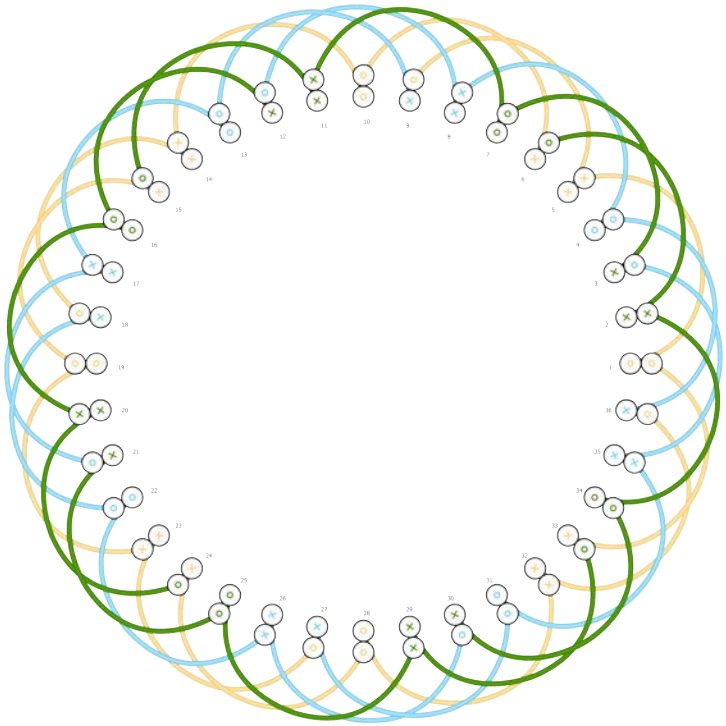

2p=10 winding schemes

p=5 Q=12 q=0.4 t=1

Slot matrix:
ka=-[1 -0.5 0 0 0 0.5 -1 0.5 0 0 0 -0.5]
kb=-[0 0.5 -1 0.5 0 0 0 -0.5 1 -0.5 0 0]
kc=-[0 0 0 -0.5 1 -0.5 0 0 0 0.5 -1 0.5]
The a-axis is on the slot 4.

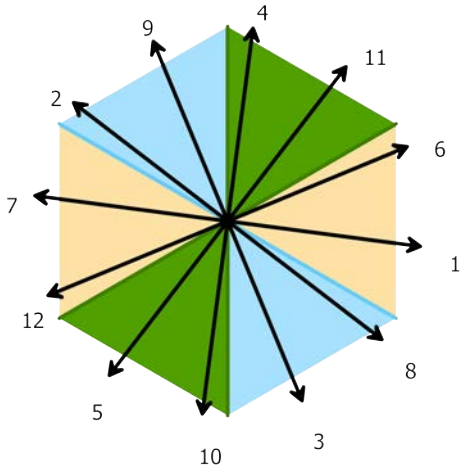

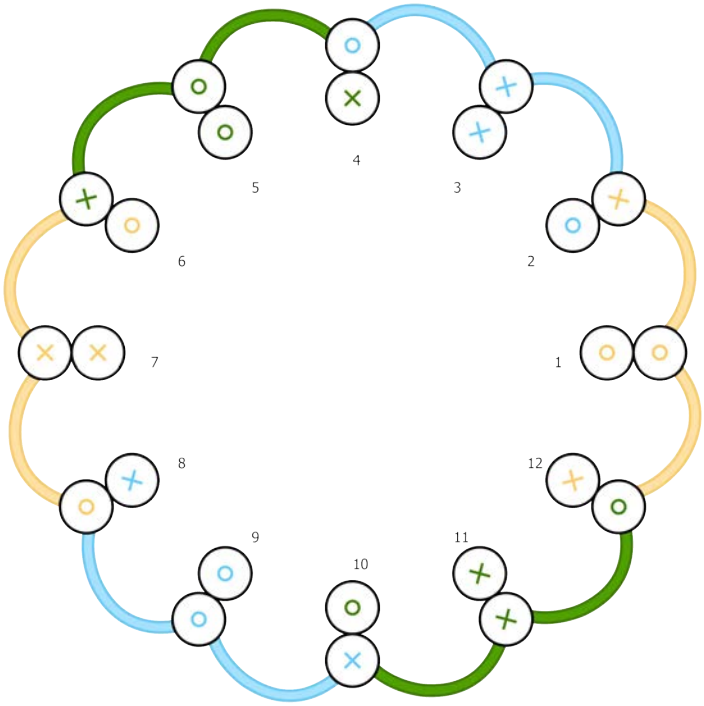

p=5 Q=24 q=0.8 t=2

Slot matrix:

ka=[1 0 -0.5 0 0 0.5 0 -1 0 0.5 0.5 0 -1 0 0.5 0 0 -0.5 0 1 0 -0.5 -0.5 0]

kb=[0 0.5 0.5 0 -1 0 0.5 0 0 -0.5 0 1 0 -0.5 -0.5 0 1 0 -0.5 0 0 0.5 0 -1]

kc=[0 -0.5 0 1 0 -0.5 -0.5 0 1 0 -0.5 0 0 0.5 0 -1 0 0.5 0.5 0 -1 0 0.5 0]

The a-axis is between the slots 4 and 5.

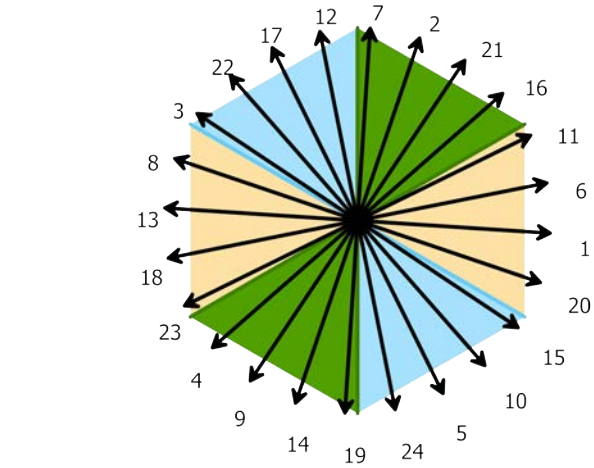

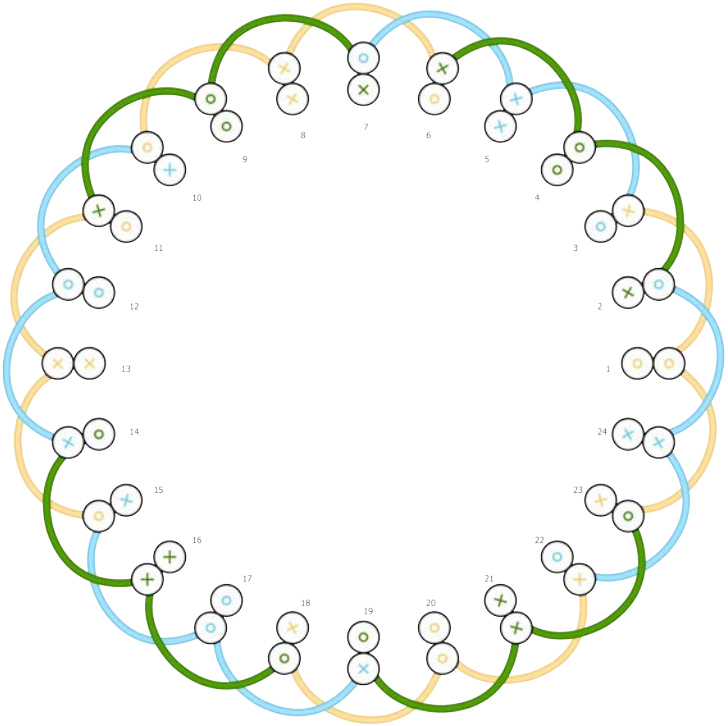

p=5 Q=36 q=1.2 t=1

Slot matrix:

ka=-[1 0 0 -0.5 -0.5 0 0 1 0 0 -0.5 -0.5 0 0 1 0.5 0 -0.5 -1 0 0 0.5 0.5 0 0 -1 0 0 0.5 0.5 0 0 -1 -0.5 0 0.5]

kb=-[0 0 1 0.5 0 -0.5 -1 0 0 0.5 0.5 0 0 -1 0 0 0.5 0.5 0 0 -1 -0.5 0 0.5 1 0 0 -0.5 -0.5 0 0 1 0 0 -0.5 -0.5]

kc=-[0 -1 0 0 0.5 0.5 0 0 -1 -0.5 0 0.5 1 0 0 -0.5 -0.5 0 0 1 0 0 -0.5 -0.5 0 0 1 0.5 0 -0.5 -1 0 0 0.5 0.5 0]

The a-axis is on the slot 17.